288 882

ELECTROFLUIDMECHANICS:
INVESTIGATION OF THE EFFECTS OF ELECTROSTATIC
FIELDS ON HEAT TRANSFER AND BOUNDARY LAYERS

Henry René Vellkoff
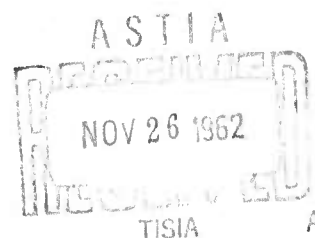
TECHNICAL DOCUMENTARY REPORT NO. ASD-TDR-62-650

September 1962

Propulsion Laboratory
Aeronautical Systems Division
Air Force Systems Command
Wright-Patterson Air Force Base, Ohio

Aeronautical Systems Division, Dir/Aeromechanics,
Propulsion Laboratory, Wright-Patterson AFB, Ohio
Rpt Nr ASD-TDR-62-650. ELECTROFLUIDMECHANICS:
INVESTIGATION OF THE EFFECTS OF ELECTROSTATIC
FIELDS ON HEAT TRANSFER AND BOUNDARY LAYERS.
Final report, Sep 62, 128p. incl illus., tables, 31 refs.

Unclassified Report

A series of experiments were conducted on the influence
of an electric field on free convection heat transfer. A
heated plate was mounted in a Mach-Zehnder interfero-
meter, and the effects of applied electrical fields were
studied. Large changes in effective heat transfer were
found. Analytical studies were made of this phenomenon.
A suitable mathematical model was formulated on the
basis of the Von Karman integral equations and the

(over)

electrostatic field equations. Correlation between the
interferometer test data and the mathematical model
was achieved.

Exploratory tests of fluid orientation and motion under
the influence of dielectric forces were also conducted,
and the potential usefulness of the phenomenon is
graphically portrayed in pictures showing the motion
of water droplets in a "Zero-G" model when a field is
applied.

1. Electrostatic fields
2. Fluid mechanics
3. Heat transfer
4. Hydrodynamics
5. Boundary layer

I. AFSC Project 3141
II. H. R. Velkoff
III. Aval fr OTS
IV. In ASTIA collection

Aeronautical Systems Division, Dir/Aeromechanics,
Propulsion Laboratory, Wright-Patterson AFB, Ohio
Rpt Nr ASD-TDR-62-650. ELECTROFLUIDMECHANICS:
INVESTIGATION OF THE EFFECTS OF ELECTROSTATIC
FIELDS ON HEAT TRANSFER AND BOUNDARY LAYERS.
Final report, Sep 62, 128p. incl illus., tables, 31 refs.

Unclassified Report

A series of experiments were conducted on the influence
of an electric field on free convection heat transfer. A
heated plate was mounted in a Mach-Zehnder interfero-
meter, and the effects of applied electrical fields were
studied. Large changes in effective heat transfer were
found. Analytical studies were made of this phenomenon.
A suitable mathematical model was formulated on the
basis of the Von Karman integral equations and the

(over)

1. Electrostatic fields
2. Fluid mechanics
3. Heat transfer
4. Hydrodynamics
5. Boundary layer

I. AFSC Project 3141
II. H. R. Velkoff
III. Aval fr OTS
IV. In ASTIA collection

electrostatic field equations. Correlation between the
interferometer test data and the mathematical model
was achieved.

Exploratory tests of fluid orientation and motion under
the influence of dielectric forces were also conducted,
and the potential usefulness of the phenomenon is
graphically portrayed in pictures showing the motion
of water droplets in a "Zero-G" model when a field is
applied.

Aeronautical Systems Division, Dir/Aeromechanics,
Propulsion Laboratory, Wright-Patterson AFB, Ohio
Rpt Nr ASD-TDR-62-650. ELECTROFLUIDMECHANICS:
INVESTIGATION OF THE EFFECTS OF ELECTROSTATIC
FIELDS ON HEAT TRANSFER AND BOUNDARY LAYERS.
Final report, Sep 62, 128p. incl illus., tables, 31 refs.

Unclassified Report

A series of experiments were conducted on the influence
of an electric field on free convection heat transfer. A
heated plate was mounted in a Mach-Zehnder interfero-
meter, and the effects of applied electrical fields were
studied. Large changes in effective heat transfer were
found. Analytical studies were made of this phenomenon.
A suitable mathematical model was formulated on the
basis of the Von Karman integral equations and the

(over)

electrostatic field equations. Correlation between the
interferometer test data and the mathematical model
was achieved.

Exploratory tests of fluid orientation and motion under
the influence of dielectric forces were also conducted,
and the potential usefulness of the phenomenon is
graphically portrayed in pictures showing the motion
of water droplets in a "Zero-G" model when a field is
applied.

1. Electrostatic fields
2. Fluid mechanics
3. Heat transfer
4. Hydrodynamics
5. Boundary layer

I. AFSC Project 3141
II. H. R. Velkoff
III. Aval fr OTS
IV. In ASTIA collection

FOREWORD

This report was originally prepared as a dissertation in partial fulfillment of the requirements for the Degree of Doctor of Philosophy in the Graduate School of The Ohio State University. This report differs somewhat from the original dissertation since it was edited for compliance with requirements for an ASD Technical Documentary Report.

The research work was accomplished under Project 3141, "Electric Propulsion Technology," in the Propulsion Laboratory, Directorate of Aeromechanics, Deputy for Technology, Aeronautical Systems Division, with Henry R. Velkoff serving as project scientist. This covers the second phase of a phased study on electrokinetics in fluid motion. The first phase is covered in ASD Technical Report 61-642.

This research represents the efforts of many many persons. The author wishes to express his gratitude and appreciation to the following:

The Aeronautical Systems Division for making it possible for him to attend The Ohio State University and complete the research presented in this paper.

Professor S. M. Marco, of The Ohio State University, for the advice and encouragement given in the initial concept and in the conduct of this research.

Mr. E. C. Phillips, of the Directorate of Aeromechanics, for his understanding, support, and patience, which contributed greatly to the successful completion of the work.

Professor A. J. Shine and his staff, of the Mechanical Engineering Laboratory, Air Force Institute of Technology, whose offer of the interferometer, associated equipment, and assistance, permitted the verification tests to be completed effectively in minimum time.

2nd Lt W. Guyton and Mr. J. Yatteau, of the Propulsion Laboratory, for their effective work in conducting the tests on dielectrophoresis and to Mr. R. Loase for his assistance in conducting the tests and preparing the data.

The many people who provided excellent support in obtaining the manometer equipment, electrical supplies, photographic equipment, and all the other vital equipment necessary to complete the job.

The Ohio State University for permission to publish this dissertation as an ASD Technical Documentary Report.

ABSTRACT

A series of experiments were conducted on the influence of an electric field on free convection heat transfer. A heated plate was mounted in a Mach-Zehnder interferometer, and the effects of applied electrical fields were studied. Large changes in effective heat transfer were found. Analytical studies were made of this phenomenon. A suitable mathematical model was formulated on the basis of the Von Karman integral equations and the electrostatic field equations. Correlation between the interferometer test data and the mathematical model was achieved.

Exploratory tests of fluid orientation and motion under the influence of dielectric forces were also conducted, and the potential usefulness of the phenomenon is graphically portrayed in pictures showing the motion of water droplets in a "Zero-G" model when a field is applied.

TABLE OF CONTENTS

TABLE OF CONTENTS (Continued)

LIST OF ILLUSTRATIONS

LIST OF ILLUSTRATIONS (Cont'd)

LIST OF ILLUSTRATIONS (Cont'd)

LIST OF ILLUSTRATIONS (Cont'd)

LIST OF ILLUSTRATIONS (Cont'd)

LIST OF SYMBOLS

SYMBOL	DEFINITION	UNITS
A	area	sq. ft.
a	distance-corona wire to plate	cm
b	impinging jet half-width	cm
C_p	specific heat at constant pressure	BTU/lb-°F
c_i	empirical corona pressure constant	lb/sq. ft.-micro amps
E	electrical field strength	volts/meter
F	body force	lb/cu. ft.
$F(\eta)$	heat transform	dimensionless
$F(z)$	boundary layer parameters	dimensionless
$f(\eta)$	heat transfer transform	dimensionless
G	geometric shape factor	dimensionless
g	acceleration of gravity	32.2 ft./sec.²
h_x	convective heat transfer coefficient	BTU/hr-sq. ft.-°F
h	average value of heat transfer coefficient with current	BTU/hr-sq. ft.-°F
h_o	average value of heat transfer coefficient without field	BTU/hr-sq. ft.-°F
i	current	microamperes
J	current density	amps/sq. meter
J_m	mechanical equivalent of heat	778 ft lb/BTU
K	ion mobility	sq. meter/volt-sec
k	thermal conductivity	BTU/hr-ft.-°F
m	length	meters
N_{Ek}	Eckert number	dimensionless
N_{Pr}	Prandtl number $C_p\mu/k$	dimensionless
p	pressure	lb/sq. ft.
p_o	ambient pressure	lb/sq. ft.
p_c	centerline stagnation pressure	lb/sq. ft.
q_g	internal heat generated	BTU/hr-cu. ft.
q_r	energy radiated	BTU/hr-cu. ft.
R	radius of electrode	feet
R_1	distance	meters

LIST OF SYMBOLS (Cont'd)

SYMBOL	DEFINITION	UNITS
R_2	distance	meters
r	radial distance	meters
r_a	radius at edge of intense corona	meters
T	temperature	°F
T_o	ambient temperature	°F
T_w	wall temperature	°F
t	transformation plane	dimensionless
U	impinging velocity	ft./sec
u	velocity	ft./sec
u_x	velocity in boundary layer	ft./sec
u_∞	velocity outside of boundary layer	ft./sec
V	applied potential	volts
V_c	voltage at start of corona current	volts
v	velocity	ft./sec
v_t	total ion velocity	ft./sec
w	complex number	
X	body force	lbs/cu. ft.
x	coordinate distance-distance along plate	inches
y	coordinate distance-distance perpendicular to plate	inches
z	$z = x/a$ dimensionless distance along plate	dimensionless
z_c	complex number $z_c = x + iy$	
α	thermal diffusivity $k/\rho C_p$	ft.^{2}/hr
β_1	stagnation pressure constant	1/sec
γ	pressure ratio parameter	dimensionless
Δ	$\dfrac{\partial u}{\partial x} + \dfrac{\partial v}{\partial y} + \dfrac{\partial w}{\partial z}$	
δ	velocity boundary layer thickness	feet
δ_0	boundary layer thickness at origin	feet
δ_T	thermal boundary layer thickness	feet
$\delta*$	ratio of thermal to velocity boundary layer thickness	dimensionless
ϵ	permittivity	farads/meter

LIST OF SYMBOLS (Cont'd)

SYMBOL	DEFINITION	UNITS
ζ	transformation plane	
η	heat transfer variable, defined in text	
θ	temperature difference, $T - T_o$	°F
θ_o	temperature difference, $T_w - T_o$	°F
θ_c	angle subtended by electrode	radians
λ	charge per unit length	coulombs/meter
μ	dynamic viscosity	lb/ft.-hr
μa	current	microamperes
ν	kinematic viscosity	ft.^{2}/hr
ρ	density	lb_m/cu. ft.
ρ_c	charge density	coulombs/cu. meter
σ_c	electrical conductivity	1/ohms
τ	time	seconds
Φ	dissipation function, defined in text	
ψ	stream function, defined in text	

INTRODUCTION

The influence exerted by an electric field on gases and liquids has been known for many years. Primary attention has been given to studying electrolytic phenomena and gas discharges, however, and relatively little work has been done on the effects of electric fields acting alone on the flow of fluids. Such field effects tend to be rather subtle in contrast to the relatively large fluid body force generated by the interaction of an electric field and a transverse magnetic field. This latter fluid-electromagnetic interaction gives rise to the whole field of magnetohydrodynamics (MHD). The interest in MHD has received wide attention in recent years because of potential applications in power generation, controlled fusion, and space propulsion. The subtle electric field effects, however, merit consideration apart from the mass of the work done on magnetohydrodynamics. The fluid-electric interactions are generally distinct from those in the MHD field.

An electric field can influence not only fluids containing charged particles and conducting fluids, but neutral nonconducting fluids as well. This wide range of action may provide controllable body forces within the fluid without the high degree of ionization customarily used in magnetohydrodynamics. Changes in fluid properties, such as viscosity or conductivity, can also occur in the presence of a field, and thus the entire behavior of fluid flow and heat transfer may be affected.

It is the purpose of this research to explore the possible interactions between electric fields and fluids. Because of the wide range of possible influences, an extensive survey of possible electric field-fluid interactions was conducted to provide a sound basis for the specific areas of research chosen. A summary of the interactions presented in Reference 1, includes the basic electrical phenomena involved, descriptions of the various interactions observed in experiments, and a discussion of the potential application of the phenomena.

Two specific electric-fluid interactions were selected for these more detailed investigations: the effects of ion motion in gases, and the motion of neutral particles. In the study of the ion motions, a combined experimental and analytical program of the effects of a corona discharge on the free convection from a heated plate was undertaken. A Mach-Zehnder interferometer was used to record results of experiments, and the analytical approach was based upon the Navier Stokes, energy, Von Karman, and electric field equations. Correlations between the theoretical solutions and the test data were accomplished. The motion of neutral particles as represented by dielectrophoresis was studied only in an exploratory fashion to verify the possible actions which could be obtained through the application of an electric field. An explanation of the corona wind and dielectrophoresis is included in Reference 1.

EXPERIMENTAL INVESTIGATION OF THE EFFECT
OF CORONA WIND ON FREE CONVECTION

This section covers the experimental work done in studying one possible interaction between an electrical field and a fluid. The experiment chosen is that of a corona discharge impinging on a heated flat plate. The section will describe the experimental phases of the work and a description of the phenomena observed.

AIMS OF THE CORONA WIND-HEAT TRANSFER TESTS

In order to study the possible effects which could be achieved by electric fields acting on ions in gases, it was necessary to chose a phenomenon which could provide a suitable source of ions. Many possible sources exist including combustion flames, ultra-violet radiation of the gas, and others. A controllable source, and one which is simple to obtain, is that of the ions in a corona discharge (Ref. 2).

The phenomenon of corona wind is discussed in detail in Reference 1, but the basic action will be reviewed briefly here. If a fine needle-point electrode is located a short distance away from another blunt electrode, a stream of air moves away from the point when high voltages are applied between the point and the other electrode. This is illustrated in Figure 1.
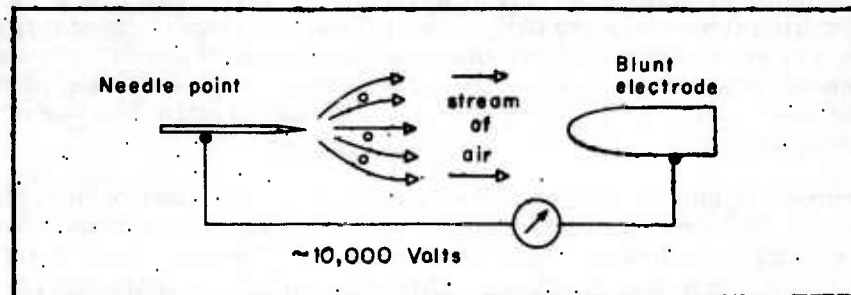
Figure 1. Corona wind from a charged point

Around the fine corona point an intense electrical field exists. Ions, existing in air naturally or created by this intense field, are accelerated by the field. These ions collide with neutral molecules of air and, near the point, further ionization takes place. Away from the region of the point, the collisions are elastic and a streaming of the air results. The net effect is the corona wind moving away from the charged point. The velocities obtainable from the corona wind in air are very small, of the order of a few feet per second. If this slight streaming were made to impinge upon a heated plate, however, a change in the flow field and temperature distribution should result. The free convection from the heated plate in still air would also provide a very sensitive phenomenon to explore with the corona wind or with any other electrostatic influence which might exist. Consequently, a combined free convection-electrostatic test was planned.

To actually conduct such a test, a Mach Zehnder interferometer was utilized (Ref. 3). Using the interference patterns of light, the interferometer can record very small changes in the temperature field around the test specimen. Any changes induced by the corona wind or electrostatic field should thus be recorded by the interferometer as changes in the interference pattern. Thus the experiment actually conducted is based upon studying a very sensitive phenomenon (free-convection) with an extremely sensitive instrument (the interferometer) to detect any potentially small influences of the applied electrostatic field. The data

2

obtained from the interferometer, although of considerable value, pertain only to temperature distributions. Since no information could be obtained with this instrument about the velocity distribution in the vicinity of the plate, pressure effects were studied separately and the velocities were then deduced.

Many electrode configurations were conceived to provide a suitable corona discharge and the field shaping necessary to control the phenomena. Electrodes that would provide a field without a corona discharge were constructed and used to provide base line data with no ions and to explore any possible effects not directly associated with ion motion. Because the corona wind tests indicated some very interesting results, most of the work was concentrated upon the corona discharge. The work with the other electrode configurations were exploratory only.

DESCRIPTION OF EXPERIMENTAL APPARATUS

Heat Transfer Equipment

A Mach-Zehnder interferometer was used to study the effects on heat transfer. The theory of operation of an interferometer is covered in numerous publications and will not be discussed in detail (Refs. 3, 4). Both infinite fringe and finite fringe patterns were used in the study. Because the infinite fringe patterns gave graphic and readily usable results, most of the runs were made with this setting. The phenomena were observed both with monochromatic light of 5641 Å and with white light. All data were taken with the monochromatic light source, although the white light was effective in visually studying the phenomena.

Figure 2 shows the over-all test apparatus with the interferometer located in the background. Depicted are the high voltage supply at the left, the working section of the interferometer in the center, and the free-convection heater power supply on the table. Figure 3 indicates the Polaroid Camera located at the rear of the interferometer, which was used to record the fringe patterns obtained. The controls at the right are used to adjust the interferometer to the fringe pattern desired.

The interferometer was located in a small building isolated from outside traffic and disturbances. All windows were covered over and taped to keep out extraneous light. Since random convective currents in the room caused occasional trouble in using the interferometer, all heat was turned off in the room for several hours prior to testing and throughout the tests. Likewise, even though the room had been apparently sealed, changes in atmospheric conditions, such as strong wind, bright sunlight, or rapidly changing temperature, caused fluctuations in the action of the interferometer. Consequently testing was accomplised only on relatively calm days with all heat turned off.

The specimen used to study free convection was an electrically heated flat aluminum plate 6 inches by 10 inches in size. In heat transfer tests conducted previously by personnel of the Air Force Institute of Technology, the temperature distribution of the plate had been found to be very uniform over a range of temperatures. The plate was heated by electrical resistance heaters inbedded in the rear of the plate and well insulated electrically from the metal plate itself. Iron-constantan thermocouples were located in the plate in the positions shown on Figure 4. The thermocouple junctions were located in holes drilled in the plate and later filled in, so that the front of the plate was smooth. During the course of the tests, four reference temperatures on the plate were read whenever data were taken with the interferometer. These temperatures remained within $1°F$ of each other except in a few cases in which the difference was slightly over $1°F$.

The plate is shown mounted vertically in the interferometer in Figure 5. Shown also in the figure are a typical electrode and the traversing mechanisms used.

Temperatures were read by means of a Rubicon Instruments potentiometer using an ice-water bath reference temperature for the thermocouples.

A.C. current was used to power the heaters in the plate in the early phases of the test. The power dissipated in the heaters was controlled by means of voltage regulators. The variation of temperature over the plate could be controlled by adjusting the applied voltage to specific heaters, and the mean plate temperature could be varied by a master voltage control. Although this power supply provided very good temperature regulation for the free convection tests without applied fields, it was found to cause difficulty with the microammeter used to measure corona currents. During initial studies of the combined corona-heat transfer tests, the microammeter gave very erratic readings whenever the A.C. heater supply was turned on. Because of this, the A.C. power supply was replaced by automotive storage batteries to provide a ripple-free D.C. power source. Variations in voltages required for temperature control were secured by a suitable rheostat. This arrangement eliminated the difficulty and the microammeter was steady through all its ranges. Plate temperatures were adjusted to uniform values and remained within the 1°F. tolerance. Figure 6 shows the heater power supply. The D.C. supply controls are at the front of the table and the A.C. Variacs are at the rear of the table. The batteries are below the table, and the voltmeters and ammeters to monitor heater input power are in the center of the table. The thermocouple potentiometer is in the rear of the table and a microammeter used to measure corona current is at the right.

Electrical Apparatus

A 0-50,000 volt power supply was used to provide the electrical field for the corona discharge. It had a current capacity of up to 2 milliamperes, which was more than adequate for the tests accomplished. The design of the power supply allowed only a negative ground; because of the arrangement of the test equipment only a positive point corona could be studied. A Greibach microammeter used to measure current, had ranges from 0-1 microamperes up to 0-1000 microamperes.

Three instruments were used to measure voltage. One voltmeter with a range of 0 to 50,000 volts, was incorporated as part of the power supply and was read during all heat transfer runs. The second voltmeter an RCA Voltohmyst, utilized a high-voltage probe, and drew undesirably high currents during operation; these currents could be accounted for, however, and calibrations were set up to correct for them. The third voltmeter, a Sensitive Research Instrument Corporation electrostatic voltmeter with a range of 0-40,000 volts, was used during precise voltage, current, and pressure measurements of various corona discharges. Independent of which voltmeter was used in the tests, it was found that the current was the most sensitive parameter to control and, as a consequence, all settings were based upon current. It was often noted that large variations in current occurred even though the changes in voltage were barely discernable.

For the tests with dielectrophoresis, an A.C. power supply was used. The supply consisted of a neon transformer connected to a Variac to provide a voltage range of zero to 20,000 volts. Several milliamperes of current could be drawn from this source.

Electrodes

Several types of electrodes that were fabricated and tested are shown in Figure 7. The electrode at the left consists of a series of No. 7 needles soldered precisely at 1/2-inch intervals along a 1/8-inch brass rod 11 inches long. The tips of the needles were aligned carefully in a jig so that distortion in the interferometer due to inaccuracies of needle arrangement would be at a minimum. The needles in this case served as the corona discharge points. The nondischarging electrode at the front is made of 1/8-inch brass rod shaped into a 12-inch oval. The electrode in the rear of the picture is a grid of fine wires 0.010 inch in diameter, 12-inches long, and spaced at one-inch intervals. The wires act as the corona discharge source. The electrode at the right is an unheated, flat, 6 by 10-inch aluminum plate that was used as a nondischarging electrode to provide an approximately parallel field.

The installation of an electrode typical of those used in these tests is shown in Figure 5, where the heated 6-by-10-inch aluminum plate is mounted in the interferometer. A single-wire electrode can be seen mounted at a distance of 2 centimeters in front of the plate. This single-wire electrode is typical of the type used primarily in these tests. It is a single stainless-steel wire kept under tension to keep it straight and electrically insulated from the mounting attachments. A small stranded-wire lead extends from the corona wire out to the point of attachment of the high-voltage lead. The electrode is mounted in a traversing mechanism that allows movement in three perpendicular coordinate directions. Thus the corona wire may be moved up and down or its distance from the plate varied as required. The wire shown in the figure is 12 inches long and 0.004 inch in diameter.

Both the plate and the electrode were electrically insulated from the remainder of the equipment. The plate was maintained at ground potential by the ground return lead to the power supply. All the sharp edges of the plate and the electrodes were rounded or covered with cement or corona dope to minimize undesirable localized corona discharge, and the surface of the plate was burnished and polished, clean and free of sharp scratches. In spite of the precautions, however, some localized discharge occurred both from spots on the plate and from distinct points on the various electrodes at very high values of applied voltage. Fortunately, these localized discharges appeared to occur only at voltages and currents beyond the range of interest in the study.

Pressure Survey Equipment

To interpret the phenomena observed with the interferometer, it became necessary to study the pressure distribution between various electrodes and the flat plate. Review of data obtained by Chattock, Harney, Stuetzer, and Robinson (Refs. 5, 6, 7, and 8, respectively) revealed that a sharp pressure peak could be expected directly beneath the fine wire during a corona discharge. None of these investigators, however, had published any data for the case of fine wires placed parallel to a flat plate.

To determine the pressure distribution, tests were run using an arrangement similar to that shown in Figure 5, but the heated plate was replaced by a pressure plate equipped with a series of pressure taps. Pressures were recorded during the corona discharge, but no interferometer or heat transfer data were taken during the pressure surveys.

Two different test configurations to measure pressure variation were set up. In the first configuration, a manometer board was tilted to a 10° angle. Flood lights were used for sharp definition of the meniscus for all the tubes, as shown in Figure 8. To measure

the pressures, a series of holes were drilled in a 7 by 12 inch aluminum plate at 0.2-inch intervals with a No. 54 drill along the horizontal and vertical centerlines of the plate. One hole was drilled at the center of the plate and the remainder were spaced outwardly to a distance of two inches from the center. The back of the plate was counterdrilled so that 1/16 inch metal tubing could be inserted. All tubes were sealed into the plate with a Glyptol varnish. The pressure measuring plate is shown at the top of the manometer board in Figure 8.

Plastic tubing was used to connect the pressure taps to the manometer board. All leads were made as short as possible, and all connections were made as tight as possible to minimize the possibility of leakage. The entire surface of the plate was polished. All nicks, scratches, and rough edges were smoothed out, and corona dope was applied at all positions of potential local discharge away from the center of the plate.

To obtain useful data on the very small pressure differences, special procedures had to be employed in using the manometer board. Room temperature changes had to be watched carefully to minimize drift effects. A Polaroid camera was mounted above and perpendicular to the manometer board to minimize distortion. Polaroid pictures were taken of each test sequence and read by means of a Gaertner Comparator. Reference pictures were taken before and after each test sequence. By comparing the position of the meniscus on each data run with the corresponding reference values, it was possible to read values of pressure to less than 0.001 inches of water. Repeatability was good. The simultaneous readings of pressure across the face of the plate gave a good indication of the form of the pressure distribution.

The second technique of measuring pressure utilized the same electrodes and pressure plate, but the pressures were read by means of a Chattock micromanometer. The photograph of this pressure test set-up, Figure 9, shows the high-voltage power supply, electrostatic voltmeter, and ammeter, as well as the pressure plate and manometer. Since the Chattock micromanometer, shown in Figure 10, provides only one pressure reading at a time, it was necessary to change the connection between the pressure taps and the manometer in sequence. The plastic tubing lead was shortened as much as possible to minimize the lag in the system and the lines made as clear as possible. Readings to determine the lag time indicated that a stable value was achieved well within one minute.

The Chattock manometer uses a two-fluid "U" tube. The fluids used in this case were kerosene and distilled water. A Gaertner Comparator, which was used to read the level of the meniscus, increased the sensitivity of the instrument and facilitated reading. The Chattock manometer, however, requires considerable adjustment and care in operation if consistent data are to be obtained. Room temperature variations, outside winds, and gusts readily affected not only the individual readings but the zero shifts, and variations in humidity affected the corona discharge. Consequently pressure tests were run only on quiet days with the room heat turned off, and on days when the relative humidity was not high. Figure 11 illustrates a typical set-up with the single wire in place a short distance in front of the pressure plate.

Experimental Procedures

Because electrostatic phenomena produce forces that are small in magnitude, it was necessary to watch for all extraneous disturbances that could occur in the test environment as well as the accuracy of the instrumentation. The difficulties with the temperature variations, gusty weather, and humidity have been indicated previously. To alleviate the presence of small random air motions in the vicinity of the test section of the interferometer, an enclosure was placed about this area. This enclosure was located so as to not

materially affect the free-convection flow of air near the plate, the flow of air from the plate, and the flow of air from the corona discharge. Use of the enclosure resulted in more stable test patterns.

An interferometer provides data on the isothermal lines in the fluid around a heated body by sensing the average density changes in the working section. A free-convection test of a flat plate in still air will reveal a series of fringes in front of the plate. By measuring the spacing of the fringes and calculating the temperatures existing in each fringe, it is possible to determine the temperature profile through the thermal boundary layer as well as the local heat transfer coefficients. A typical interferometer picture, Figure 12, shows an end view of the test specimen with the flat heated surface at the right. The fringes are evident in front of the plate. In this case, the plate temperature was 92°F and the room temperature was 64.1°F. The "T"-shaped rod at the bottom provides a reference length for data reduction. The end view of the electrode support rod can be seen at the left side. The fine corona wire at the end of the rod cannot be discerned in the picture. No voltage was applied at the time this interferogram was taken. When a voltage is applied between the fine wire and the plate and changes to the thermal boundary layer occur, the fringe patterns are distorted. In general, if the fringes are brought closer together so that the thermal boundary layer is thinner, heat transfer increases. If the boundary layer is pulled outwardly, the heat transfer rate decreases. Thus, when viewing the data presented in subsequent photographs, these basic points should be borne in mind as an aid in interpreting the phenomena.

The accuracy of the data depends on both the environmental conditions and the instrumentation used. Temperatures measured with the thermocouples and the thermometers could be read to within 0.1°F. The interferometer fringe patterns contain errors due to the variation in density in the horizontal direction along the plate. This error can be compensated for and a compensation is included in the data reduction method. A second error is introduced by the end effects of the finite plate width. The largest inaccuracy comes in the actual measurements of the spacings of the fringes. Although the Gaertner Comparator can measure the spacing to 0.0001 inch, determining the centerline of the fringes introduces far greater uncertainties. When the fringes are diffused and spread far apart, a sizeable uncertainty can result. Conversely, an uncertainty is also introduced when the fringes are compacted, one upon the other, because the individual lines are difficult to locate.

The voltage and current data are also subject to inaccuracies. As mentioned previously, the voltage used in corona discharge phenomena is a relatively insensitive parameter in the region of the initial flow of corona current. In order to initiate the corona discharge, the voltage control knob of the power supply was turned slowly until a change in current could be observed, but the voltage reading was of little assistance in determining the starting point. Many calibrations were made with the three voltmeters described previously. The precision electrostatic voltmeter, which was used as a standard to calibrate the others, was available for use during only a portion of the work; as a consequence, recourse was made to the less accurate instruments.

Current measurements made with the Greibach Microammeter are considered to be accurate. Unfortunately, corona discharge currents are very erratic. The fundamental nature of the discharge currents with a positive point consists of a series of random current pulses accompanying electron avalanches toward the positive point. Slight variations in atmospheric conditions in the vicinity of the wire could also cause variations in the corona current. Consequently, the pointer of the microammeter moved continually and erratically during all readings. These same variations have been noted by other

7

investigators (Refs. 6, 8). Several readings were usually taken, but drifting would occur to either the high or low side, and the averages were not truly representative. Efforts were made in all tests to take readings at the most stable current value in the range under consideration. Because of this erratic behavior, it was difficult to assign a value to the accuracy of the current data even though it is a most sensitive parameter in this investigation. From study of many data points, it is believed that the current values are within 5 per cent in the small current ranges (less than 10 μa) and considerably better than that in the higher ranges.

The pressure data contain several possible sources of inaccuracies. With both manometers, the possibility existed of the meniscus sticking to the wall of the tubes and thus introducing errors. If light were directed continuously on either manometer, all readings became meaningless; volumetric changes and distortions of the apparatus occurred from exposure to direct light for more than an instant. Consequently, when working with the inclined manometer, the lights were flashed on momentarily while taking a picture of the tubes.

The Chattock manometer was particularly sensitive to random external disturbances. As indicated before, changes in temperature, drafts, outside winds, and aircraft in flight all could cause erratic readings. In addition to these, even such disturbances as doors being closed, cabinets opened, and other tests being conducted in remote areas could cause severe transients in the pressure readings. An ideal location in which to perform these tests would have been a room with air conditioning, controlled humidity, extremely rugged walls, and heavy thermal insulation.

By setting the pressure equipment up in the same room with the interferometer, disturbances due to the movement of people was substantially eliminated. Testing was accomplished on what appeared to be very quiet and calm days. Even under the best conditions, a troublesome drift of the reference zero occurred. Many runs were obtained under good test conditions in which the zero shift was within 0.0001 inch of water, and these data show a consistent pattern with little shifting and distortion. Unfortunately, zero shifts occurred during some of the runs that consumed several hours, during which time small atmospheric changes may have occurred which were not readily detectable. Data obtained under these conditions were erratic and did not correlate well. In spite of the difficulties, we believe that the data as presented in the next section are reliable.

By far the most troublesome problem in the whole experiment was the difficulty in repeating tests and obtaining data with a high degree of precision (within one percent). Some of the factors causing this have been mentioned before, and these are of considerable importance. Fundamental to this problem, however, is the erratic character of the corona discharge itself. Variations of the corona due to small changes in humidity, local ionization, and random convective currents are very difficult to control. The average mobility of the ions is affected considerably by the amount of moisture in the air. Since pressure rise generally varies inversely with ion mobility, pressure rise due to corona discharge can be expected to vary with humidity. Since clear-cut corrections for the influence of humidity on pressure rise were not available, the pressure rise data were not corrected for humidity effects. The basic interactions between corona discharge and free-convection heat transfer, however, occurred at all ranges of humidity, from very dry cold days to foggy days with the humidity close to 100 percent.

RESULTS OF THE EXPERIMENTAL INVESTIGATION

Method of Data Interpretation

The heat transfer coefficients were obtained from the interferograms by measuring the spacing of the fringes and using the calculation procedures presented in Appendix 1. Readings were taken from at least ten separate locations along each plate. The data are presented in plots to show heat transfer coefficients along the surface of the plate, and the effects of varying current and wire spacing. Voltage-current graphs are presented to illustrate the usual characteristics of corona discharge.

Interferometer Data

The results of the combined electric field-convection tests are shown in the accompanying photographs and corresponding graphs. Only the most significant results are presented and interpreted. The first sequence of tests incorporates the heated plate in a vertical position, with a single stainless-steel electrode 0.004 inch in diameter located 2 cm away from the plate. This configuration provides an intense electrical field near the wire, and a highly nonuniform electrical field in the region in front of the plate. The wire is horizontal and at the centerline of the plate. The potential applied between the wire and the plate is slowly raised from zero up to values sufficient to give currents of approximately $150\mu a$.

Figure 13 presents a sequence of pictures as seen with the interferometer as the voltage is increased. View A is the reference photograph with no applied field; plate temperature is 119°F and room temperature is 69°F. In this exploratory run, no attempt was made to hold the plate temperature constant at high corona current values. At high values of corona current, plate temperature dropped to approximately 100°F with a constant heater current. The fringe pattern shown in this picture remains unchanged as the potential is applied as long as the current remains essentially zero. As soon as a slight current begins to flow, some changes in the pattern occur. This behavior is characteristic of all tests conducted with the corona discharge. The rods holding the fine wires are visible at the left. The "T" located at the bottom of the picture provides a reference length.

The initial disturbance of the thermal boundary layer, shown in View B, occurs just at the onset of corona current. Subsequent pictures, in sequence, show the marked distortion of the isothermal lines as the current is increased. The patterns shown are fairly steady for a given stabilized current except for Views D and E, which are slightly unsteady. The isothermal lines are extremely steady for currents in excess of $10 \mu a$. The pictures reveal that, depending upon the value of current, regions of increased or decreased heat transfer exist. The data on heat transfer coefficients, h_x, in this sequence are considered quite accurate for values of current less than $10 \mu a$. Above this value, sufficient plate cooling occurred to introduce some error in h_x. Consequently, no h_x data are presented for currents greater than $10 \mu a$. The values of the heat transfer coefficients corresponding to Views A through E are plotted in Figure 14. The heat transfer coefficient at various locations along the plate is plotted for several values of corona discharge current. The abscissa, x, represents the distance in the vertical direction along the plate surface; x = 0 represents the centerline of the plate, three inches from the bottom edge; distances to the right of x = 0 represent the lower part of the plate, and distances to the left represent the upper part of the plate. A marked change in the magnitude and distribution of h_x results from the applied electrical field. For small currents, the variation along the plate is extremely large, while for higher currents, the values of h_x tend to become more symmetric about the centerline.

Figure 15 presents the results of tests using the same configuration as in Figure 13 but the temperature difference between plate and room air is maintained constant throughout the test sequence. Stabilized test points were obtained and multiple records were made of the phenomena. Accurate data were obtained up to high values of current. View A shows the reference pattern with no applied field. Changes in the fringes are evident as the current is increased. At the higher values of current, the thermal boundary layer becomes extremely thin; it can be expected, therefore, that the heat transfer rate has increased greatly. Unfortunately, this extreme thinness of the boundary layer makes it difficult, if not impossible, to determine the local values of heat transfer coefficient. The heat transfer coefficients corresponding to this sequence of photographs are plotted in Figure 16. The reference curve with no field applied can be obtained with considerable accuracy. Values of heat transfer coefficient for the higher values of current indicate a larger degree of scatter, and could not be determined for the center of the plate.

The next series of tests, shown in Figure 17, was conducted with the electrode moved away from the plate to a distance of 5 cm. The temperature difference was maintained at 34°F. The thermal boundary layer is squeezed down as the field is increased. The main difference between this case and the previous one at corresponding high currents is that the thermal layer is thinned more uniformly across the plate. Corresponding values of heat transfer coefficient are plotted in Figure 18. Difficulties were again encountered in reducing the data at the higher current values.

A test sequence with the electrode moved out to 10 cm is shown in Figure 19. The higher currents were not reached in this case because the required voltage became excessively high. At high voltages, local points of corona discharge occurred on the plate and on discrete points of the wire. Such intense local discharges gave erroneous impressions of the value of the current driving the corona wind. Heat transfer coefficients are shown in Figure 20.

In the next sequence of tests, the heated plate was placed with the flat heated surface faced downward and the 0.004 inch wire electrode 2 cm away from the plate at the centerline. The temperature difference was held constant at 27°F. The influences on the isotherms as the current begins to flow for the range from 0 to 4.55 μa only are indicated in Figure 21. The gradual squeezing of the boundary layer is clearly evident. Other carefully controlled experiments indicated that the patterns shown is very symmetrical about the centerline for all values of current. The corresponding heat transfer coefficients are plotted in Figure 22. The method of presenting data for the horizontal plate is similar to that used for the vertical plate. Since the configuration was symmetrical about the centerline of the plate, however, data for only one half of the plate are plotted, from the centerline out to the edge. The gradual change in magnitude and distribtuion is clearly evident. The variation of h_x becomes bell-shaped as the current is applied. At the edge of the plate, where $x = 3$, the end effects cause a localized increase. This characteristic increase is evident in the curve for free convection with no field applied. It is interesting to notice that the local values of h_x can be changed several fold with currents of a few microamperes.

Figure 23 presents the results of another test sequence in which the same configuration was used, but the temperature difference was maintained at 27°F and the current range covers 0 μa to 159 μa. The thinning of the thermal boundary layer is quite evident. At the high values of current, the patterns resemble those found with the vertical plate. The heat transfer coefficients are plotted in Figure 24. The values at high currents and near the center tend to scatter as before.

10

In the next sequence of tests, the same configuration of horizontal plate is used, but the wire is moved to a distance of 5 cm and the temperature difference is maintained at 34°F. The results of the tests, shown in Figure 25, again indicate a thinning down of the boundary layer, but the shape is somewhat flatter than that with the electrode at 2 cm. The heat transfer coefficients plotted in Figure 26 show the changes in magnitude and distribution. Once again, at higher current values the data becomes scattered due to the difficulty of reading the interferograms. Large changes in the heat transfer coefficient again result from a small current flow.

Pressure Survey Data

Tests of the pressure rise obtained with a corona wind were conducted to provide data on the magnitudes of the pressures as well as the variation of the pressure along the plate. The test configuration consisted of locating a single wire electrode parallel to a 7 by 12-inch flat plate at the centerline. Wires measuring 0.0005, 0.004, and 0.010 inch in diameter were tested at various distances from the plate. The wire was oriented so that it ran parallel to the 7-inch dimension of the pressure plate. The pressure rise obtained at the centerline of the plate with the different size electrodes is shown in Figures 27, 28, and 29. All plots indicate an approximately linear pressure-current characteristic, which is in accordance with the theories of corona wind. Some zero shift occurred. A typical zero shift can be seen in the 2-cm case of Figure 29. A small influence of spacing of the wire can be noted, but trends due to wire spacing are not consistent as the wire size is changed. The magnitudes of the pressure for a given current, likewise, do not seem to be markedly influenced by wire size. No clear-cut trends of the effects of wire size or wire spacing can be determined from the data. All data presented in these three figures were taken with the Chattock micromanometer.

The next sequence of tests were conducted to investigate pressure distribution. Data were taken with the Chattock micromanometer. A 0.004-inch wire electrode was used at three wire spacings, 2 cm, 4 cm, and 6 cm. Results of these tests are plotted in Figures 30, 31 and 32. The magnitudes of the centerline pressures at a given current do not vary greatly, as had been indicated in the previous test data. The shape of the curves at all spacings is similar. Since testing had shown that the pressure distributions were symmetrical, only one-half of the distribution is shown. Because the corona discharge does not necessarily occur in a line perpendicular from the wire to the plane, some shift in the peak pressure position can be expected. Study of the curves, however, reveals that the centerline of the corona wind actually did move away from the geometric centerline of the plate in some cases.

Figure 33 presents the results of another series of tests at a 2-cm spacing to show the characteristic variability of the corona phenomenon. Data taken at the lower three currents were strongly affected by random zero shifts. Although the curves seem to be of reasonable proportion, a subsequent curve shows that these data are unusable.

Typical pressure distribtuions obtained with the inclined manometer are presented in Figure 34 to show the general shape of the pressure distribution curve. The absolute values of these data are not as accurate as those obtained with the Chattock manometer, but the curve has the same bell shape.

Current-Voltage Relations

The variation of current with applied voltage was measured often during the course of the testing. Since it proved difficult to relate the voltage to either test technique or data

interpretation, only one representative voltage curve will be presented. Figure 35 presents the results for a corona discharge with a 0.004-inch wire located at the centerline of a 7 x 12-inch flat plate and running in the direction of the 7-inch dimension. Data are presented for various wire spacings. It is believed that the results are typical of those found with corona discharge.

Discussion of Test Results

The purpose of this section is to describe in some detail the phenomena observed in the foregoing sequence of tests on the interferometer.

An unusual movement of the thermal boundary layer is shown in Figure 13. This phenomenon occurred in all runs with the vertical plate, and with several electrode configurations. At the initial flow of current, the isotherms are "pulled-out" from the heated plate. At somewhat greater currents this pull-out becomes larger. As the current was raised to even higher values, the pull-out disappeared. The cause of the pull-out was investigated in considerable detail. Pressure distribution measurements at low currents failed to provide any accurate data on the pressure field in the region of pull-out. The pull-out shape appeared to move opposite to the direction expected from corona wind action. Any dipole forces acting in the air should also have acted in a direction opposite to the pull-out. A possible explanation of the pull-out phenomenon lay in the action of two impinging fluid streams. With a heated vertical plate, a convective stream moves upward along the plate. If the corona wind strikes the plate, it can be expected that the air stream will split and try to move upward and downward. The corona stream moving downward will buck the upward streaming of the thermal boundary layer. It appears possible, therefore, that as the two fluid streams meet, the temperature field would change in an unanticipated manner. The possibility that the pull-out phenomenon was due to an interaction of the corona wind and the thermally heated stream was explored in the sequence of tests shown in Figures 21, 23, and 25. The corona wire was placed exactly at the center of an accurately leveled horizontal plate at a short distance below the plate. Upon application of the field, the center of the corona wind stream would be located at the point of zero longitudinal velocity of the thermal boundary layer. Thus, any corona stream striking the plate would split into two streams, each of which would move with the streaming in the thermal boundary layer. If no pull-out occurred, then the pull-out phenomenon must have been associated with the fluid flow impingement. Conversely, if pull-out did occur, then the phenomenon required some other explanation, and this, conceivably, could be a new type of interaction.

The tests with the horizontal plate were setup with the hot side up and the hot side down. The convective cells developed in free convection with the hot face up made it impossible to interpret the results. Tests with the hot side down and the corona wire at several spacings, however, were most successful, as shown in Figures 21, 23, and 25. As field is applied and the current flows, no pull-out is evident with either the 2 cm or 5 cm wire spacing. The experiments were repeated several times to verify results, and extreme caution was used so that extraneous disturbances did not introduce error. Since the pull-out did not occur, it was felt that the pull-out phenomenon observed with the vertical plate tests was due to the impingement of fluid streams, and not to an unexplained electrostatic effect.

ANALYTICAL STUDY OF THE EFFECT OF CORONA DISCHARGE
ON FREE-CONVECTION HEAT TRANSFER

The influence of the applied electric field on the heat transfer of the heated flat plate was analyzed in an attempt to learn possible trends that might occur and to aid in obtaining a better understanding of the phenomena. The analytical work is broken down into four phases: electrical field effects, heat transfer theory, the combined problem, and an approximate solution to the horizontal plate case.

ELECTRIC FIELD-CORONA DISCHARGE RELATIONS

In analyzing the corona discharge phenomena, it is essential to obtain relationships covering the field strength, current distribution, current-voltage relationships, and the induced pressure rise. The theory is based upon the recognition that a definite charge, ρ_c, exists. Two simple illustrations of solutions will be presented: a one-dimensional case, and a cylindrical-electrode configuration.

The electric field equations (from Ref. 1) are:

$$\overline{\nabla} \cdot \overline{E} = \frac{\rho_c}{\epsilon} \tag{1}$$

$$\overline{J} = \sigma_c \, \overline{E} + \rho_c \, \overline{v}_t \tag{2}$$

$$\overline{F} = \rho_c \, \overline{E} \tag{3}$$

Pressure Rise with Space Charge

In a gas where the total current carriers are associated with the ions, $\overline{J} = \rho_c \, \overline{v}_t$, where $\overline{v}_t$ is the total velocity of the moving charge. It is assumed that ions of only one sign exist away from the immediate vicinity of the corona point, and the mobility of these ions is approximately constant. (A discussion of the concept of ion mobility may be found in Reference 1.) Then, since the total velocity of the charge (ions) is equal to the sum of the gas motion and the ion motion, the following relationship exists:

$\overline{v}_t$ = velocity of ions relative to the gas + velocity of the gas.

The velocity of the ions relative to the gas is equal to KE. Therefore,

$$\overline{v}_t = K \overline{E} + \overline{v}$$

where $\overline{v}$ is gas velocity. The current density becomes

$$\overline{J} = \rho_c \, \overline{v}_t$$

$$= \rho_c \, (K \overline{E} + \overline{v}) \tag{4}$$

using

$$\dot{\rho}_c = \epsilon \, (\overline{\nabla} \cdot \overline{E})$$

13

and

$$\overline{J} = \epsilon \, (\overline{\nabla} \cdot \overline{E}) \, (K\overline{E} + \overline{v}) \tag{5}$$

Considering the relative magnitudes of $K\overline{E}$ and $\overline{v}$ for a typical case of corona wind:

$$K \cong \frac{2 \text{ cm}^3}{\text{volt-sec}}$$

$$E \cong \frac{10000 \text{ volts}}{2 \text{ cm spacing}} = \frac{5000 \text{ volts}}{\text{cm}}$$

$$KE \cong 100 \text{ m/sec}$$

The usual air velocities in a corona discharge are below 5 m/sec. Thus, v is considerably smaller than KE in this case and will be neglected. If air is blown past the corona point at higher velocities, then v could become significant (Ref. 6). Therefore:

$$\overline{J} \cong \rho_c \, K\overline{E} = K \epsilon \, (\overline{\nabla} \cdot \overline{E}) \, \overline{E} \tag{6}$$

In the stagnation region under the impinging corona wind stream, velocities will be very small. The boundary layer thickness in this region will likewise be very small, and the pressure across the boundary layer will be approximately constant. Consequently, the pressure rise due to the electrical field will occur in the region of the air where essentially nonviscous potential flow occurs. Consequently, in the Navier Stokes equations (Refs. 9, 10):

$$\rho \, \frac{du_i}{d\tau} = X_i - \frac{\partial p}{\partial x_i} + \mu \nabla^2 u_i + \frac{\mu}{3} \, \frac{\partial \Delta}{\partial x_i} \tag{7}$$

$$\overline{X} = \overline{F} \, ; \qquad \Delta \equiv \frac{\partial u_i}{\partial x_i} \, ,$$

where $\overline{F}$, the electrical body force, is equal to $\overline{X}$, the body force exerted on the fluid. The pressure gradient and the electric field body forces are of considerably greater magnitude than the viscous or inertia forces, and consequently the Navier Stokes equations reduce to:

$$\overline{\nabla} p = \rho_c \, \overline{E} \tag{8}$$

and

$$\overline{\nabla} p = \frac{\overline{J}}{K} \tag{9}$$

follows. This indicates that pressure gradient is proportional to current density and inversely proportional to ion mobility. In a one-dimensional case, Equation (9) becomes

$$\frac{\partial p}{\partial y} = \frac{J}{K}$$

14

$$p = \int_{y_0}^{y_1} \left(\frac{J}{K} \right) dy \qquad (10)$$

In a one-dimensional model of cross-section A, the current density would be related to the current, i, by:

$$J = \frac{i}{A}$$

Therefore:

$$p = \frac{i}{KA} \int_{y_0}^{y_1} dy = \left(\frac{i}{KA} \right) (y_1 - y_0) \qquad (11)$$

This predicts a linear rise in pressure as either the current or the electrode spacing is increased. y_0 is a reference distance located a very short distance away from the region of intense corona discharge.

If the electrode geometry is cylindrical, then for a constant current,

$$J = \frac{i}{A}$$

and A is given as a function of radius by:

$$A = \ell \, r \, \theta_c$$

where:

ℓ is the length of the fine wire electrode,

θ_c is the angle subtended by the outer electrode,

and

r is the radius.

Therefore:

$$p = \int_{r_0}^{r_1} \left(\frac{J}{K} \right) dr$$

$$= \left(\frac{i}{K \ell \theta_c} \right) \int_{r_0}^{r_1} \frac{dr}{r}$$

$$= \left(\frac{i}{K \ell \theta_c} \right) \ell n \frac{r}{r_0} \qquad (12)$$

If the outer electrode radius is R, and the reference radius at the edge of the intense corona is r_0, then the pressure at R is:

$$p = \left(\frac{i}{K \ell \theta_c} \right) \ell n \frac{R}{r_0} \qquad (13)$$

This relationship would indicate that the pressure is once again proportional to the current, but varies as the logarithm of the radii ratio as either the spacing or the wire size is changed.

15

If relationships between field strength and current are desired, then it can be shown (Refs. 2, 8) for the linear case:

$$E^2 - E_0^2 = \frac{2i}{\epsilon K A} (y - y_0) \tag{14}$$

where:

$$E = E_0 \quad @ \quad y = y_0$$

For the cylindrical case, the relationship can be shown to be:

$$E^2 = \left(\frac{2i}{\epsilon K}\right) + \frac{C_r}{r^2} \tag{15}$$

$$C_r = (r_a E_a)^2 - 2i \frac{r_a^2}{\epsilon K} \tag{16}$$

where E_a is the field strength at r_a (Ref. 2).

A complete listing of the various relationships of current, voltage, and pressure for simple geometrics is given by Steutzer in Reference 7.

Cobine (Ref. 2) derives the relationship between corona current and applied voltage for a cylindrical electrode configuration in the form

$$i = \frac{2 K V (V - V_c)}{R^2 \ell n \frac{R}{r_a}} \tag{17}$$

where V_c is the voltage at which the corona starts.

He points out that the general relationship between current and voltage for corona discharge is of the form

$$i = CV (V - V_c) \tag{18}$$

where C is a constant which depends primarily upon the geometry of the system. This form has been checked by many investigators and has been found to hold quite well at low current values.

To determine the pressure rise between the fine wire and flat plate configuration used in the experiments, attempts were made to derive the relationships between the space-charge-limited current, voltage, and pressure. The boundary conditions in the problem of a round cylinder at one side and a flat surface at the other side proved difficult to handle mathematically. Since it was desirable to have explicit equations for the field and current distribution, numerical solutions and representations were not attempted. Approximations based upon a cylindrical configuration were tried, but the correlation between these approximations and the pressure curves from the test data was very poor.

Pressure Rise with Low Charge Density

Since small currents had produced very significant results in the experiments, the possible use of the space-charge-free field equations was investigated. Without space charge, the problem of determining the field becomes elementary. The case of a long wire above an infinite conducting plane is covered in many sources (Refs. 11, 12, 13). For close spacing and small wire size, it was assumed that the test configuration might be represented adequately by the following theoretical model.

The equations for the two-dimensional field based upon the method of images as adapted from Reference 11 are:

$$E_x = \frac{\lambda}{2\pi\epsilon} \left[\frac{x}{R_1^2} - \frac{x}{R_2^2} \right] \tag{19}$$

$$E_y = \frac{\lambda}{2\pi\epsilon} \left[\frac{y+a}{R_1^2} - \frac{y-a}{R_2^2} \right] \tag{20}$$

where the various distances are represented in Figure 36 and λ represents charge per unit length.

At the surface of the plate $y = 0$, and $R_1 = R_2 = R$. This leads to the following relations:

$$E_x = 0 \text{ at the plane surface}$$

and

$$E_y = \frac{\lambda}{\pi\epsilon} \left[\frac{a}{x^2 + a^2} \right] \tag{21}$$

where $R^2 = a^2 + x^2$.

The equation for voltage is:

$$V = \frac{\lambda}{2\pi\epsilon} \ln \frac{2a}{r_a} , \tag{22}$$

which is valid for large spacings relative to wire size. Therefore:

$$E_y = \frac{2\left(\frac{V}{a}\right)}{\ln\left(\frac{2a}{r_a}\right)} \left[\frac{a^2}{x^2 + a^2} \right] . \tag{23}$$

Letting $Z = x/a$

$$E_y = \frac{2\left(\frac{V}{a}\right)}{\ln\left(\frac{2a}{r_a}\right)} \left[\frac{1}{1 + Z^2} \right] . \tag{24}$$

The relationship for the pressure in a dielectric due to the applied electrostatic field (Refs. 14, 15) is given by:

$$\Delta p = \frac{1}{2} \epsilon E^2 \tag{25}$$

Strictly speaking, this relationship holds only for the pressure rise in a dielectric between two parallel plates. It does not hold precisely for a corona discharge. However, Stuetzer (Ref. 7) indicates that relationships of the form

$$\Delta p = \frac{1}{2} \epsilon E_{max}^2 \cdot (G)$$

hold quite well for corona discharges. G is a constant which depends on geometry. The maximum value for E will occur near the plate where E_x is small. Consequently, as an approximation

$$\Delta p = \frac{1}{2} \epsilon E_y^2 (G) \tag{26}$$

with the constant (G) left undetermined for the moment.

Using this relationship and Equation (25), the expression for pressure can be written:

$$\Delta p = 2 \epsilon \left[\frac{(\frac{V}{a})}{\ln(\frac{2a}{r_a})} \right]^2 \left[\frac{1}{1+z^2} \right]^2 (G) \tag{27}$$

When x = 0, z = 0, pressure at the centerline can be expressed by:

$$\Delta p_c = 2 \epsilon \left[\frac{(\frac{V}{a})}{\ln(\frac{2a}{r_a})} \right]^2 (G) \tag{28}$$

where p_c is centerline pressure.

If for convenience, the reference atmospheric pressure is assumed to be zero, then $\Delta p_c = p_c$. Therefore:

$$\frac{p}{p_c} = \left[\frac{1}{1+z^2} \right]^2 \tag{29}$$

This expression provides a pressure distribution over the flat plate, assuming there are no space charge effects, that $p = \frac{1}{2} \epsilon E^2 (G)$, and that the influence of E_x is relatively small.

Equation (29) is plotted in Figure 37. To check whether this expression would provide a reasonable representation of the actual phenomena, it was compared with the experimental data and the results are plotted in Figures 38, 39, and 40. These figures present the same pressure distribution data as was presented in Figures 30, 31, and 32, except that the data have been normalized by dividing the magnitudes of all pressures by the centerline peak pressure. The distances along the plate were transformed by introducing a new variable, Z (Z = x/a, and a is the distance from the wire to the plate). These plots show that the form of the pressure distribution for a given wire spacing remains approximately the

same as the current is varied widely. In addition, the shape of the distribution remains essentially the same with changes in the spacing. The normalized distribution is more peaked with the 6-cm spacing, but the differences are not large. Large changes, however, can arise from small zero shifts in the micromanometer. These effects are shown in Figure 41, which presents the normalized data of Figure 33. Data obtained at the lower three values of current had small random shifts in the zero reference of the manometer. As can be seen from Figure 41, the wide variance makes these data unusable.

As can be noted from Figures 38, 39, and 40, correlation between the shape of the pressure curves for the test data and for theory is quite good at smaller values of a; at larger values of a, however, correlation becomes poorer. This may possibly be attributed to the fact that the assumed infinite plane of the two-dimensional model becomes a poor approximation as the spacing becomes large. Based upon this comparison with the test data, the variation

$$\frac{p}{p_c} = \left[\frac{1}{1 + z^2} \right]^2$$

is considered a reasonable representation so long as a is considered small. The variation provides information on the shape of the pressure distribution only.

In attempting to calculate p_c from the form

$$p_c = 2\epsilon \left[\frac{\frac{V}{a}}{\ln \left(\frac{2a}{r_a} \right)} \right]^2 (G) ,$$

it was found to be difficult to determine the geometric constant G because of the boundary conditions mentioned in the space-charge case. Consequently, the data obtained during the pressure tests were used in calculating center pressures. The relationship between center-line pressures and current was in accord with the equations for the one-dimensional case and the cylindrical configuration.

One-dimensional: $\quad p = \dfrac{i}{KA} \, (y - y_0)$ $\hspace{3cm}$ (11)

Cylindrical: $\quad p = \dfrac{i}{K \ell \theta_c} \, \ln \left(\dfrac{R}{r_a} \right)$ $\hspace{3cm}$ (13)

The test data shown in Figures 27, 28, and 29 verify the linear relationship of pressure and current. Using $p = c_1 i$, the constant c_1 becomes essentially a geometric shape factor for a given ion mobility. c_1 then is determined from Figures 27, 28, or 29 for the specific wire size and wire spacing chosen.

Thus, in establishing the mathematical model of the pressure produced, an experimental constant has been introduced. The resulting expression, however, has the advantage of being quite simple in form.

CONVECTIVE HEAT TRANSFER WITHOUT APPLIED ELECTRIC FIELDS

A brief summary of relevant heat transfer problems will be given to provide a background for this work. Flat-plate forced convection, vertical-plate free convection, and

stagnation-point heat transfer will be covered. The starting point for solving all three cases is with the following equations (Ref. 9):

Continuity:

$$\frac{\partial u_i}{\partial x_i} = 0 \tag{30}$$

Navier Stokes:

$$\rho \frac{d u_i}{d \tau} = X_i - \frac{\partial p}{\partial x_i} + \mu \nabla^2 u_i + \frac{\mu}{3} \frac{\partial \Delta}{\partial x_i} \tag{7}$$

Energy:

$$\rho \frac{d C_p T}{d \tau} = \frac{1}{J_m} \frac{dp}{d\tau} + \frac{\partial}{\partial x_i} \left(k \frac{\partial T}{\partial x_i} \right) + \frac{\mu}{J_m} \Phi - \frac{1}{J_m} u_i X_i + q_r + q_g \tag{31}$$

where:

$$\Phi = 2 \left\{ \left(\frac{\partial u}{\partial x} \right)^2 + \left(\frac{\partial v}{\partial y} \right)^2 + \left(\frac{\partial w}{\partial z} \right)^2 + \left(\frac{\partial u}{\partial y} + \frac{\partial v}{\partial x} \right)^2 \right.$$

$$\left. + \left(\frac{\partial w}{\partial y} + \frac{\partial v}{\partial z} \right)^2 + \left(\frac{\partial u}{\partial z} + \frac{\partial w}{\partial x} \right)^2 - \frac{2}{3} \Delta^2 \right\} \tag{32}$$

q_r = radiation energy

q_g = internal heat generated

X_i = a body force

τ = time

$\Delta \equiv \frac{\partial u_i}{\partial x_i}$.

Forced Convection-Laminar Flow

With the usual assumptions of Blasius flow (Refs. 4, 16), the equations for the case of heat transfer to a flat plate in laminar flow become

Continuity:

$$\frac{\partial u}{\partial x} + \frac{\partial v}{\partial y} = 0 \tag{33}$$

Navier Stokes:

$$u \frac{\partial u}{\partial x} + v \frac{\partial u}{\partial y} = \nu \frac{\partial^2 u}{\partial y^2} \tag{34}$$

20

Energy:

$$u \frac{\partial T}{\partial x} + v \frac{\partial T}{\partial y} = \alpha \frac{\partial^2 T}{\partial y^2} + \frac{\nu}{J_m C_p} \left(\frac{\partial u}{\partial y} \right)^2 . \tag{35}$$

Use of the stream function

$$\Psi = (\nu \times U)^{\frac{1}{2}} f (\eta) \tag{36}$$

and the transformation

$$\eta = y \left(\frac{u_\infty}{\nu x} \right)^{\frac{1}{2}} .$$

allows the Navier Stokes equations to be transformed to an ordinary differential equation

$$f'''(\eta) + \frac{1}{2} f(\eta) f''(\eta) = 0 \tag{37}$$

the solution for which is tabulated in many sources (Refs. 4, 10). The energy equation is handled through the same transformation and becomes:

$$\frac{d^2 T}{d \eta^2} + \frac{f}{2} N_{Pr} \frac{dT}{d\eta} = \left(\frac{-u_\infty^2}{J_m C_p} \right) N_{Pr} f''^2 . \tag{38}$$

The solution to this equation is given by:

$$h_x = - k \left(\frac{u_\infty}{\nu x} \right)^{\frac{1}{2}} \left[\frac{(f'')^{N_{Pr}}}{\int_0^\infty (f'')^{N_{Pr}} d\eta} \right]_{\eta = 0} \tag{39}$$

A reasonable approximation to this solution (Ref. 17) is given by:

$$h_x = k \left(\frac{u_\infty}{\nu x} \right)^{\frac{1}{2}} (0.332 N_{Pr}^{\frac{1}{3}}) \tag{40}$$

where N_{Pr} is the Prandtl Number.

Free Convection Vertical Plate

In the free convection from a vertical plate, a body force arises due to the effect of gravity. The equations in this case become (Ref. 9):

Navier Stokes:

$$\rho \left(u \frac{\partial u}{\partial x} + v \frac{\partial u}{\partial y} \right) = X - \frac{\partial p}{\partial x} + \mu \frac{\partial^2 u}{\partial y^2} \tag{41}$$

Energy:

$$u \frac{\partial T}{\partial x} + v \frac{\partial T}{\partial y} = \frac{k}{\rho C_p} \frac{\partial^2 T}{\partial y^2} . \tag{42}$$

21

The transformation of the equations in this case uses

$$\Psi = 4 \nu c x^{\frac{3}{4}} F(\eta)$$

$$\eta = \frac{cy}{x^{\frac{1}{4}}}$$

$$c = \sqrt[4]{\frac{g(T_w - T_o)}{4 \nu^2 T_o}}$$

where

T_o = free stream temperature

T_w = wall temperature

$\theta = T-T_o/T_w-T_o$.

The equations then become:

Navier Stokes:

$$F''' + 3 FF'' - \overline{F'}^2 + \theta = 0 \tag{43}$$

Energy:

$$\theta'' + 3 N_{Pr} F \theta' = 0 \tag{44}$$

Solutions for this set of equations are listed in References 4 and 10.

Stagnation-Point Heat Transfer

The stagnation-point problem arises when a fluid stream impinges upon a surface and a zone of zero velocity is formed under the stream. The case of an infinite stream striking a cylinder or flat plate is well covered in the literature (Refs. 9, 16). Both theoretical and experimental evidence support the assertion used in the solutions that the velocity of the flow outside of the boundary layer increases linearly from the stagnation point. This variation holds only in the vicinity of the stagnation point, but it is most useful.

Using the relationship $U_\infty = \beta_1 x$, the pressure gradient term in the Navier Stokes equations becomes:

$$- \frac{1}{\rho} \frac{\partial p}{\partial x} = \beta_1^2 x \tag{45}$$

and the Navier Stokes equations become:

$$u \frac{\partial u}{\partial y} + v \frac{\partial u}{\partial y} = \beta_1^2 x + \nu \frac{\partial^2 u}{\partial y^2} \tag{46}$$

22

Using

$$\Psi = (\nu \beta_1)^{\frac{1}{2}} \times F(\eta)$$

$$\eta = \left(\frac{\beta_1}{\nu}\right)^{\frac{1}{2}} y$$

the equation is transformed to the ordinary equation

$$F''' + FF'' - (F')^2 + 1 = 0. \tag{47}$$

The energy equation for this case is given by

$$u \frac{\partial T}{\partial x} + v \frac{\partial T}{\partial y} = \frac{k}{\rho c_p} \frac{\partial^2 T}{\partial y^2} \tag{48}$$

which, with the transformation, becomes

$$\theta'' + N_{Pr} F \theta' = 0 \tag{49}$$

where

$$\theta = \frac{T - T_w}{T_0 - T_w}.$$

The solution of these equations is given in Reference 16.

The foregoing brief sketch of three of the fundamental problems of convective heat transfer are included solely as background material. Some of the efforts made in tackling the problem of heat transfer with corona discharge were based upon the concepts involved in these solutions. Their inclusion provides for ready reference.

COMBINED CORONA WIND-CONVECTION PROBLEM

In order to formulate a suitable mathematical model, it is necessary to set down as completely as possible the physical system to be described. In the present work, two separate physical cases will be considered. The corona wind impinging on a horizontal plate with the bottom heated constitutes one case, and the corona wind impinging on a heated vertical plate constitutes the second. These two systems are shown in Figures 42 and 43. In the first case, the bouyancy force is symmetrical about the center of the plate. Any streaming due to thermal bouyancy or corona wind is additive and no regions of stagnation should exist.

The bouyancy force in the case of the horizontal plate acts somewhat differently from that for the vertical plate. For a vertical plate, the bouyancy force acts along the plate, and causes the convective streaming to move along the surface. For a horizontal plate, the bouyancy force acts perpendicular to the plate, and any streaming occurs because of the upward movement of the heated air at the edge of the plate. Consequently, in the center of the plate, the bouyancy force which acts perpendicular to the small streaming taking place will be neglected in the analysis of the horizontal plate.

23

The vertical plate presents an interesting but formidable problem. The same complex additive corona effects and thermal effects occur as in the first case, and in addition, the magnitude of corona wind will approach that of the free-convection streaming at certain values of current. Thus, at least two separate problems present themselves. In the region above the centerline of the impinging jet of air, the two streams will be additive and a combined free-convection and forced-convection problem results. The thermal body force in this case is in the same direction as the external corona wind stream. In the region below the centerline, the situation is changed. Here the corona wind streams in the opposite direction to the thermal body force. At some value of current, the magnitude of the corona wind will be approximately the same as that of the upward streaming heated air. Although it is doubtful that the distribution of velocity in the two streams as they impinge will be the same, the net result is that some type of stagnation region should result. This complex problem is illustrated graphically by the interferometer pictures of the vertical heated plate shown in Figure 13.

The approaches used in attempting to solve these problems included consideration of solutions of the Navier Stokes and energy equations with the concept of an impinging two-dimensional finite jet, and the use of the Von Karman integral equations.

Two-Dimensional Jet Approach

Study of all the data and photographs of the corona wind indicated that the cross section of the impinging jet of air appeared to be very narrow before it was deflected by the plate. Pictures of both the horizontal plate and the vertical plate at high currents indicated that the streaming after impingement was approximately symmetrical. A possible model then was conceived to be a thin two-dimensional jet of air impinging upon a flat surface. The case of the horizontal plate with the thermal body force included was considered from this viewpoint first. If this approach would turn out to be promising it was felt that the width of the jet could be determined from the test data.

The case of the horizontal flat plate with an impinging jet was considered in the following manner. As a first approximation, it was assumed that the viscosity and boundary layer would not markedly influence the flow field and pressure distribution of the jet of air. This assumption allowed the use of potential flow theory in the region away from the surface of the plate. One possible technique for handling this case is by using the hodograph transformation (Refs. 18, 19). The problem is shown in Figure 44.

Using the transformation

$$\zeta = \frac{(u - iv)}{U} , \tag{50}$$

the jet is mapped onto the upper half of the unit circle.

$$t = -\frac{1}{2} \left(\zeta + \frac{1}{\zeta} \right)$$

maps the upper half of the unit circle onto the upper half of the t plane. The flow in the t plane is equivalent to a source flow of strength $\frac{Ub}{\pi}$.

The complex potential $w(z) = u + iv$ becomes, for this case:

24

$$w(z) = \frac{Ub}{2\pi} \ell_n \left(\frac{t^2}{t^2 - 1} \right)$$

$$= \frac{Ub}{2\pi} \ell_n \left(\frac{\zeta^2 + 1}{\zeta^2 - 1} \right) \tag{51}$$

Using $\frac{dw}{dz} = \frac{dw}{d\zeta} \frac{d\zeta}{dz}$, it can be shown that

$$dz = \frac{2b}{\pi} \left(\frac{1}{\zeta^2 - 1} - \frac{1}{\zeta^2 + 1} \right)$$

from which

$$\frac{z}{b} = \left(\frac{2}{\pi} \right) \left(\tan^{-1} \zeta + \tanh^{-1} \zeta \right). \tag{52}$$

At the surface of the plate, $v = 0$ and this equation becomes

$$\frac{x}{b} = \left(\frac{2}{\pi} \right) \left(\tan^{-1} \frac{u}{U} + \tanh^{-1} \frac{u}{U} \right). \tag{53}$$

This is an implicit equation. Expressing the terms in series and reducing the equation,

$$\frac{x}{b} \cong \frac{4}{\pi} \left[\left(\frac{u}{U} \right) + \frac{1}{5} \left(\frac{u}{U} \right)^5 + \frac{1}{9} \left(\frac{u}{U} \right)^9 + \frac{1}{13} \left(\frac{u}{U} \right)^{13} + \cdots \right] \tag{54}$$

Using a reversion of series technique

$$\frac{u}{U} = \frac{\pi x}{4b} \left[1 - \frac{1}{5} \left(\frac{x}{b} \right)^4 + \cdots \right]. \tag{55}$$

The form of the equations for velocity and pressure calculated on an incompressible basis is shown in Figure 45.

The most revealing aspect of this figure is that the linear term of the expression for u/U holds quite well in the vicinity of the centerline. If the pressure and velocity relationship of the corona-wind jet would be similar to these curves, then, potentially, a very simple calculation for boundary layer profile and heat transfer could be made. In the central region where $x < \frac{4u}{\pi U} b$, the stagnation solution discussed previously would apply, and in the outer region where $x > \frac{4u}{\pi U} b$, the flat-plate laminar flow solution would apply.

A comparison between the theoretical thin-jet pressure distribution and a typical pressure distribution obtained from test is shown in Figure 46. Several attempts were made to adjust the relative shapes of the curve by choosing various values of b, the theoretical jet half-width. Since the form of the pressure curves did not agree well with the test curves, it could be expected that correlation with heat transfer coefficients based upon this method would also not be very good.

Navier Stokes Approach

Since both the test data and the thin-jet theory indicated that large pressure variations would be confined to a region close to the centerline, it was felt that the combined thermal body force-corona wind problem could be tackled in the outer regions of the plate, assuming the wind velocity in this region to be approximately constant. The physical model which was considered next was that of the second case as represented by Figure 43. This figure illustrates the two regions of flow, above the centerline and below the centerline. If the free-convection effects are large, and the upper half of the plate is considered, then the body force acts in the direction of external flow. In this case, the body force is:

$$\rho \, g \left(\frac{T_w - T_0}{T_0} \right)$$

In the region away from the centerline, the equations become:

Navier Stokes:

$$u \frac{\partial u}{\partial x} + v \frac{\partial u}{\partial y} = g \left(\frac{T_w - T_0}{T_0} \right) \theta + \nu \frac{\partial^2 u}{\partial y^2} \tag{56}$$

Energy:

$$u \frac{\partial T}{\partial x} + v \frac{\partial T}{\partial y} = \alpha \frac{\partial^2 T}{\partial y^2} \tag{57}$$

where the term $\left(\frac{\nu}{J_m C_\rho} \right) \left(\frac{\partial u}{\partial y} \right)^2$ is dropped from the energy equation because the velocities are extremely small. This set of equations is, of course, exactly the same set as was used for the free-convection vertical plate. The significant change in the problem comes with the different boundary conditions. As the corona wind streams over the surface, the velocity distribution will vary from zero at the surface to some maximum away from the surface and then decay back to zero at a distance farther out from the plate. The shape of this total distribution is complex. The simpler problem of the spreading of a free jet is even difficult to handle. In the case of corona discharge, it is difficult to know the form of the highly localized velocity distribution, and consequently the shape of the wake is in doubt. This shape would form the outer region of the corona wind after it turned the corner. On the other hand, the width of the boundary layer growing beneath the corona wind would be very small for some distance away from the center stagnation region. It was assumed, consequently, that the thickness of the corona wind would be large relative to the boundary layer thickness, and that the velocity at the edge of the boundary layer would be the velocity of the peak of the corona wind. These assumptions are represented in Figure 47 where schematic representations of temperature and velocity profiles are shown. U_∞, the impinging velocity, is the velocity of the corona discharge.

Using the free-convection transformations, equations (56) and (57) become:

$$F''' + 3 F F'' - 2 (F')^2 + \theta = 0 \tag{58}$$

$$\theta'' + 3 N_{Pr} F \theta' = 0 \tag{59}$$

26

The boundary conditions are:

$$y = 0, \quad \eta = 0, \quad u = 0, \quad v = 0, \quad T = T_w$$

$$y \to \delta, \quad \eta \to \infty, \quad u = u_\delta, \quad v = 0, \quad T = T_0$$

which lead to:

$$F = 0, \quad F' = 0, \quad \theta = 1, \quad @ \quad y = 0$$

$$F'' = 0, \quad F' = \frac{U}{4 \nu c^2 x^{\frac{1}{2}}} \quad @ \quad y \to \delta$$

These relationships imply that the boundary conditions change at every position up the wall. If this approach is used, solutions for the equations would have to be made in discrete steps for selected values of x.

For the case with the body force acting in the direction opposite to the direction of flow (Ref. 20), the sign of the body force term is changed and the equations become

$$F''' + 3 F F'' - 2 (F')^2 - \theta = 0 \tag{60}$$

$$\theta'' + 3 N_{Pr} F \theta' = 0 \tag{61}$$

The boundary conditions are the same as for the previous case. Consequently, a solution proceeding in this fashion would have to be done in discrete steps also.

Different forms for the transformations were tried, but no clear-cut approach for handling the combined free convection-forced convection was evident. Since a review of other combined convection work did not reveal anything directly applicable, it was decided to follow the integral equation approach.

Von Karman Integral Equation Approach

The integral equations of boundary layer and heat transfer theory for steady flow (Ref. 10) are given as:

Momentum:

$$\frac{\partial}{\partial x} \int_0^\delta \rho u^2 \, dy - u_0 \frac{\partial}{\partial x} \int_0^\delta \rho u \, dy = -\delta \frac{\partial p}{\partial x} - g \int_0^\delta \rho \left(\frac{T - T_0}{T_0} \right) dy - \mu \left(\frac{du}{dy} \right)_{y=0} \tag{62}$$

Energy:

$$J_m C_p \left[\frac{\partial}{\partial x} \int_0^{\delta_T} \rho u T \, dy - T_0 \frac{\partial}{\partial x} \int_0^{\delta_T} \rho u \, dy \right] - \int_0^{\delta_T} u \frac{\partial p}{\partial y} \, dy = -J_m k \left(\frac{\partial T}{\partial y} \right)_{y=0} + \mu \int_0^{\delta_T} \left(\frac{\partial u}{\partial y} \right)^2 dy \tag{63}$$

where δ_T is the thickness of the thermal boundary layer. Because the velocities involved in the phenomenon are so small, the viscous dissipation term was dropped in the energy equation.

27

The procedure used in solving the integral equations is to assume reasonable forms for the velocity and temperature distributions in the boundary layer which meet certain prescribed boundary conditions. Although the technique is not precise, it does offer insight into the problem as well as provide solutions useful in engineering.

ANALYTICAL SOLUTION OF THE HORIZONTAL PLATE CASE

In the application of the Von Karman integral equations to the case of heat transfer from the bottom of a heated flat plate subject to corona wind, it was assumed that the thermal body force was small and could be neglected. The integral equations then become:

$$\frac{\partial}{\partial x} \int_0^\delta \rho u^2 \, dy - u_0 \frac{\partial}{\partial x} \int_0^\delta \rho u \, dy = -\delta \frac{\partial p}{\partial x} - \mu \left(\frac{\partial u}{\partial y} \right)_{y=0} \tag{64}$$

$$J_m C_p \left[\frac{\partial}{\partial x} \int_0^{\delta_T} \rho u T \, dy - T_0 \frac{\partial}{\partial x} \int_0^{\delta_T} \rho u \, dy \right] - \int_0^{\delta_T} u \frac{\partial p}{\partial x} = - J_m k \left(\frac{\partial T}{\partial y} \right)_{y=0} \tag{65}$$

In this case, it was decided to attempt to determine what variation in boundary-layer thickness and heat transfer coefficient could be obtained throughout the entire range, from the centerline outwardly. The body force effects due to the applied electrical field were included through the use of the pressure rise distribution previously derived under the section on electric field-corona discharge relations. Thus, the analysis consisted primarily of determining the variations of boundary-layer thickness and heat transfer coefficients under the influence of a prescribed pressure distribution.

Pressure-Velocity Relation

In considering the fluid flow in the region of the impinging jet of corona wind, it is necessary to examine the nature of the relationship between velocity and pressure. For incompressible flow, Bernoulli's equation holds. If, however, a body force is introduced, the relationship is not as simple, even if the viscous effects are considered small. From thermodynamic reasoning it can be shown that if work is done on the fluid, for example by the body force, then the constant of integration will change across streamlines, and the condition of irrotationality will not hold even for incompressible flow. Because of this, one cannot assume the relationship $p_c = p + \frac{1}{2} \rho u^2$ will hold throughout the fluid stream above the boundary layer without more careful consideration.

In the region outside the boundary layer, the viscous effects can be considered small and, consequently, the Navier Stokes equations become

$$\rho \left(u \frac{\partial u}{\partial x} + v \frac{\partial u}{\partial y} \right) = X - \frac{\partial p}{\partial x} \tag{66}$$

$$\rho \left(u \frac{\partial v}{\partial x} + v \frac{\partial v}{\partial y} \right) = Y - \frac{\partial p}{\partial y} \tag{67}$$

If $X_i = \rho_c E_i$, using $E_i = \frac{\partial V}{\partial x_i}$

where V is the potential (voltage), then

$$X_i = -\rho_c \frac{\partial V}{\partial x_i} \tag{68}$$

28

For very small currents, if ρ_c is assumed to be a scalar constant other than zero,

$$X_i = - \frac{\partial \rho_c V}{\partial x_i} \tag{69}$$

and the equations for incompressible flow become:

$$u \frac{\partial u}{\partial x} + v \frac{\partial u}{\partial y} = - \frac{1}{\rho} \frac{\partial}{\partial x} (p + \rho_c V)$$

$$u \frac{\partial v}{\partial x} + v \frac{\partial v}{\partial y} = - \frac{1}{\rho} \frac{\partial}{\partial y} (p + \rho_c V) \tag{70}$$

Then

$$\left(u \frac{\partial u}{\partial x} + v \frac{\partial u}{\partial y} \right) dx = - \frac{1}{\rho} d (p + \rho_c V) \tag{71}$$

$$\left(u \frac{\partial v}{\partial x} + v \frac{\partial v}{\partial y} \right) dy = - \frac{1}{\rho} d (p + \rho_c V).$$

Therefore:

$$\left(u \frac{\partial u}{\partial x} + v \frac{\partial u}{\partial y} \right) dx - \left(u \frac{\partial v}{\partial x} + v \frac{\partial v}{\partial y} \right) dy = 0. \tag{72}$$

Letting

$$M = u \frac{\partial u}{\partial x} + v \frac{\partial u}{\partial y}$$

$$N = - \left(u \frac{\partial v}{\partial x} + v \frac{\partial v}{\partial y} \right)$$

$$Mdx + Ndy = 0, \tag{73}$$

using Green's theorem for the plane (Ref. 21)

$$\iint_A \left(\frac{\partial M}{\partial y} - \frac{\partial N}{\partial x} \right) dx dy = - \int_C (Mdx + Ndy), \tag{74}$$

and

$$\frac{\partial u}{\partial x} + \frac{\partial v}{\partial y} = 0, \tag{30}$$

it can be shown that

$$u \left(\frac{\partial^2 v}{\partial x^2} + \frac{\partial^2 v}{\partial y^2} \right) = v \left(\frac{\partial^2 u}{\partial x^2} + \frac{\partial^2 u}{\partial y^2} \right). \tag{75}$$

29

This condition holds for all values of u and v if $\nabla^2 u = 0$, $\nabla^2 v = 0$, and implies that if ρ_c can be considered a scalar constant, then irrotationality will follow. The foregoing demonstrates that the use of the condition of irrotationality is reasonable for the case of very small space charge. Therefore:

$$\left(u\, \frac{\partial u}{\partial x} + v\, \frac{\partial v}{\partial x} \right) dx = - \frac{1}{\rho}\, d\, (\, p + \rho_c V\,) \tag{76}$$

$$\rho_{\overline{2}}\, (\, u^2 + v^2\,) = -\, p - \rho_c\, V + p_0$$

$$p + \rho_{\overline{2}}\, (\, u^2 + v^2\,) = p_0 - \rho_c\, V \tag{77}$$

where p_0 is the constant of integration. Near the flat plate surface, $v = 0$, and V approaches zero. Consequently, Bernoulli's equation holds approximately near the wall:

$$p + \rho_{\overline{2}}\, u^2 = p_0 . \tag{78}$$

When $x = 0$, $u = 0$, $p = p_c$, it follows that $p_0 = p_c$, where p_c is the pressure at the center-line of the corona discharge.

Using the relation previously derived for the pressure variation under a corona discharge,

$$p = p_c \left[\frac{1}{1 + z^2} \right]^2 \tag{29}$$

the Bernoulli equation becomes:

$$\rho\, \frac{u^2}{2} = p_c \left[1 - \left(\frac{1}{1 + z^2} \right)^2 \right] \tag{79}$$

With this relation, the solution of the integral equations can be undertaken. Three forms of velocity and temperature profiles are assumed: linear, parabolic, and cubic. Because the parabolic distribution solution provides the clearest picture of the techniques involved, it will be carried through completely. The linear and cubic solutions will be indicated only.

Parabolic Solution

The parabolic profile assumed is:

$$u = u_x \left(\frac{2y}{\delta} - \frac{y^2}{\delta^2} \right) \tag{80}$$

which meets the boundary conditions of:

$$y = 0\, , \qquad u = 0$$

$$y = \delta\, , \qquad u = u_x\, , \qquad \frac{\partial u}{\partial y} = 0$$

$$\theta = T - T_w\, ; \qquad \theta = \theta_0 \left(\frac{2y}{\delta_T} - \frac{y^2}{\delta_T^2} \right) \tag{81}$$

30

which meets the boundary conditions of:

$$y = 0, \quad T = T_w, \quad \theta = 0$$

$$y = \delta_T \quad T = T_0, \quad \theta = \theta_0, \quad \frac{\partial \theta}{\partial y} = 0.$$

Substitution of the velocity profile into the momentum equation

$$\frac{\partial}{\partial x} \int_0^\delta \rho u^2 \, dy - u_x \frac{\partial}{\partial x} \int_0^\delta \rho u \, dy = -\delta \frac{\partial p}{\partial x} - \mu \left(\frac{\partial u}{\partial y} \right)_{y=0} \tag{64}$$

leads to

$$\frac{8}{15} \rho \frac{d}{dx} (u_x^2 \delta) - \frac{2}{3} \rho u_x \frac{d}{dx} (u_x \delta) + \delta \frac{\partial p}{\partial x} = - \frac{2 \mu u_x}{\delta} \tag{82}$$

which, upon further manipulation, becomes

$$\frac{d\delta^2}{dx} - \left[\frac{3}{u_x^2} \frac{d}{dx} \left(u_x^2 + \frac{5p}{\rho} \right) \right] \delta^2 = \frac{30 \nu}{u_x}. \tag{83}$$

Considering the bracketed term and the Bernoulli relation

$$p + \rho \frac{u_x^2}{2} = p_c \tag{84}$$

$$u_x^2 = \frac{2 p_c}{\rho} - \frac{2p}{\rho} \tag{85}$$

$$\frac{3}{u_x^2} \frac{d}{dx} \left(u_x^2 + \frac{5p}{\rho} \right) = \frac{3}{u_x^2} \frac{d}{dx} \left(\frac{2 p_c}{\rho} + \frac{3p}{\rho} \right) \tag{86}$$

Since p_c is a constant with respect to x

$$\frac{3}{u_x^2} \frac{d}{dx} \left(\frac{2 p_c}{\rho} + \frac{3p}{\rho} \right) = \frac{9}{2} \frac{1}{\left(\frac{\rho u_x^2}{2} \right)} \frac{dp}{dx}. \tag{87}$$

But

$$\frac{dp}{dx} = - \frac{d}{dx} \left(\frac{\rho u_x^2}{2} \right) \tag{88}$$

and

$$- \frac{9}{2} \frac{1}{\frac{\rho u_x^2}{2}} \frac{d \left(\frac{\rho u_x^2}{2} \right)}{dx} = - \frac{9}{2} \frac{d}{dx} \left(\ln \rho \frac{u_x^2}{2} \right) \tag{89}$$

31

The momentum equation becomes:

$$\frac{d\delta^2}{dx} + \frac{9}{2}\left[\frac{d}{dx}\left(\ln\frac{\rho u_x^2}{2}\right)\right]\delta^2 = \frac{30\nu}{u_x} . \tag{90}$$

The solution to this equation is

$$\delta^2 = e^{-\int \frac{d}{dx}\left(\ln\frac{\rho u_x^2}{2}\right)dx}\int e^{\int \frac{d}{dx}\left(\ln\frac{\rho u_x^2}{2}\right)dx} \cdot \frac{30\nu}{u_x}\,dx$$

$$+ c\,e^{-\int \frac{d}{dx}\left(\ln\frac{\rho u_x^2}{2}\right)dx} \tag{91}$$

$$\delta^2 = \frac{30\nu}{\left(\frac{\rho u_x^2}{2}\right)^{9/2}}\int \frac{\left(\frac{\rho u_x^2}{2}\right)^{9/2}}{u_x}\,dx + \frac{c}{\left(\frac{\rho u_x^2}{2}\right)^{9/2}} . \tag{92}$$

For the boundary layer thickness to remain finite at $x = 0$, $u_x = 0$, c must be zero.

$$\delta^2 = \frac{30\nu\sqrt{\frac{\rho}{2}}}{\left(\frac{\rho u_x^2}{2}\right)^{\frac{9}{2}}}\int_0^x \left(\frac{\rho u_x^2}{2}\right)^4\,dx . \tag{93}$$

From

$$\frac{\rho u_x^2}{2} \equiv \frac{\rho u^2}{2} = p_c\left[1-\left(\frac{1}{1+z^2}\right)^2\right] \tag{79}$$

where $u = u_x$, the velocity outside the boundary layer,

$$\delta^2 = 15\mu a\sqrt{\frac{2}{\rho p_c}}\quad \frac{1}{\gamma^{\frac{9}{2}}}\int_0^z \gamma^4\,dz \tag{94}$$

where

$$\gamma = \left[1-\left(\frac{1}{1+z^2}\right)^2\right]$$

$z = x/a$

a = spacing of corona wire from plate.

Using a somewhat tedious process, the integral for this parabolic case can be integrated exactly. γ^4 is expanded and integrated term by term to give:

32

$$F(z) \equiv \int_0^z \gamma^4 \, dz = z - 0.899023 \left(\frac{z}{1+z^2} + \tan^{-1} z \right)$$

$$+ 0.7333984 \; \frac{z}{(1+z^2)^2} + 0.5867188 \; \frac{z}{(1+z^2)^3}$$

$$- 0.3542411 \; \frac{z}{(1+z^2)^4} - 0.3148810 \; \frac{z}{(1+z^2)^5}$$

$$+ 0.0773810 \; \frac{z}{(1+z^2)^6} + 0.0714286 \; \frac{z}{(1+z^2)^7} . \tag{95}$$

Thus an explicit solution for the square of the thickness of the boundary layer is obtained. The behavior of the expression for δ^2 in the neighborhood of the origin must be investigated closely, because the expression $\gamma^{9/2}$ approaches zero at the origin. Applying L'Hopital's rule, let

$$\frac{f(z)}{g(z)} \equiv \frac{\int \gamma^4 dz}{\gamma^{\frac{9}{2}}} .$$

Then

$$\frac{f'(z)}{g'(z)} = \frac{\gamma^4}{\frac{9}{2} \gamma^{\frac{7}{2}} \frac{d\gamma}{dz}} = \frac{2}{9} \; \frac{\gamma^{\frac{1}{2}}}{\frac{d\gamma}{dz}}$$

$$= \frac{2}{9} \; \frac{\gamma^{\frac{1}{2}}}{4z(1+z^2)^{-3}} = \frac{1}{18} \; (2+z^2)^{\frac{1}{2}} \; (1+z^2)^2 \tag{96}$$

$$\lim_{z \to 0} \frac{f(z)}{g(z)} = \frac{\sqrt{2}}{18} . \tag{97}$$

At the origin then

$$\delta_0^2 = \frac{5}{3} \mu a \sqrt{\frac{1}{\rho p_c}} \tag{98}$$

$$\delta_0 = \left(\frac{5}{3} \mu a \right)^{\frac{1}{2}} \left(\frac{1}{\rho p_c} \right)^{\frac{1}{4}} . \tag{99}$$

For larger values of z

$$\delta^2 = 15 \mu a \sqrt{\frac{2}{\rho p_c}} \; \frac{\int_0^z \gamma^4 \, dz}{\gamma^{\frac{9}{2}}} . \tag{100}$$

The shape of the boundary layer is given by

$$\frac{\delta}{\left(15\mu a \sqrt{\frac{2}{\rho P_c}}\right)^{\frac{1}{2}}} = \left[\frac{\int_0^z \gamma^4 dz}{\gamma^{\frac{2}{2}}}\right]^{\frac{1}{2}} \tag{101}$$

This function is plotted in Figure 48. The function shows the finite value at the origin, and the subsequent increase as z gets larger.

The energy equation will be considered next.

$$J_m C_p \left[\frac{\partial}{\partial x}\int_0^{\delta_T}\rho u T dy - T_0 \frac{\partial}{\partial x}\int_0^{\delta_T}\rho u dy\right] - \int_0^{\delta_T} u \frac{\partial p}{\partial u} dy = - J_m k \left(\frac{\partial T}{\partial y}\right)_{y=0} \tag{65}$$

Substituting

$$\theta = T - T_w$$

$$\theta = \theta_0 \left(\frac{2y}{\delta_T} - \frac{y^2}{\delta_T^2}\right)$$

$$\frac{\partial \delta_T}{\partial x}\left[\int_0^1 (u\theta - u\theta_0)\, d\frac{y}{\delta_T}\right] - \frac{1}{\rho J_m C_p}\frac{\partial p}{\partial x}\delta_T \int u\, d\frac{y}{\delta_T} = -a\left(\frac{\partial\theta}{\partial y}\right)_{y=0} \tag{102}$$

$$-\theta_0 \frac{\delta*}{6}\left[1 - \frac{\delta*}{5}\right]\frac{d}{dx} u_x \delta_T - \frac{\delta* u_x}{\rho J_m C_p}\left[1 - \frac{\delta*}{3}\right] = -\frac{2a\theta_0}{\delta_T} \tag{103}$$

where $\delta* \equiv \dfrac{\delta_T}{\delta}$ and is assumed not to vary appreciably with x.

$$\frac{\partial \delta_T^2}{\partial x} + \left\{\frac{1}{u_x^2}\frac{\partial u_x^2}{\partial x} - 20\frac{\delta*-3}{\delta*-5}\cdot\frac{\frac{\partial p}{\partial x}}{\rho J_m C_p \theta_0}\right\}\delta_T^2 = -\frac{120 a}{\delta*(\delta*-5)u_x} \tag{104}$$

which solution is:

$$\delta_T^2 = e^{-\int f_1(x)\,dx}\int e^{\int f_1(x)\,dx} f_2(x)\,dx + c e^{-\int f_1(x)\,dx} \tag{105}$$

where

$$f_1(x)\,dx \equiv \left\{\frac{1}{u_x^2}\frac{du_x^2}{dx} - 20\frac{\delta*-3}{\delta*-5}\frac{\frac{\partial p}{\partial x}}{\rho J_m C_p \theta_0}\right\}$$

$$f_2(x)\,dx \equiv -\frac{120 a}{\delta*(\delta*-5)u_x}$$

34

Therefore:

$$e^{\int f_1(x)\,dx} = e^{\int \frac{d\ln u_x^2}{dx}\,dx} \times e^{-20\left(\frac{\delta_* - 3}{\delta_* - 5}\right)\frac{1}{\rho J_m C_p \theta_0}\int \frac{dp}{dx}\,dx}$$

$$= u_x^2\, e^{-\left(\frac{\delta_* - 3}{\delta_* - 5}\right)\frac{20p}{\rho J_m C_p \theta_0}} \tag{106}$$

$$\int e^{\int f_1(x)\,dx} f_2(x)\,dx = \int u_x^2 e^{-\left(\frac{\delta_* - 3}{\delta_* - 5}\right)\frac{20p}{\rho J_m C_p \theta_0}} (-1)\frac{120\,\alpha}{\delta_*(\delta_* - 5)u_x}\,dx$$

$$= \frac{-120\,\alpha}{\delta_*(\delta_* - 5)}\int u_x e^{-\left(\frac{\delta_* - 3}{\delta_x - 5}\right)\frac{20p}{\rho J_m C_p \theta_0}}\,dx \cdot \tag{107}$$

Substituting

$$p = p_c\left[\frac{1}{1+z^2}\right]^2 \tag{29}$$

$$\alpha_1 \equiv \left(\frac{\delta_* - 3}{\delta_* - 5}\right)\frac{20}{\rho J_m C_p \theta_0}$$

$$u_x^2 = \frac{2p_c}{\rho}\gamma$$

and noting that for the solution to remain finite at the origin, $c = 0$,

$$\delta_T^2 = \frac{-120\,\alpha\,\alpha\,e^{\alpha_1 p_c\left(\frac{1}{1+z^2}\right)^2}}{\delta_*(\delta_* - 5)\sqrt{\frac{2p_c}{\rho}}\,\gamma}\int_0^z \gamma^{\frac{1}{2}} e^{-\alpha_1 p_c\left(\frac{1}{1+z^2}\right)^2}\,dz \tag{108}$$

Using the first two terms of the series expansion for $e^{\wedge}$:

$$e^x = 1 + x + \frac{x^2}{2!} + \frac{x^3}{3!} + \cdots \tag{109}$$

leads to

$$e^{\alpha_1 p_c\left(\frac{1}{1+z^2}\right)^2} \cong 1 + \alpha_1 p_c\left(\frac{1}{1+z^2}\right)^2 \tag{110}$$

The expression for δ_T^2 becomes:

$$\delta_T^2 = -\frac{120\,\alpha\,\alpha}{\delta_*(\delta_* - 5)}\frac{\left[1 - \alpha_1 p_c\left(\frac{1}{1+z^2}\right)^2\right]}{\sqrt{\frac{2p_c}{\rho}}\,\gamma}\int_0^z \gamma^{\frac{1}{2}}\left[1 + \alpha_1 p_c\left(\frac{1}{1+z^2}\right)^2\right]\,dz \tag{111}$$

35

This is a complex expression for which no exact solution was found.

The expression $\alpha_i\, p_c$ will be examined further. At the centerline $p_c = \rho_2 U^2$, where U is the peak impinging velocity.

$$\alpha_1\, p_c = \frac{\delta_* - 3}{\delta_* - 5} \cdot \frac{20 p_c}{\rho\, J_m\, c_p\, \theta_0}$$

$$= \frac{\delta_* - 3}{\delta_* - 5} \cdot \frac{10 U^2}{J_m\, c_p\, \theta_0} = \frac{\delta_* - 3}{\delta_* - 5}\, 10\, N_{Ek} \tag{112}$$

where

$$N_{Ek} \equiv \frac{U^2}{J_m\, c_p\, \theta_0}$$

To determine the order of magnitude of $\alpha_1\, p_c$, consider typical values of the various terms.

Typically:

$$\theta_0 = 20°F$$

$$U = 10\ ft/sec$$

$$c_p = 0.24\ BTU / lb\ °F$$

$N_{Ek} = 8.32 \times 10^{-4}$

For values of δ_* from 0 to 3, the expression $\dfrac{\delta_* - 3}{\delta_* - 5}$ lies between 3/5 and 0. Assuming a value of 1/2 which occurs when $\delta_* = 1$,

$$\alpha_1\, p_c = 4.16 \times 10^{-3}.$$

Since the pressure relation

$$\frac{p}{p_c} = \left[\frac{1}{1 + z^2}\right]^2 \tag{29}$$

varies between 1 and 0 as z varies from 0 to infinity, $\alpha_1\, p_c \left(\dfrac{1}{1 + z^2}\right)^2$ will always be smaller than 4.16×10^{-3} for $\delta_* = 1$. Values of δ_* above 2 are unlikely. Evaluation of δ_T/δ at specific points verified this. If δ_* becomes greater than 3 the analysis would become questionable, certainly in the region $\delta_* = 5$. Therefore:

$$e^{\alpha_1\, p} < e^{4.16 \times 10^{-3}}$$

$$< \sim 1.004$$

for all values of z.

For the small pressures involved in a corona discharge, then,

$$e^{\alpha_1 p} \cong 1$$

$$\delta_T^2 = \frac{-120 \, \alpha a}{\gamma \cdot \delta_*(\delta_* - 5)\sqrt{\frac{2 p_c}{\rho}}} \int \gamma^{\frac{1}{2}} \, dz . \tag{113}$$

The value of $\overline{\delta_T^2}$ as $z \to 0$ is indeterminate. Applying L'Hopital's rule

$$\frac{f(z)}{g(z)} = \frac{\int \gamma^{\frac{1}{2}} dz}{\gamma} .$$

$$\frac{f'(z)}{y'(z)} = \frac{\gamma^{\frac{1}{2}}}{\frac{d\gamma}{dz}} = \frac{\gamma^{\frac{1}{2}}}{4z(1+z^2)^{-3}} = \frac{(2+z)^{\frac{1}{2}}(1+z^2)}{4} \tag{114}$$

$$\mathscr{l}\!\underset{z \to 0}{\mathrm{im}} \frac{f(z)}{g(z)} = \frac{\sqrt{2}}{4} . \tag{115}$$

At the origin

$$\delta_T^2 = \frac{-30 \, \alpha a}{\delta_*(\delta_* - 5)}\sqrt{\frac{\rho}{p_c}} \tag{116}$$

By definition $\delta_* = \delta_T/\delta$. The value of δ_* at the origin can be determined as follows using the values of δ_T^2 and δ^2 at the origin.

$$\delta_{*_0}^2 = \frac{\delta_T^2}{\delta^2} = \frac{-30\alpha a \frac{\sqrt{\frac{\rho}{p_c}}}{\delta_*(\delta_* - 5)}}{\left(\frac{5}{3}\right) a\mu \sqrt{\frac{1}{\rho \, p_c}}}$$

$$= - \frac{18 \, N_{Pr}^{-1}}{\delta_*(\delta_* - 5)} . \tag{117}$$

For air, with $N_{Pr} = 0.71$, a graphical solution yields $\delta_* = 2.048$.

For values of $z > 0$, the ratio δ_T^2/δ^2 varies in a more complex fashion. For small pressures, this ratio becomes:

$$\delta_*^2 = \frac{\delta_T^2}{\delta^2} = \frac{-4 \, N_{Pr}^{-1}}{\delta_*(\delta_* - 5)}\left\{\frac{\frac{\int \gamma^{\frac{1}{2}} dz}{\gamma}}{\frac{\int \gamma^4 dz}{\gamma^{\frac{9}{2}}}}\right\} . \tag{118}$$

37

As z approaches infinity, the bracketed term approaches $\int dz / \int dz$ and the ratio approaches 1.

At very high z,

$$\delta_*^2 = \frac{-4 \, N_{Pr}^{-1}}{\delta_* (\delta_* - 5)} \,. \tag{119}$$

For a Prandtl number of unity, $\delta_* = 1$. For air, $\delta_* = 1.05$. Thus a variation in δ_* does occur with a change in z. This is contrary, of course, to the assumption originally made in solving the integral equations. The effect of the change in δ_* will be considered in evaluating the over-all results.

The heat transfer coefficients can be calculated from

$$h_x = -\frac{k}{\theta_0} \frac{\partial T}{\partial y} \bigg|_{y=0} \tag{120}$$

Using $\theta = T - T_w$ and $\theta = \theta_0 \left(\frac{2y}{\delta_T} - \frac{y^2}{\delta_T^2} \right)$,

$$h_x = \frac{2k}{\delta_T} \tag{121}$$

Expressing this in terms of the velocity boundary layer,

$$h_x = \frac{2k}{\delta_*} \frac{(2 \rho \, p_c)^{\frac{1}{4}}}{(30 a \mu)^{\frac{1}{2}}} \frac{1}{\left[\frac{F(z)}{\gamma^{\frac{9}{2}}} \right]^{\frac{1}{2}}} \,. \tag{122}$$

Using the pressure-current relationship found in the previous section,

$$p_c = c_1 \, i$$

$$h_x = \frac{2k}{\delta_*} \frac{(2 \rho \, c_1 \, i)^{\frac{1}{4}}}{(30 a \mu)^{1/2}} \frac{1}{\left[\frac{F(z)}{\gamma^{9/2}} \right]^{1/2}} \,. \tag{123}$$

Near the origin $\delta_* = 2.048$

At the origin

$$h_x = \frac{2k}{2.048} \left(\frac{3}{5} \right)^{\frac{1}{2}} \frac{(\rho c_1 \, i)^{1/4}}{(a \mu)^{1/2}} \tag{124}$$

where c_1 is an experimental and geometric constant. This equation predicts that the heat transfer coefficient at any station should vary as the one-fourth power of the current.

The shapes of the velocity and temperature profiles which are assumed may materially affect the magnitudes of the boundary layer thickness and heat transfer coefficient but should have relatively small influence on the form of the variation in heat transfer

coefficient with distance. In order to get an estimate of the changes caused by profile shape, two other profiles were assumed, linear and cubic.

Linear Solution

For the linear solution the following curves were assumed:

$$u = u_x \frac{y}{\delta}$$

$$\theta = \theta_0 \frac{y}{\delta_T} \quad ; \quad \theta \equiv T - T_w$$

with the boundary conditions of

$$y = 0, \quad T = T_w, \quad \theta = 0, \quad u = 0$$

$$y = \delta, \quad u = u_x$$

$$y = \delta_T, \quad T = T_0, \quad \theta = \theta_0$$

Substituting these into the integral equations, one obtains for the velocity boundary thickness,

$$\delta^2 = 6 \, 0 \mu \sqrt{\frac{2}{\rho P_c}} \quad \frac{\int_0^z \gamma^{9/2} \, dz}{\gamma^5} \tag{125}$$

For z = 0

$$\frac{\int \gamma^{9/2} \, dz}{\gamma^5} = \frac{\sqrt{2}}{20} \tag{126}$$

$$\delta_0^2 = \frac{3}{5} \, a \mu \sqrt{\frac{1}{\rho \cdot P_c}} \tag{127}$$

$$\delta_0 = \left(\frac{3}{5} \, a \mu\right)^{1/2} \left(\frac{1}{\rho P_c}\right)^{1/4} \tag{128}$$

The thermal boundary layer is given by

$$\delta_T^2 = \frac{12 \, \alpha a \left[1 - 3 N_{Ek} \left(\frac{1}{1+z^2}\right)^2\right]}{\delta_* \sqrt{\frac{2 P_c}{\rho}}} \int_0^z \gamma^{1/2} \left[1 + 3 N_{Ek} \left(\frac{1}{1+z^2}\right)^2\right] dz \tag{129}$$

$$\approx \frac{12 \, \alpha 0}{\delta_* \sqrt{\frac{2 P_c}{\rho}} \, \gamma} \int_0^z \gamma^{1/2} \, dz \tag{130}$$

39

For $z = 0$

$$\delta_T^2 = \frac{3 \sigma \alpha}{\delta_*} \sqrt{\frac{\rho}{p_c}} \tag{131}$$

At the origin

$$\delta_*^2 = \frac{\delta_T^2}{\delta^2} = \frac{5 N_{Pr}^{-1}}{\delta_*} \tag{132}$$

$$\delta_*^3 = 5 N_{Pr}^{-1} \tag{133}$$

$$\delta_* = 1.71 N_{Pr}^{-1} \tag{134}$$

For air $\delta_* = 1.92$.

For larger values of z

$$\frac{\delta_T^2}{\delta^2} = \frac{12 \alpha \sigma \sqrt{\rho p_c} \dfrac{\int_0^z \gamma^{1/2} dz}{\gamma}}{\delta_* \sqrt{\dfrac{2 p_c}{\rho}} \quad 6 \sigma \mu \sqrt{2} \quad \dfrac{\int_0^z \gamma^{1/2} dz}{\gamma^5}} \tag{135}$$

For $z \to \infty$

$$\frac{\delta_T^2}{\delta^2} = \frac{N_{Pr}^{-1}}{\delta_*}$$

$$\delta_*^3 = N_{Pr}^{-1} \tag{136}$$

$$\delta_* = N_{Pr}^{-\frac{1}{3}} \tag{137}$$

The heat transfer coefficient is given by

$$h_x = -\frac{k}{\theta_0} \left(\frac{\partial T}{\partial y}\right)_{y=0} \quad ; \quad h_x = \frac{k}{\delta \cdot \delta_*}$$

$$h_x = \frac{k (2 \rho p_c)^{1/4}}{\delta_* (12 \sigma \mu)^{1/2} \left[\dfrac{\int_0^z \gamma^{9/2} dz}{\gamma^5}\right]^{1/2}} \tag{138}$$

$$h_x = \frac{k (2 \rho c_i i)^{1/4}}{\delta_* (12 \sigma \mu)^{1/2} \left[\dfrac{\int_0^z \gamma^{9/2} dz}{\gamma^5}\right]^{1/2}} \tag{139}$$

The values for $\left(\dfrac{\int \gamma^{9/2}\,dz}{\gamma^5}\right)$ are given by the following approximation:

$z \geq 1$

$$\frac{\displaystyle\int_0^z \gamma^{9/2}\,dz}{\gamma^5} = \frac{1}{\gamma^5}\left\{ z - .936973\left[\frac{1}{(1+z^2)} + \tan^{-1} z\right]\right.$$

$$+ \ 0.844934\ \frac{z}{(1+z^2)^2} + 0.700281\ \frac{z}{(1+z^2)^3} - 0.542473\ \frac{z}{(1+z^2)^4}$$

$$- \ 0.482326\ \frac{z}{(1+z^2)^5} + 0.197886\ \frac{z}{(1+z^2)^6} + 0.182664\ \frac{z}{(1+z^2)^7}$$

$$\left. - \ 0.029514\ \frac{z}{(1+z^2)^8} - 0.027777\ \frac{z}{(1+z^2)^9} + \ - - - \right\} \qquad (140)$$

Values between $z = 0$ and $z = 1$ can be obtained from the curve in Figure 49. The curve in this region was obtained by graphical integration. At the origin where

$$\frac{\int \gamma^{9/2}\,dz}{\gamma^5} = \frac{\sqrt{2}}{20}$$

$$h_x = \left(\frac{5}{3}\right)^{1/2}\ \frac{k}{1.92}\ \frac{(\rho\, c_1\, l)^{1/4}}{(a\,\mu)^{1/2}} \qquad (141)$$

Cubic Solution

For the cubic solution the following curves were assumed:

$$u = u_x\left[\frac{3}{2}\left(\frac{y}{\delta}\right) - \frac{1}{2}\left(\frac{y}{\delta}\right)^3\right] \qquad (142)$$

$$\theta = \theta\left[\frac{3}{2}\left(\frac{y}{\delta_T}\right) - \frac{1}{2}\left(\frac{y}{\delta_T}\right)^3\right] \qquad (143)$$

with $\theta = T - T_w$ as before. These equations meet the boundary conditions of:

$$y = 0\ ,\quad u = 0\ ,\quad \frac{d^2 u}{dy^2} = 0,\quad \theta = 0\ ,\quad \frac{d^2\theta}{dy^2} = 0$$

$$y = \delta\ ,\quad u = u_x\ ,\quad \frac{du}{dy} = 0$$

$$y = \delta_T\ ,\quad \theta = \theta_0\ ,\quad \frac{d\theta}{dy} = 0$$

Substituting these into the integral equations, one obtains for the velocity boundary layer thickness

$$\delta^2 = \frac{140}{13} \, a\mu \left(\frac{2}{\rho p_c}\right)^{1/2} \frac{\int_0^z \gamma^{109/26} \, dz}{\gamma^{61/13}} \tag{144}$$

$$z \to 0 \qquad \frac{\int \gamma^{109/26} \, dz}{\gamma^{61/13}} = \frac{13}{244} \sqrt{2} \tag{145}$$

Therefore:

$$\delta_0^2 = \frac{72}{61} \, a\mu \left(\frac{1}{\rho p_c}\right)^{1/2} \tag{146}$$

$$\delta_0 = \left(\frac{72}{61}\right)^{1/2} \left(a\mu\right)^{1/2} \left(\frac{1}{\rho p_c}\right)^{1/4} \tag{147}$$

The thermal boundary layer is given by

$$\delta_T^2 = \left\{ \frac{540 \, a\alpha \left[1 - \frac{45}{2} N_{Ek} \left(\frac{6\delta_* - \delta_*^3}{27\delta_* - 2\delta_*^3}\right) \left(\frac{1}{1+z^2}\right)^2\right]}{(27\delta_* - 2\delta_*^3) \left(\frac{2 p_c}{\rho}\right)^{1/2} \gamma} \right\}$$

$$\times \left\{ \int_0^z \left[1 + \frac{45}{2} N_{Ek} \left(\frac{6\delta_* - \delta_*^3}{27\delta_* - 2\delta_*^3}\right) \left(\frac{1}{1+z^2}\right)^2 \right] dz \right\} \tag{148}$$

$$\delta_T^2 \cong \frac{540 \, a\alpha}{(27\delta_* - 2\delta_*^3) \left(\frac{2 p_c}{\rho}\right)^{1/2}} \int_0^z \gamma^{1/2} \, dz \tag{149}$$

For $z = 0$,

$$\delta_T^2 = \frac{135 \, a\alpha}{(27\delta_* - 2\delta_*^3)} \left(\frac{\rho}{p_c}\right)^{1/2} \tag{150}$$

The ratio of the boundary layer thicknesses at the origin is given by

$$\frac{\delta_T^2}{\delta^2} = \frac{135 \, a\alpha \left(\frac{\rho}{p_c}\right)^{1/2}}{27\delta_* - 2\delta_*^3} \times \left(\frac{61}{72}\right) \frac{(\rho p_c)^{1/2}}{a\mu}$$

$$= \frac{135}{27\delta_* - 2\delta_*^3} \, \frac{61}{72} \, N_{Pr}^{-1} \tag{151}$$

$$16\delta_*^5 - 216\delta_*^3 = -915 \, N_{Pr}^{-1} \tag{152}$$

For air, a graphical solution yields 2.088 for $z = 0$. As $z \to \infty$, for a Prandtl number of one, $\delta*$ approaches 1.0. The equation is

$$27 \delta_*^3 - 2 \delta_*^5 = 25.1 \, N_{P_r}^{-1} \tag{153}$$

The heat transfer coefficient is given by

$$h_x = - \frac{k}{\theta_0} \left(\frac{\partial T}{\partial y} \right)_{y=0} \quad ; \quad h_x = \frac{3}{2} \frac{k}{\delta \cdot \delta_*}$$

$$h_x = \frac{3}{2} \frac{k}{\delta_*} \frac{\left(\frac{13}{280 \, a\mu} \right)^{1/2} (2 \rho \, \rho_c)^{1/4}}{\left[\frac{\int_0^z \gamma^{109/26} \, dz}{\gamma^{61/13}} \right]^{1/2}} \tag{154}$$

$$h_x = \frac{3}{2} \frac{k}{\delta_*} \frac{\left(\frac{13}{280 \, a\mu} \right)^{1/2} (2 \rho \, c_i \, i)^{1/4}}{\left[\frac{\int_0^z \gamma^{109/26} \, dz}{\gamma^{61/13}} \right]^{1/2}} \tag{155}$$

The function $\left[\dfrac{\int \gamma^{109/26} dz}{\gamma^{61/13}} \right]$ is shown in Figure 49. The values in the region $z = 0$ to

$z = 1$, are obtained by graphical integration. For values of z greater than one, the following expression can be used.

$$\frac{\int_0^z \gamma^{109/26} \, dz}{\gamma^{61/13}} = \frac{1}{\gamma^{61/13}} \left\{ z - 0.914161 \left(\frac{z}{1+z^2} + \tan^{-1} z \right) \right.$$

$$+ 0.776297 \frac{z}{(1+z^2)^2} + 0.630396 \frac{z}{(1+z^2)^3} - 0.426638 \frac{z}{(1+z^2)^4}$$

$$- 0.379283 \frac{z}{(1+z^2)^5} + 0.123729 \frac{z}{(1+z^2)^6} + 0.114211 \frac{z}{(1+z^2)^7}$$

$$\left. - 0.011352 \frac{z}{(1+z^2)^8} - 0.010684 \frac{z}{(1+z^2)^9} + - - - \right\} \tag{156}$$

At the origin

$$h_x = \frac{3}{2} \frac{k}{2.088} \left(\frac{61}{72} \right)^{1/2} \frac{(\rho \, c_i \, i)^{1/4}}{(a\mu)^{1/2}} \tag{157}$$

Combined Thermal Body Force and Corona Wind

The case of the vertical plate subjected to the combined electric field and thermal body forces was considered from the integral equation approach also. The area where the corona wind velocity is approximately constant was considered in detail. The

pressure gradient term $\frac{p}{p_c} = \left[\frac{1}{1+z^2} \right]^2$ was not included in the initial analysis. It

was decided that the form of the equations should be investigated first in the region where the pressure was approximately constant. Based on the outcome of this initial analysis, the pressure term could be reconsidered.

It was assumed that the velocity and thermal boundary layer thicknesses were the same. The following velocity and temperature profiles were assumed.

$$u = u_0 \left[\frac{3}{2} \frac{y}{\delta} - \frac{1}{2} \left(\frac{y}{\delta} \right)^3 \right] + u_x \left(\frac{y}{\delta} \right) \left[1 - \frac{y}{\delta} \right]^2 \tag{158}$$

$$\frac{T - T_0}{T_w - T_0} = \left[1 - \frac{y}{\delta} \right]^2 \tag{159}$$

where

u_0 = velocity due to the corona wind

u_x = velocity due to the free convection.

These profiles were substituted into integral equations. The resulting equations obtained are:

Momentum:

$$\frac{1}{105} \frac{d\delta \left(51.625 \, u_0^2 + 9.5 \, u_0 \, u_x + u_x^2 \right)}{dx} - \frac{u_0}{24} \frac{d\delta \left(15 \, u_0 + 2 \, u_x \right)}{dx}$$

$$= \frac{g \, \delta}{3} \left(\frac{T_w - T_0}{T_0} \right) - \frac{\nu}{\delta} \left(\frac{3}{2} \, u_0 + u_x \right) \tag{160}$$

Energy:

$$\delta \frac{d}{dx} \left[\delta \left(3 \, u_0 + u_x \right) \right] = 60 \, \alpha \tag{161}$$

An intricate coupling exists and no simple analytic solution was found for this set of equations. It would be possible to determine a solution for specific cases through numerical methods, but because of the limitations of time no further work was expended on this approach. Because of the difficulty experienced even with a constant pressure distribution,

the variation of pressure $\frac{p}{p_c} = \left[\frac{1}{1+z^2} \right]^2$ was not introduced into the analysis.

Summary of Analysis

The analysis of the horizontal plate based upon the Von Karman integral approach appears to have been fruitful. The magnitude of the heat transfer coefficient is predicted to vary as

44

$i^{\frac{1}{4}}$ and explicit relationships are available for the variation of h_x. Because of the need for assuming velocity and temperature profiles in the integral method, it cannot be expected that the absolute magnitude of the heat transfer coefficient will be precise. The trends, however, should be representative of the actual variations of h_x if the physical model used is a reasonable approximation to the actual test model. The validity of the assumption of very low space charge distortion of the field equations can only be ascertained after comparison with the test data.

The analysis of the horizontal plate by means of the thin-jet approach appears to provide an approximate technique for estimating the effects of the corona discharge on heat transfer. The difficulty of estimating the proper jet width, however, limits the utility of this method.

In the next section a comparison will be made between the analytical predictions and the actual test data for the horizontal plate case.

<div align="center">

CORRELATION OF TEST DATA WITH THE
ANALYTICAL SOLUTION

</div>

This section will be devoted to the comparison of the analytical solutions and the test data obtained from the interferometer. The comparison is limited to the case of the horizontal plate with the bottom side of the plate heated. The configuration considered is the 0.004-inch wire located 2 cm and 5 cm below the plate. Both the integral-equation solutions and the two-dimensional thin-jet solution will be compared.

In order to compare the theory with the test data, the constants are evaluated at the mean temperature of the air in front of the plate. The values of the thermal conductivity, density, and viscosity of air at various temperatures were taken from Jakob and Hawkins (Ref. 17).

The constant in the equation for pressure $p_c = c_1 i$ is obtained from Figure 27, in which the data for the 0.004-inch wire is plotted for various wire spacings.

For

$$a = 2 \text{ cm}$$

$$c_1 = 3.54 \times 10^{-4} \; \frac{\text{p. s. f.}}{\mu a}$$

For

$$a = 5 \text{ cm}$$

$$c_1 = 3.80 \times 10^{-4} \; \frac{\text{p. s. f.}}{\mu a}$$

These values of c_1 are derived from the test data on the pressure plate with the wire located vertically and the vertical dimension of the plate is 7 inches. However, the corresponding dimension of the heated plate is 10 inches. The current flowing to the plate for any given pressure will be proportional to the length of the wire and the plate. A test run was made to verify this. The pressure plate was masked off with electrical insulating tape in a series of steps and pressure-current measurements were taken.

The test results shown in Figure 50 indicate that the linear relation holds. Correcting c_1 for the difference in plate size:

$$a = 2 \text{ cm}$$

$$c_1 = 2.48 \times 10^{-4} \frac{\text{p.s.f.}}{\mu a}$$

$$a = 5 \text{ cm}$$

$$c_1 = 2.66 \times 10^{-4} \frac{\text{p.s.f.}}{\mu a}$$

For a typical case @ $T_{mean} = 79° F$,

$$\nu = 1.686 \times 10^{-4} \text{ sq. ft /sec}$$

$$k = 0.0151 \text{ BTU / hr - ft - °F}$$

$$\rho = 0.0736 \text{ lbs / cu ft}$$

INTEGRAL EQUATION SOLUTION

The above values are now substituted into the equations for heat transfer coefficient, as follows:

1. Equation (139) for the linear profile, assuming $\delta*$ variation to be small, becomes:

For a = 2 cm

$$h_x = 0.466 \, i^{1/4} \left(\frac{\int_0^z \gamma^{9/2} \, dz}{\gamma^5} \right)^{-\frac{1}{2}} \tag{162}$$

For a = 5 cm

$$h_x = 0.300 \, i^{1/4} \left(\frac{\int_0^z \gamma^{9/2} \, dz}{\gamma^5} \right)^{-\frac{1}{2}} \tag{163}$$

2. Equation (123) for the parabolic profile, assuming $\delta*$ variation to be small, becomes:

For a = 2 cm

$$h_x = 0.553 \, i^{1/4} \left(\frac{\int_0^z \gamma^4 \, dz}{\gamma^{9/2}} \right)^{-\frac{1}{2}} \tag{164}$$

For a = 5 cm

$$h_x = 0.356 \, i^{1/4} \left(\frac{\int_0^z \gamma^4 \, dz}{\gamma^{9/2}} \right)^{-\frac{1}{2}} \tag{165}$$

46

3. Equation (155) for the cubic profile, assuming $\delta*$ variation to be small, becomes:

For a = 2 cm

$$h_x = 0.479 \, i^{\frac{1}{4}} \left(\frac{\int_0^z \gamma^{109/26} \, dz}{\gamma^{61/13}} \right)^{-\frac{1}{2}} \quad (166)$$

For a = 5 cm

$$h_x = 0.309 \, i^{1/4} \left(\frac{\int_0^z \gamma^{109/26} \, dz}{\gamma^{61/13}} \right)^{-\frac{1}{2}} \quad (167)$$

TEST DATA CORRELATION

Typical solutions of heat transfer coefficient for the a = 2 cm case are shown in Figures 51, 52, and 53. The test data for the corresponding cases are shown in Figures 54 and 55.

From a comparison of the test data and the theoretical solutions at a = 2 cm, it can be seen that the trends of the solutions are good. The magnitude of h_x differs depending upon the profile considered. This had been anticipated, as was discussed in the previous section. To afford a more direct comparison, the theory and test data are shown together in Figure 56, which indicates that the trends are good. At the end of the plate the data and theory diverge. A large portion of this difference is believed to be due to the end effects of the plate. The comparison for a = 5 cm is shown in Figure 57. Both Figures 56 and 57 show that the theory predicts a somewhat more rapid decrease of h_x as x increases than is shown by the test data.

Since it appeared that the use of the fixed value of $\delta*$ might introduce sizeable variations in h_x as z became large, a study was undertaken to determine the explicit variation of $\delta*$ for all three velocity distributions. The variation of $\delta*$ with x is given by

For the parabolic case:

$$\delta_*^2 = \frac{4 \, N_{Pr}^{-1}}{\delta* \, (5 - \delta*)} \left\{ \frac{\int_0^z \gamma^{\frac{1}{2}} \frac{dz}{\gamma}}{\frac{\int_0^z \gamma^4 \, dz}{\gamma^{9/2}}} \right\} \quad (168)$$

For the linear case:

$$\delta_*^2 = \frac{N_{Pr}^{-1}}{\delta*} \left\{ \frac{\int_0^z \gamma^{\frac{1}{2}} \frac{dz}{\gamma}}{\frac{\int_0^z \gamma^{9/2} \, dz}{\gamma^5}} \right\} \quad (169)$$

For the cubic case:

$$\delta_*^2 = \frac{25.05}{27\delta* - 2\delta*^3} \, N_{Pr}^{-1} \left\{ \frac{\frac{\int_0^z \gamma^{1/2} \, dz}{\gamma}}{\frac{\int_0^z \gamma^{109/26} \, dz}{\gamma^{61/13}}} \right\} \quad (170)$$

47

The values of the integrals were determined by graphical integration of the numerator. For specific values of z, the values of $\delta*$ could be determined. The linear case provided an explicit solution

$$\delta* = N_{Pr}^{-\frac{1}{3}} \left\{ \frac{\dfrac{\int \gamma^{\frac{1}{2}} dz}{\gamma}}{\dfrac{\int \gamma^{\frac{3}{2}} dz}{\gamma^{\delta}}} \right\}^{\frac{1}{3}} \tag{171}$$

which exhibits the familiar N_{Pr}-1/3 form found in the forced-convection theory. The values of $\delta*$ for the parabolic and cubic cases were obtained by a careful graphical solution of the 4th order and 5th order equations. The variation of $\delta*$ is shown in Figure 58.

The heat transfer coefficients modified by the inclusion of the variation of $\delta*$ are shown in Figures 59, 60, 61, 62, 63, and 64. The test data for a = 5 cm is shown in Figure 65. A better comparison of the modified theory and the test data can be found in Figure 66 where the a = 2 cm curves and test data are compared at two values of the current. The agreement in shape of the theoretical curves is now considered to be excellent. The end effects of the plate are clearly evident in the test data. Since the changes made in $\delta*$ had no effect at the origin, the small deviation between test and theory remain. This difference is reflected in the relatively uniform displacement of the theoretical curve from the test data. Since one of the most sensitive parameters to determine the entire investigation was the absolute magnitude of pressure, it is not altogether unexpected that differences in magnitude exist. Figure 67 presents the comparison for a = 5 cm. Similar results to those presented for the 2 cm case are evident. The shape of the curves is in good agreement except where the end effects of the plate are evident. The absolute magnitudes of the heat transfer coefficients also differ somewhat from the test data.

The wide variation of heat transfer coefficient with corona wind over the plate implies a sizeable variation of the temperature profile in the boundary layer. This variation is presented for a typical case in Figure 68. The temperature profiles are plotted at several locations along the plate. The profiles do vary, and the slopes of the curves increase greatly near the origin under the impinging jet of air.

The theory predicted that the heat transfer coefficient should vary as $i^{\frac{1}{4}}$ under the action of the corona wind. To verify that such a trend exists, the values of h_x were plotted against $i^{\frac{1}{4}}$. The results are shown in Figures 69 and 70. The current varies from 0.32 μa to 180 μa for the 2 cm case, and from 2.6 μa to 180 μa for the 5 cm case. Data are plotted for several locations along the horizontal plate. The data at x = 0 for the a = 2 cm case were very erratic at high currents and are not included. It can be seen that straight lines passed through the points correlate with the data quite well. Consequently the prediction that the heat transfer coefficient should vary as $i^{\frac{1}{4}}$ is substantiated. Figure 71 presents data on the variation of the mean heat transfer coefficient with current. The ratio of the average heat transfer coefficient over the surface of the plate with applied field to the average free convection heat transfer coefficient is plotted against $i^{\frac{1}{4}}$. It can be seen that a linear relationship also would hold well for this case.

It is apparent from a review of the theory and the experimental work, that large changes in heat transfer over the free-convection case can be achieved through the use of the corona wind. Substantial increases occur for very small currents. The power required for the action is low; some typical values are shown in Table 1. These values are for some of the curves shown in Figures 54, 55, and 65.

48

Table 1

Power Requirements for Corona Wind, Horizontal Plate, 0.004-Inch Wire at Two Spacings.

Wire Spacing (cm.)	Current	Voltage (KV)	Power (watts)
2	0	0	0
2	.32	5.00	.0016
2	1.05	5.00	.0053
2	2.54	5.17	.0131
2	4.55	5.67	.0258
2	0	0	0
2	5.6	6.0	.0336
2	10.2	6.34	.0648
2	19.1	6.67	.127
2	41.0	8.00	.328
2	79.5	8.83	.703
5	0	0	0
5	2.6	8.33	.022
5	4.55	8.67	.039
5	10.2	10.00	.102
5	21.2	11.85	.251
5	39.5	14.19	.561
5	78.5	18.18	1.429

These data correspond to the data in Figures 54, 55, and 65.

THIN JET SOLUTION

The last correlation to be made is between the thin jet and the test data. The equations used were:

Stagnation region (Ref. 10):

$$x < \frac{4u}{\pi U} b$$

$$h_x = 0.570 \ N_{Pr}^{0.4} \ k \left(\frac{\pi}{4} \ \frac{U}{b} \cdot \frac{1}{\nu} \right)^{\frac{1}{2}} \tag{172}$$

Blasius region (Ref. 17):

$$h_x = k \left(\frac{u}{\nu x}\right)^{\frac{1}{2}} (0.332 \, N_{Pr}^{\frac{1}{3}}) \tag{173}$$

Study of the pressure distribution revealed that an approximate equivalent jet half-width for a = 2 cm would be b = a/2. Using this value and substituting:

$$U = \left(\frac{2 \, p_c}{\rho}\right)^{\frac{1}{2}}$$

$$p_c = c_1 \, i = 2.478 \times 10^{-4} \, i \tag{174}$$

The equation for the stagnation region becomes:

$$h_x = \left(\frac{\pi}{4}\right)^{\frac{1}{2}} (0.570 \, N_{Pr}^{0.4}) \, k \left(\frac{2 \rho}{a \mu}\right)^{\frac{1}{2}} \left(\frac{2 \times 2.4781}{\rho}\right)^{\frac{1}{4}} \tag{175}$$

Typically for air at 79°F and a = 2 cm:

$$h_x = 1.98 \, i^{\frac{1}{4}} \tag{176}$$

This expression holds from x = 0, to x = $2a/_\pi$. Beyond x = $2a/_\pi$ the Blasius solution is used. Fitting the Blasius solution so that at x = $2a/_\pi$ the heat transfer coefficients of the two regions are the same, results in the following expression when $\chi > 2a/\pi$:

$$h_x = \frac{2.23 \, i^{\frac{1}{4}}}{x^{\frac{1}{2}}} \tag{177}$$

where x is given in centimeters.

These relationships are plotted in Figure 72 for a = 2 cm. Comparison of this curve with the test data of Figure 55 indicates a fair degree of correlation. The right order of magnitude is achieved and the shapes of the curves approximate those for the test data except, of course, in the region of the ends of the plate. The primary problem in this method lies in the choice of a suitable jet half-width, b. No accurate nor logical method presents itself by which to determine b. Since both magnitude and, to some extent, shape are affected by the choice of b, this method can be considered only an approximation.

<div align="center">

EXPLORATORY TESTS ON FREE CONVECTION
WITH OTHER ELECTRODES

</div>

In the over-all investigation of the electrostatic effects on free-convection heat transfer, many electrode configurations were used. At the outset of the testing, a Model "T" Ford automotive spark coil was used as a high-voltage source. The voltage wave form was found to be very erratic, including both a D.C. component and random A.C. components. The spark coil was useful in providing some interesting pictures of effects of the corona discharge on the interferometer patterns. Results of tests made with a two-dimensional row of pins and the spark coil are shown in Figure 73. View A illustrates

the effect on the isothermal lines an instant after the field is applied; a large swirl can be seen moving upward at the top of the picture. View B shows the effect of the corona discharge under continuous application of the field. In both pictures the row of needles is represented by the gray line pointing upward towards the center of the plate. The dual lines on the left side of the picture are the support rods for the needles.

Figure 74 shows the results of an initial test in which a grid of 0.010-inch-diameter wires was placed in front of the heated plate. (The wire grid is shown in the rear of Figure 7.) The electric field is impressed between the fine wires and the heated plate. When voltage is applied by means of the automotive spark coil, the thermal boundary layer in the vicinity of the wires is pulled out decidedly. These pictures were taken in the initial exploratory phase of the work. The photography is very poor, but the pictures are included because the phenomenon they show had an important impact on subsequent testing. Many of the subsequent vertical plate tests with a single wire described in a previous section were aimed at understanding this pullout. The pullout phenomenon appears to indicate an action counter to that of corona wind, and even counter to the action which would be produced by dielectric streaming. As indicated in Reference 1, dielectric streaming would occur as the result of a body force produced by the nonuniform electric field. However, the density gradient and thus the dipole moment per unit volume, is in the direction to cause the dielectric streaming to move away from the fine wires. As discussed under testing, it is believed that the pullout occurs as an interaction between fluid streams, and one of these streams, the boundary flow, is highly viscous. Thus, it appears that the first impression of the picture may be misleading.

Figure 75 illustrates the results of tests with the same wire grid but using the high voltage provided by the D.C. power supply. At the very low currents, between 1 μa and 5 μa, the same pullout phenomenon occurred as was observed with the spark coil; pictures in the low current range are not included. View A is a reference with no field applied. The remaining pictures indicate the effect of increased currents on the isothermal lines. The thermal boundary layer is made thinner by the application of the electric field, and the entire flow field becomes erratic and apparently very turbulent.

Test results using a specially prepared surface for the heated plate are shown in Figure 76. This surface consisted of a series of 0.004-inch wires attached to the surface of an insulating sheet of plastic. The wires were spaced one inch apart, parallel to each other and horizontal to the plastic sheet, which was cemented to the front of the heated plate. The fine wires were located away from the plate surface facing the free room air. Dropping resistors were placed between each of the wires, and were so chosen that approximately a current of 10 μa per wire would flow for an applied voltage of 30 KV. It was believed that this configuration would provide for local sources of ions within the boundary layer. By placing the other electrode at various locations and applying a voltage, the possible effects on the boundary layers could be observed with the interferometer. View A illustrates the reference case with no applied field. The wires are so small, they cannot be seen at the surface of the plate. The external electrode is positioned 1-5/8 inches below the bottom edge of the plate. This electrode, the oval rod shown in the front of Figure 7, is not visible in the interferometer pictures. View B shows the effects when the field is applied. Even at high currents very little effect of the field is found. It is apparent that any attempt to control fluid behavior at the surface of a body through the application of electric fields will have to be done with a great deal of careful forethought.

Figure 77 illustrates the effect of a uniform electric field on the thermal boundary layer of the vertical heated plate. A flat 6-inch-by-10-inch aluminum electrode, unheated, was placed 1.1 cm in front of the heated plate. Views A and B show results before and after a

51

strong field was applied. No corona discharge occurred, no measurable currents were observed, and no changes to the fringe patterns are apparent. Tests of this type were repeated using several electrode spacings and applied voltages up to and including that necessary for breakdown (sparking). No effects on the isothermal lines were visible for applied fields below breakdown potentials. It thus appears that application of a uniform field in air with very low ionization produces no measurable changes on the free-convection heat transfer.

EXPLORATORY TESTS WITH DIELECTROPHORESIS

This section will cover very briefly a series of tests made to explore the body forces obtainable through the use of the dielectrophoresis body force. The phenomenon of dielectrophoresis is explained in detail in Reference 1. In summary, it is a force which can act on a particle placed in a nonuniform electric field even if that particle does not possess a net electrical charge. By virtue of the charge displacements occurring on bodies in electric fields, an electrical body force arises. Experiments conducted by Gemant and Pohl (Refs. 22, 23) have indicated that motion of the particles, either solid or liquid, can be achieved. To verify these results, similar tests were conducted. In addition some original work was done on the motion of droplets of water in a simulated "Zero-G" model.

DESCRIPTION OF TEST APPARATUS

Figure 78 shows the entire test set-up. At the right is the D.C. high-voltage power supply; next to it is a neon transformer connected to a Variac to provide a variable source of high A.C. voltage. The test model, located at the center of the picture, is shown enlarged in Figure 79. Several electrodes of various shapes are shown at the left of the glass container. The test model is a glass container approximately 8 inches in diameter; one electrode lead extends through a sealed stem at its right side. For these tests, one of the electrodes was fastened to the lead in the container, and another was mounted in the electrode holder directly above the center of the container. The electrical field was applied between the upper and the lower electrodes. The container was filled with fluid consisting of a mixture of one half each of CCl_4 and silicone D.C. 200 fluid. The fluids were mixed in an attempt to obtain a fluid that was nonconducting but had the same specific gravity as that of water. It had been anticipated that the fluids were completely miscible, but an interface formed between two phases of the fluid at which it was possible to suspend droplets of water.

TEST RESULTS

Figures 80 and 81 illustrate the electric wind effects. The point used as the central electrode is located just above the surface of the liquid. The lower electrode, directly beneath it, is in the fluid at the bottom of the container. When a field is applied, waves are generated on the surface of the liquid as the corona wind strikes the surface. This phenomenon is the same as that considered previously in the sections on heat transfer.

The next series of pictures indicate the effect of a nonuniform A.C. field on the fluid. The central electrode, shown in Figure 82, is a round ball approximately 1/8 inch in diameter located 3/16 inch above the surface of the fluid. The lower electrode is the same as was used before. When the A.C. voltage is applied, the fluid jumps up and clings to the surface of the ball, as shown in Figure 83. A ring central electrode was placed above the surface as shown in Figure 84. Figure 85 shows the fluid clinging to the wire under the action of the field. These experiments merely represent pictorial verification of Gemant's and Pohl's work.

The last pictures illustrate the action of the nonuniform field on suspended water droplets. Figure 86 shows the fluid model. The upper electrode is a small round surface electrically insulated by a very heavy coating of wax, and the lower electrode is a sheet of aluminum foil placed below and outside the glass container. The nonuniform field is established between these two electrodes. Two relatively large droplets of water can be seen suspended upon the interface existing within the fluid model. After the field was applied, the water droplets moved slowly toward the central electrode and, upon reaching it, coalesced to form a single droplet. This sequence portrays the actual existence of the nonuniform field body force. Considerable care had to be exercised in conducting the tests in order to observe the phenomenon. Whenever a bare central electrode was used, the droplet would be repelled and broken up upon reaching it.

These exploratory tests are included solely to demonstrate that nonuniform field effects actually exist. It was not possible in the time available to obtain and use accurate instrumentation. Approximately 4000 volts A.C. were required to move the droplets of water but, unfortunately, currents were not measurable with the A.C. milliammeter available. The pictures, however, do indicate that some measure of fluid orientation and control are possible with the nonuniform electric fields.

SUMMARY OF ELECTRIC FIELD-FLUID INVESTIGATION

Starting with the fundamental question, what are the possible effects of an electrostatic field on the boundary layer and heat transfer in a fluid, an entire field of investigation was opened. The review of literature and theory in several fields of endeavor revealed that a broad range of influences were possible. The question that followed was, were the phenomena controllable and useful?

Two series of experiments were then conducted to determine whether or not the influences could be controlled or made to provide useful results. One series consisted of determining the effects of corona wind on free-convection heat transfer. An extensive experimental and analytical program proved that large changes in heat transfer occurred with the application of electric fields. The correlation between theory and test data appeared to be very good. While the actual magnitudes of the heat transfer coefficients were not predicted exactly, the indicated trends were in excellent agreement. The second series of experiments were purely exploratory and were accomplished to demonstrate some actions of the dielectrophoresis phenomenon.

CONCLUSIONS AND RECOMMENDATIONS

As a result of the over-all survey to determine the possible interactions between electric fields and fluids, it was concluded that many possible actions exist. The actions include:

1. Ion-drift phenomena due to an applied field
2. Charged-particle motion in an A.C. field
3. Phoresis motions
4. Dielectrophoresis phenomena
5. Changes in fluid properties with applied fields.

Because of these actions, body forces are available of sufficient magnitude to perform useful functions. Prior experiments have indicated that both partially ionized and neutral fluids can be influenced. It appears logical to utilize these body forces in carefully selected regions of the fluid, in the boundary layer, for example, to provide changes in heat transfer or drag.

The experimental work conducted in this study clearly indicates that a sizeable change in heat transfer can be obtained through the use of the corona discharge. The application of the Von Karman integral equations and electric field theory lead to an analytical solution which correlates well with the test data for a typical test configuration. The demonstration tests of dielectrophoresis, likewise, indicate that motion of neutral fluids and particles is possible with nonuniform A. C. electric fields.

It is believed that the phenomena involved in electrofluidmechanics can have significant importance in a wide range of fluid mechanic and heat transfer problems. Much basic work must be done, however, to understand the various phenomena, their limitations, and their scope.

It is recommended that a continuing effort be expended in this area. Many possible avenues of research are evident, including effects on viscosity, thermal conductivity, transition, separation, drag, and heat transfer. Potential areas of application may be large if the phenomena can be controlled at will.
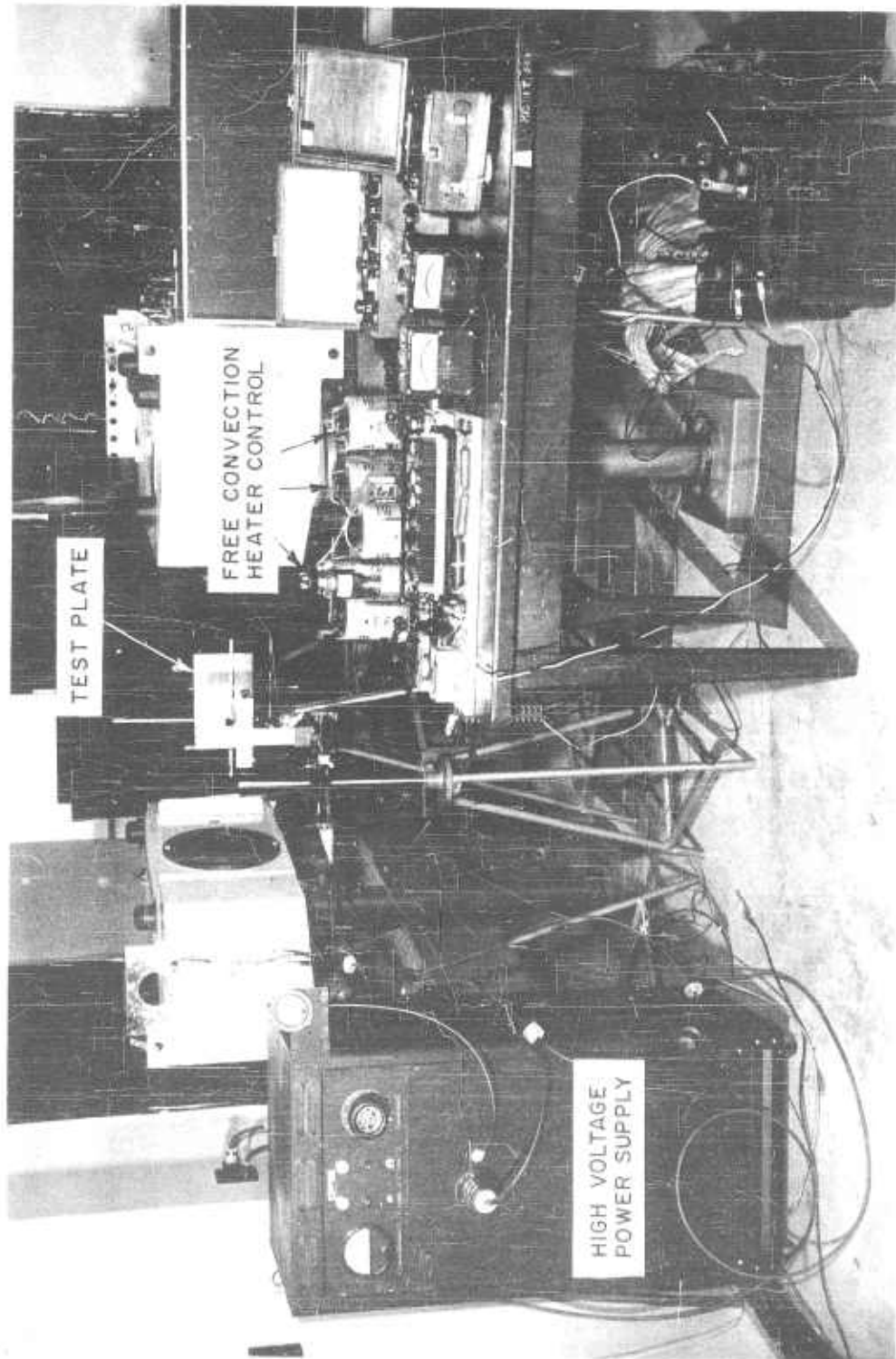
Figure 2. Over-all view of interferometer installation
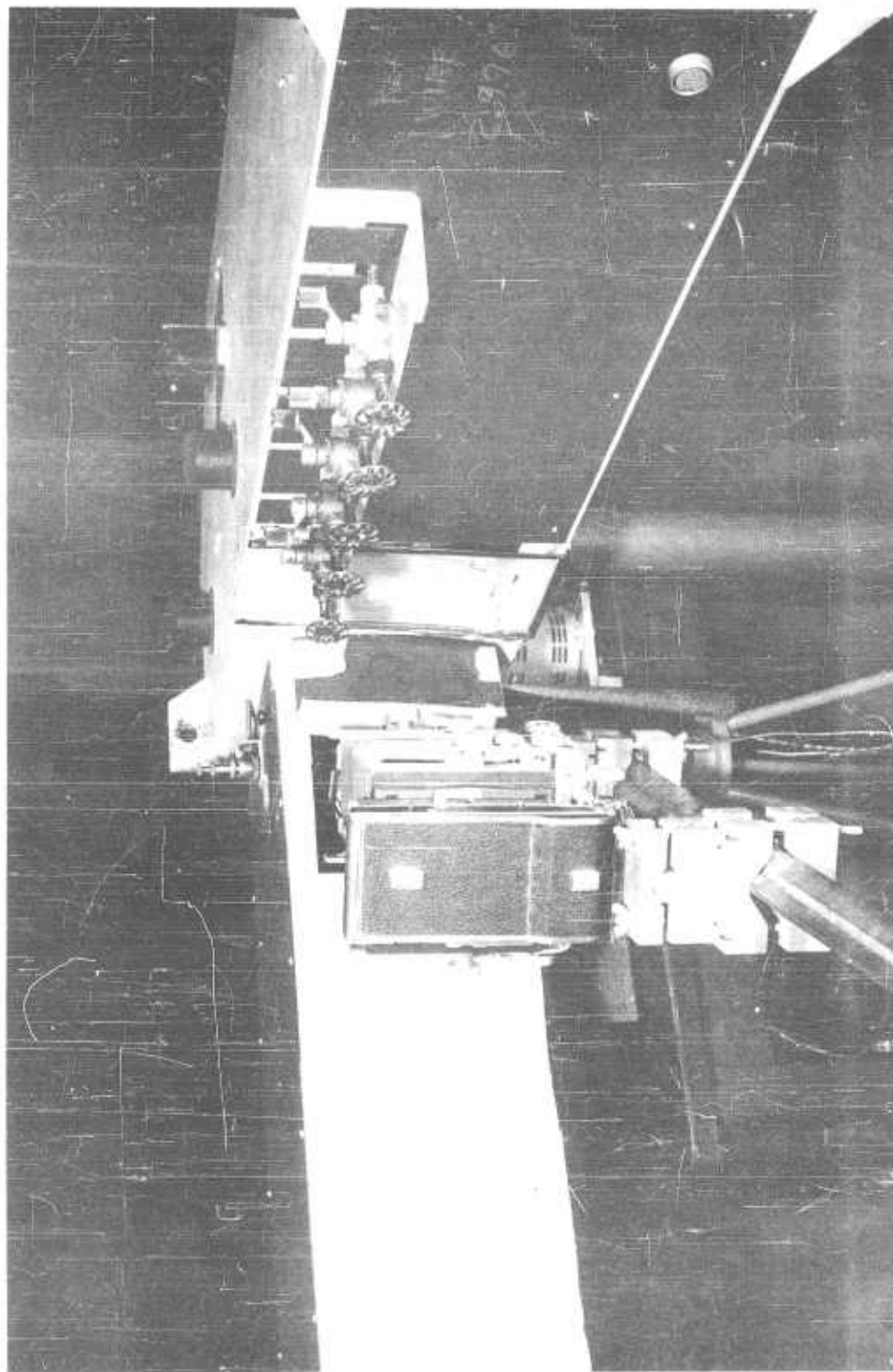
Figure 3. Close-up of camera mounting on interferometer
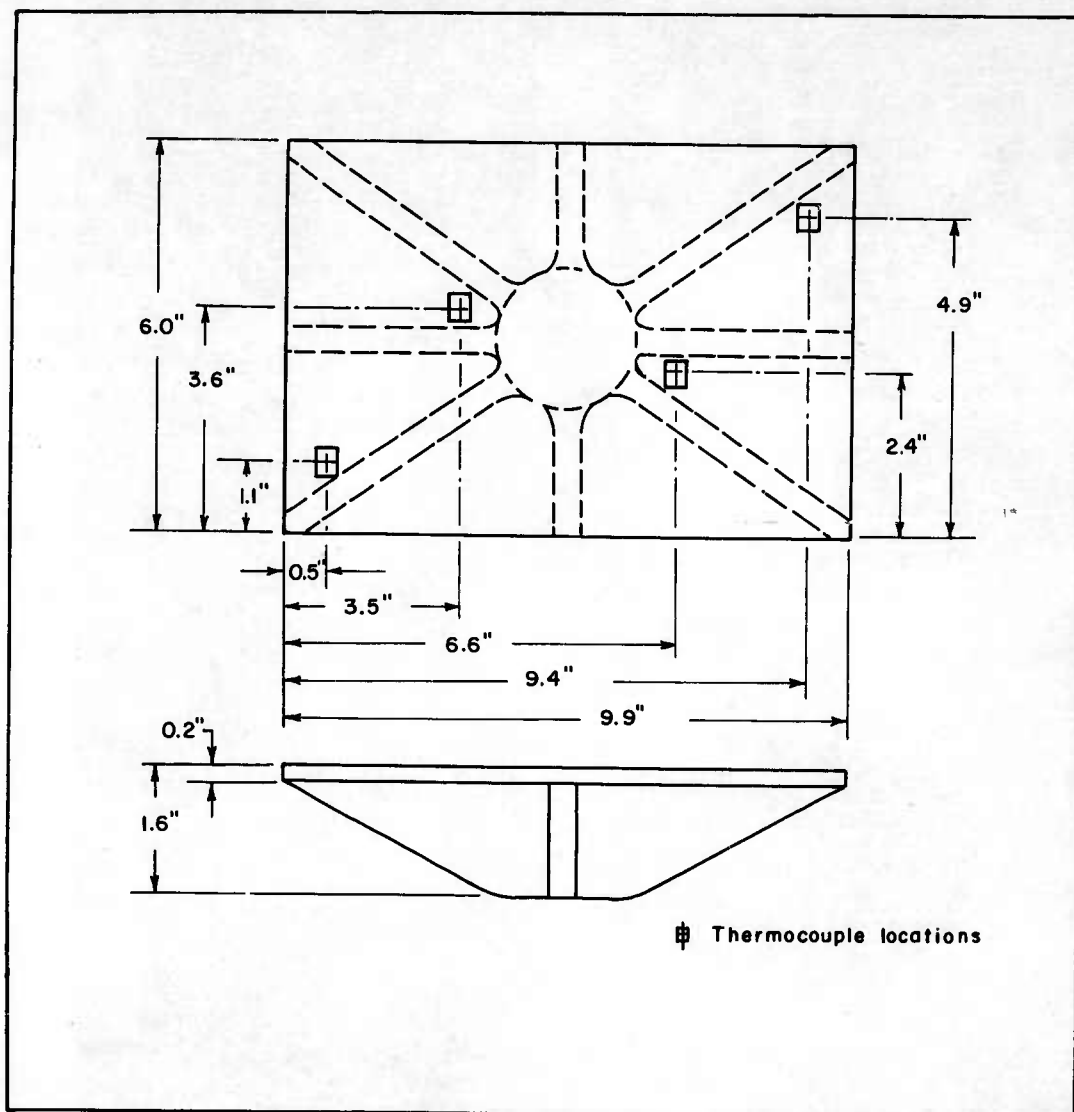
Figure 4. Location of thermocouples on heated plate
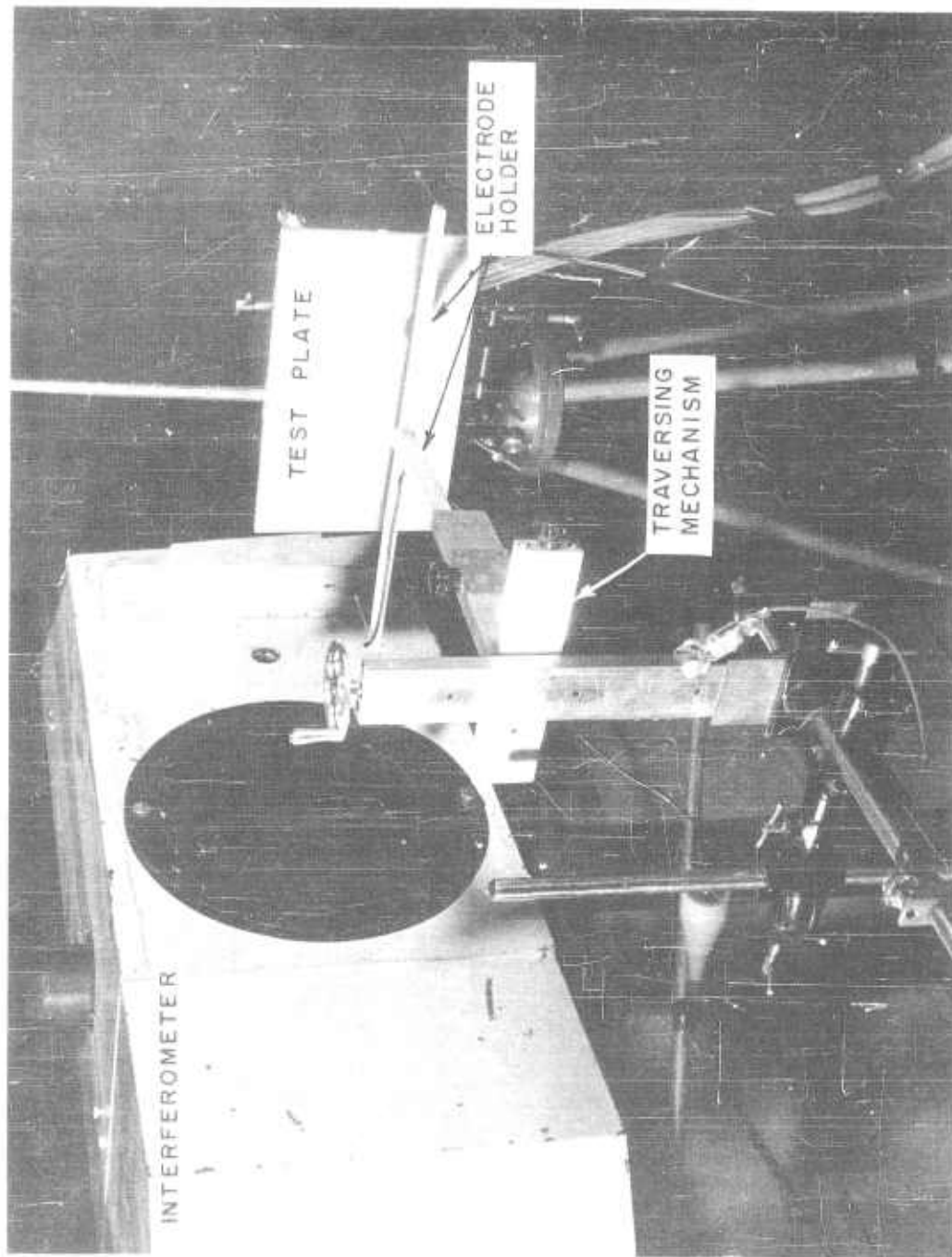
Figure 5. Typical interferometer installation of heated plate and electrode
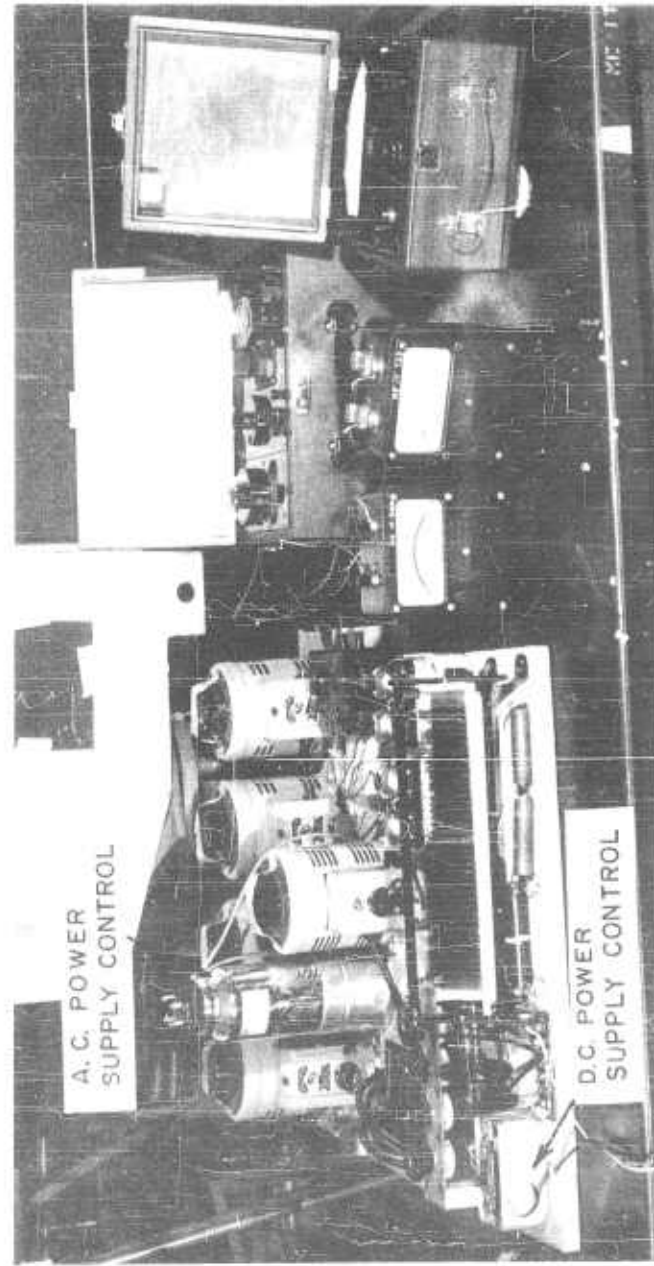
Figure 6. Heater power supply

FLAT ALUMINUM PLATE

GRID

OVAL ELECTRODE

ROW OF NEEDLES
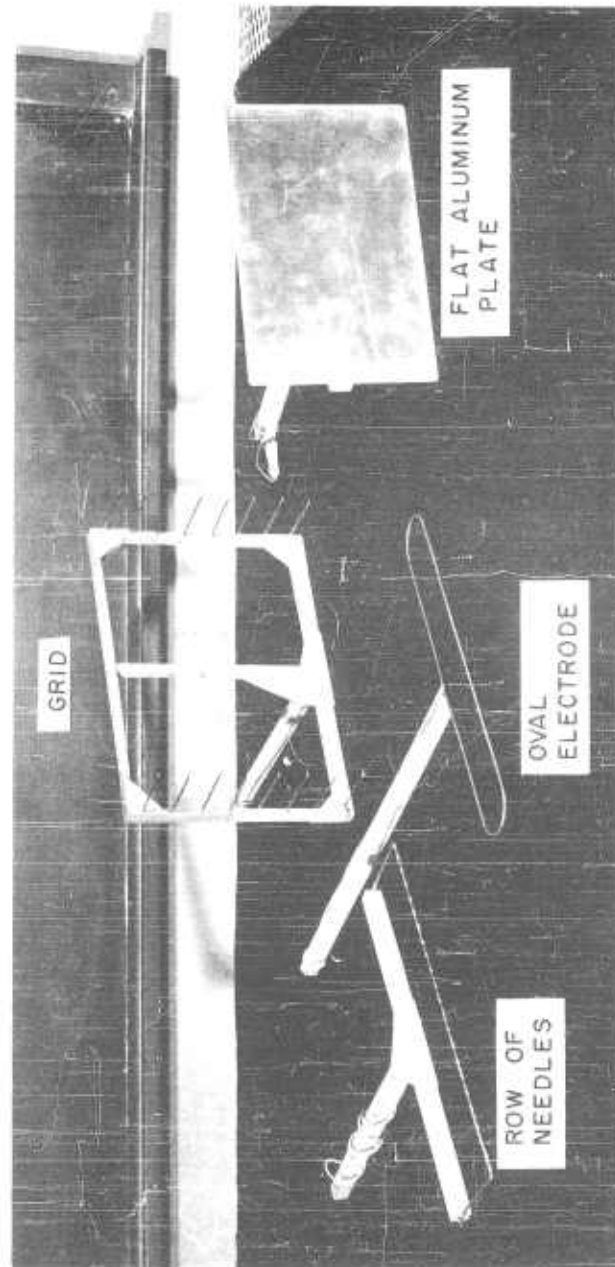
Figure 7. Electrodes for interferometer tests

Figure 8. Over-all view of inclined manometer showing spotlight and 7 x 12-inch plate
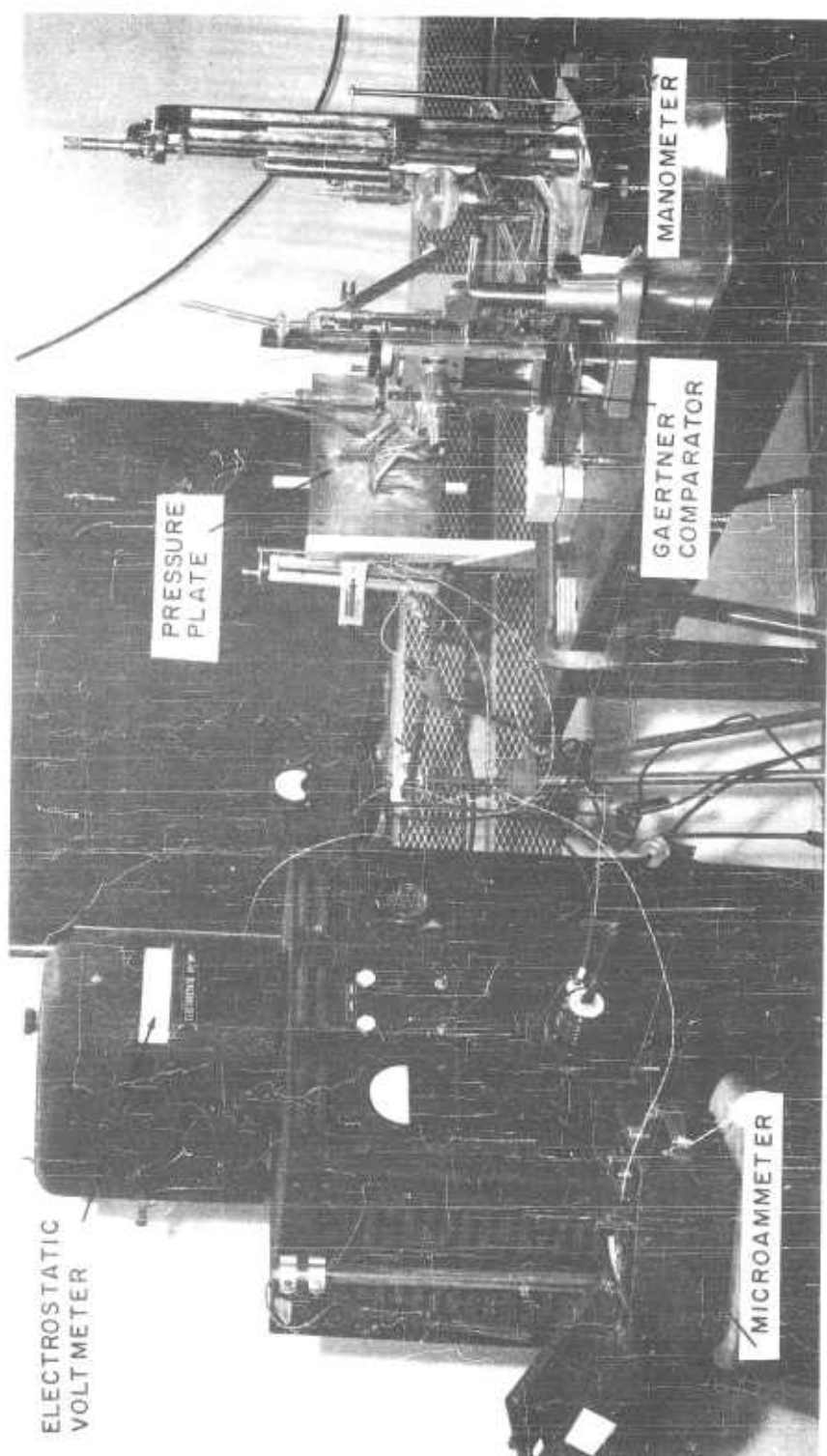
Figure 9. Over-all view of pressure survey arrangement using Chattock micromanometer

62
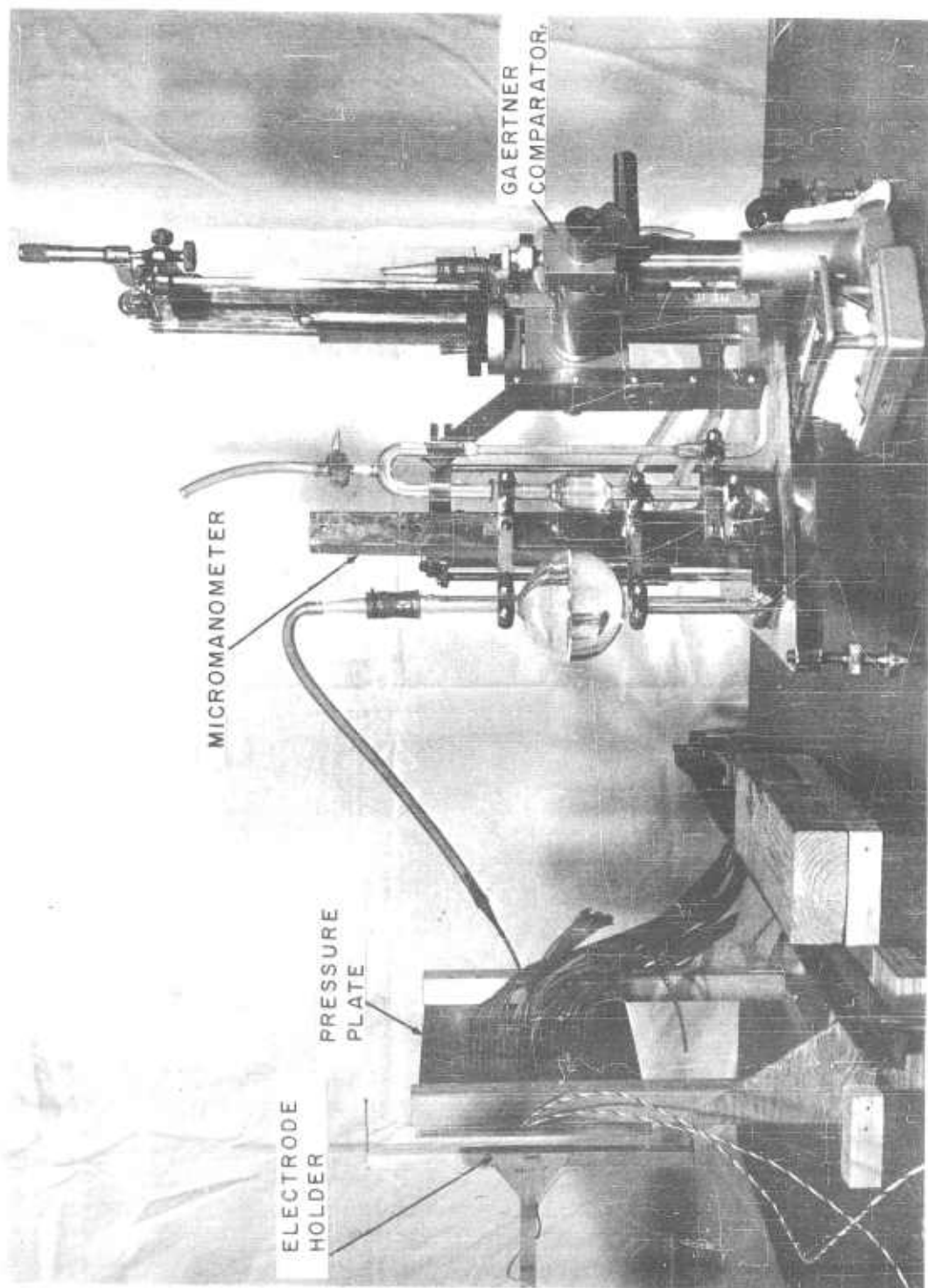
Figure 10. Close-up view of Chattock micromanometer and Gaertner comparator
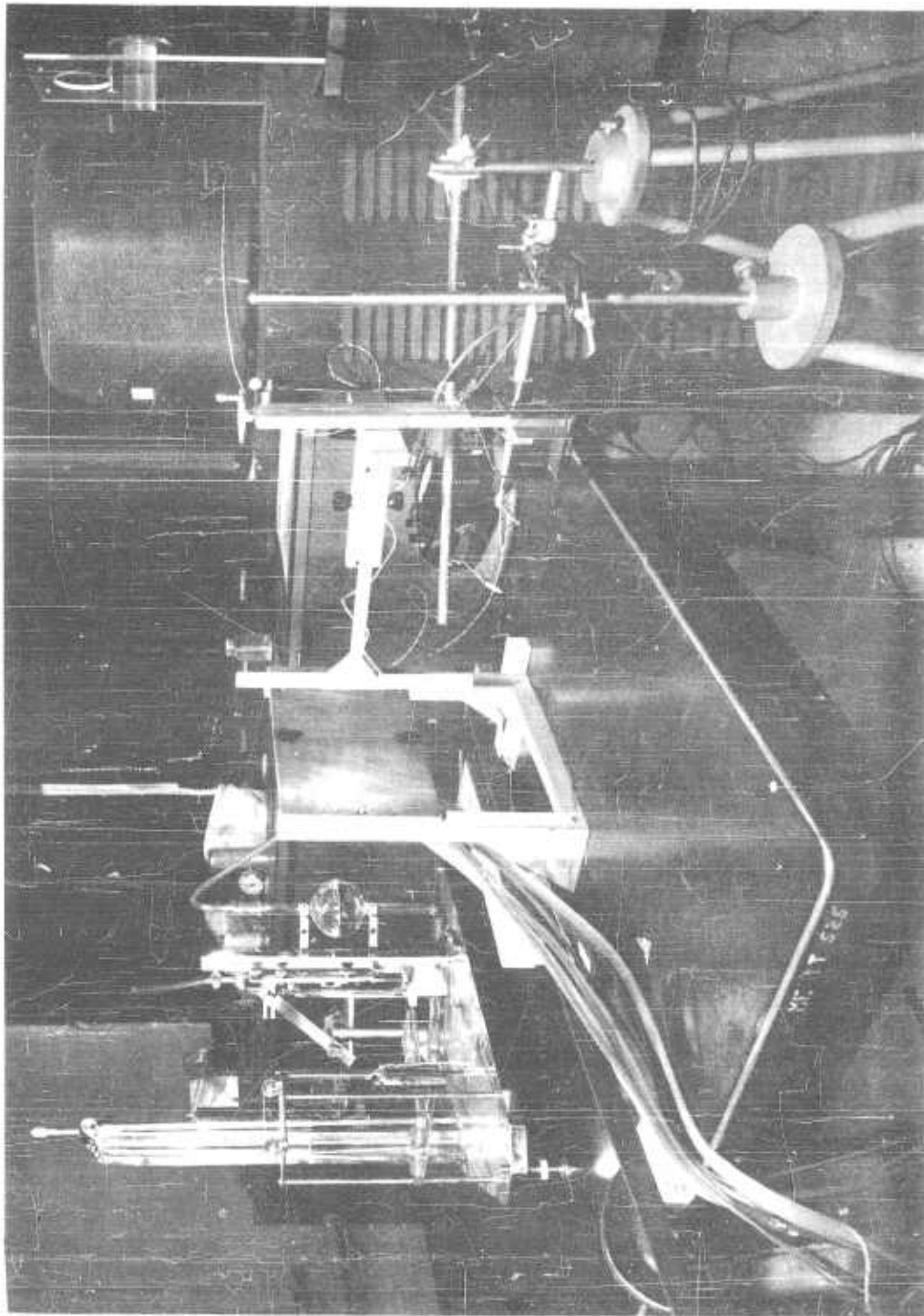
Figure 11. Corona wind pressure plate set-up showing electrode in place
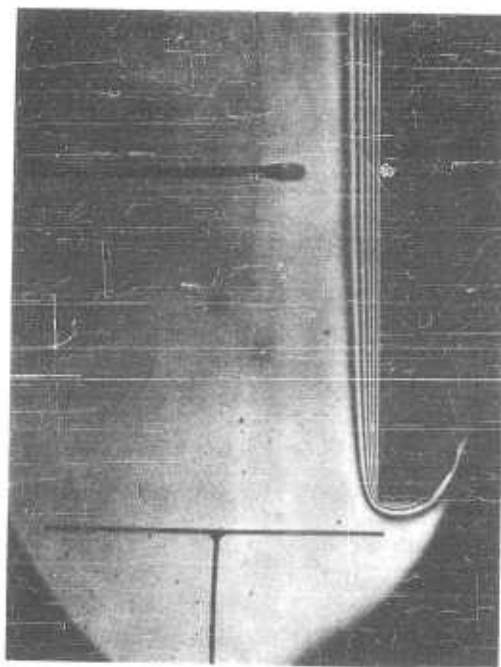
Figure 12. Typical picture as seen with the interferometer, no applied field
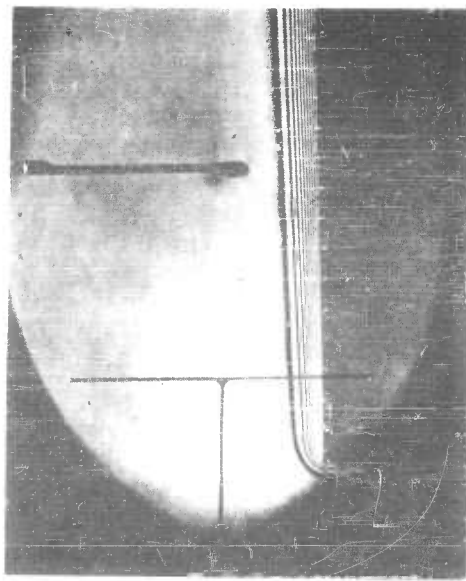
A. No electric field   0 KV   B. 5.41 KV   0.70 microamps
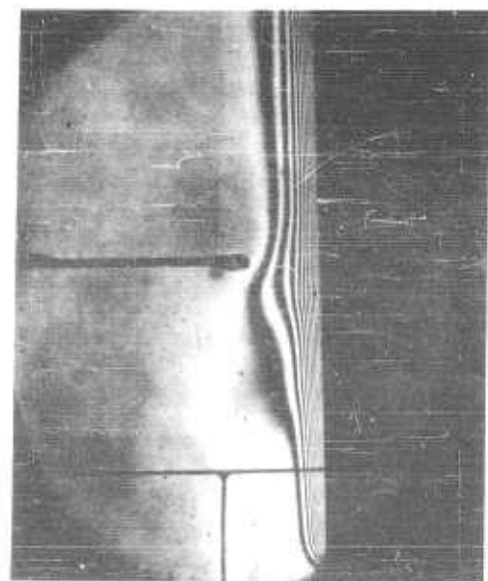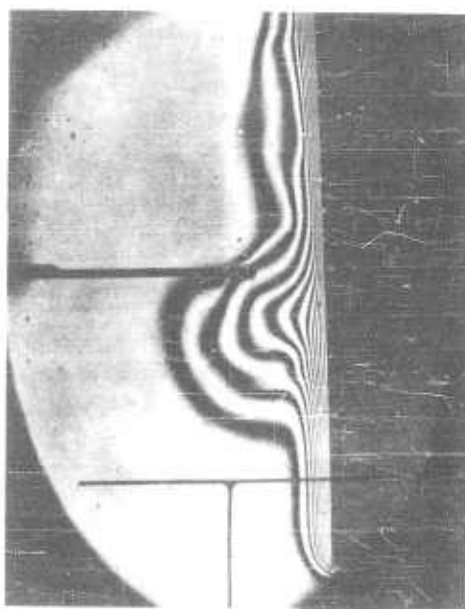
C. 5.8 KV   1.85 microamps   D. 6.1 KV   3.10 microamps
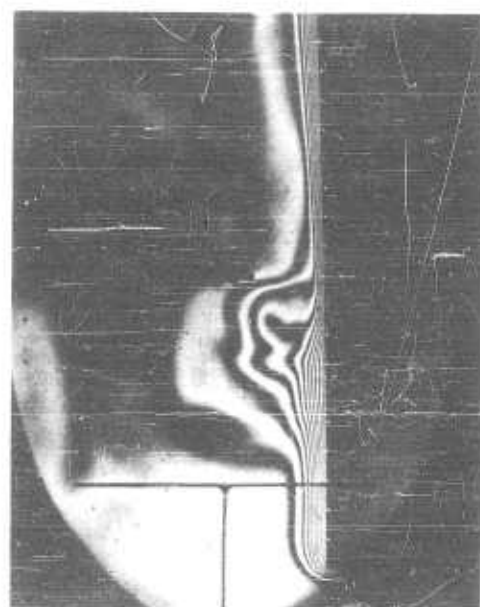
Figure 13. Interferometer pictures of the effects of corona discharge on heat transfer. Vertical
heated plate, plate temperature approximately 119°F, room temperature 69°F, wire
0.004 inch in diameter, 2 cm in front of plate at centerline
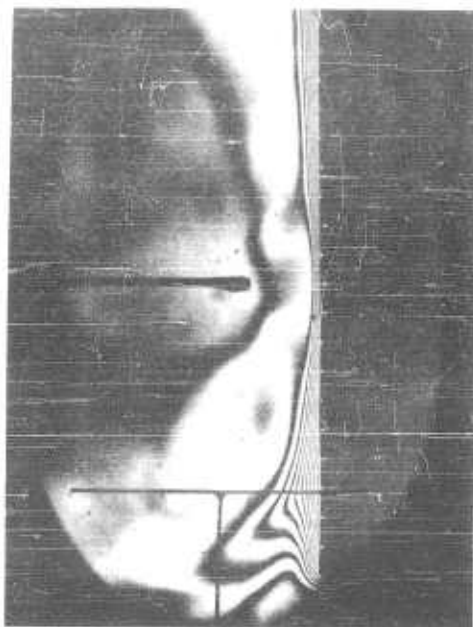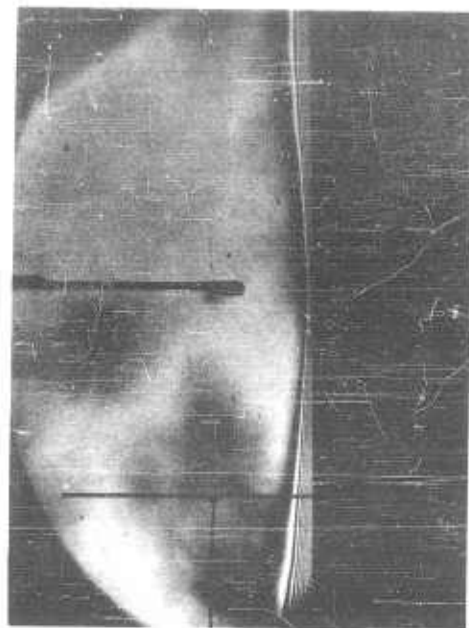
E. 6.4 KV   5.9 microamps   F. 7.5 KV   22.8 microamps
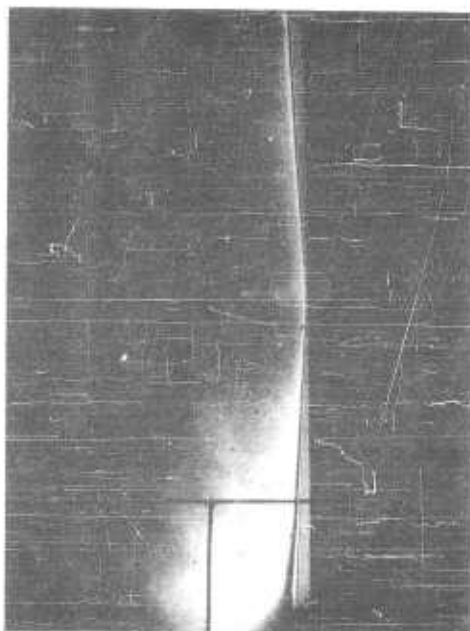
G. 10.0 KV   74.2 microamps   H. 13.4 KV   193 microamps
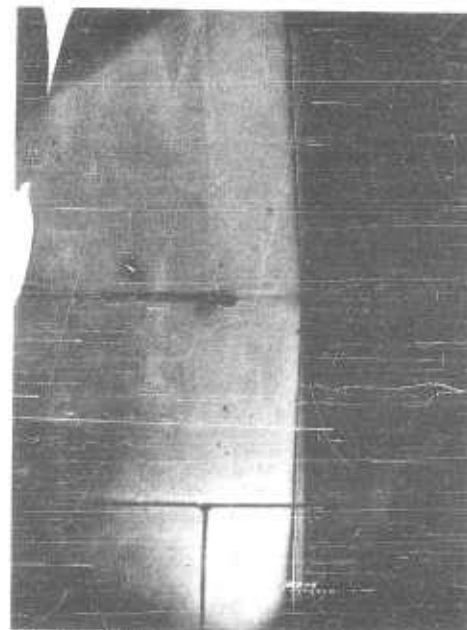
Figure 13 (Cont'd). Interferometer pictures of the effects of corona discharge on heat transfer. Vertical
heated plate, plate temperature approximately 119°F, room temperature 69°F, wire
0.004 inch in diameter, 2 cm in front of plate at centerline
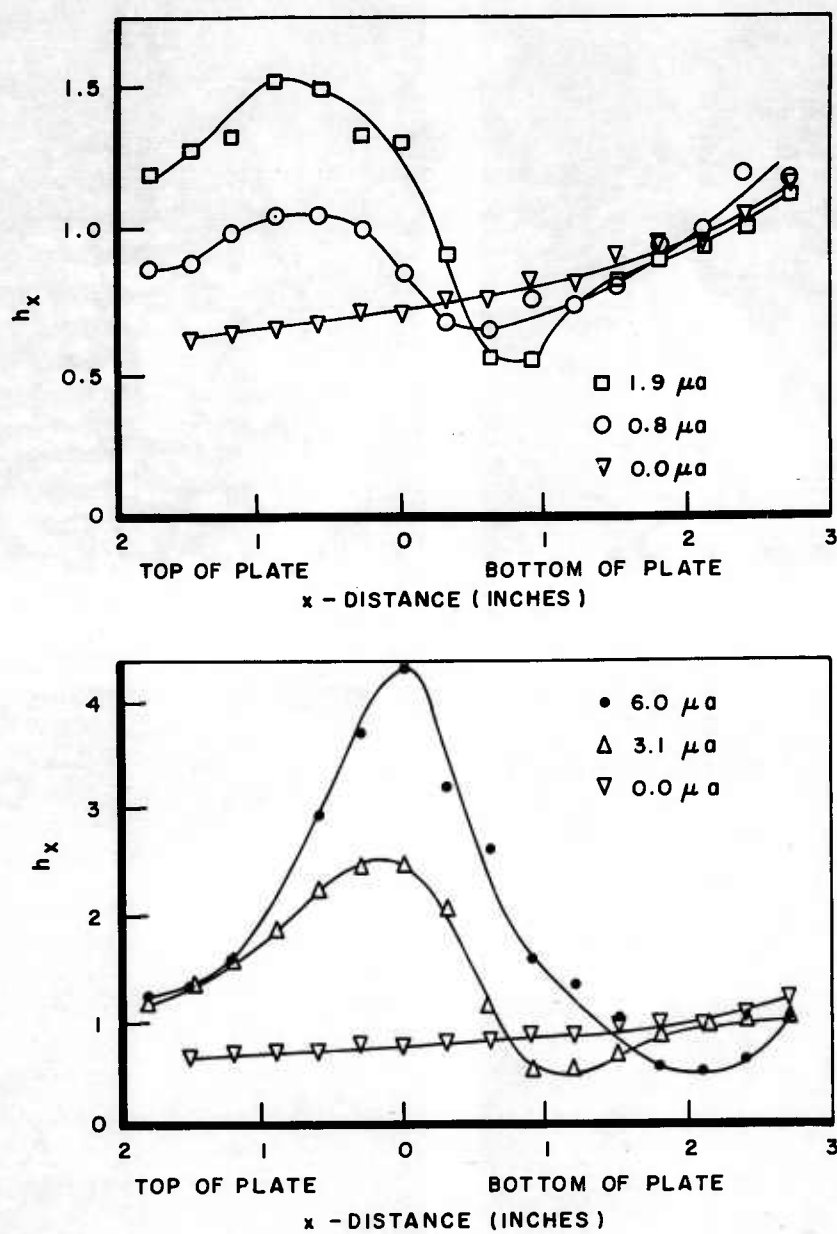
Figure 14. Heat transfer coefficients for vertical plate, with a 0.004-inch diameter
wire located 2 cm from centerline, corresponding to photographs of
Figure 13
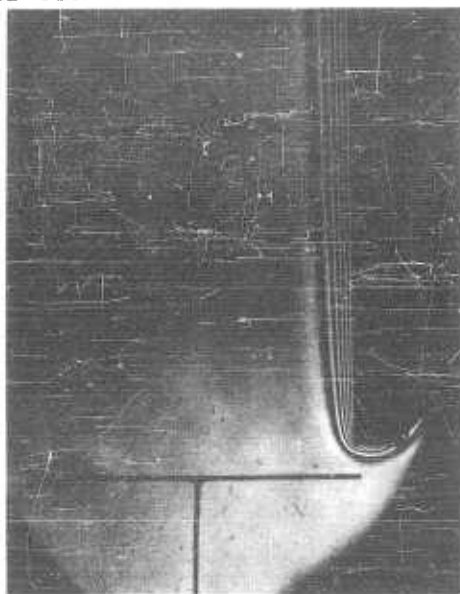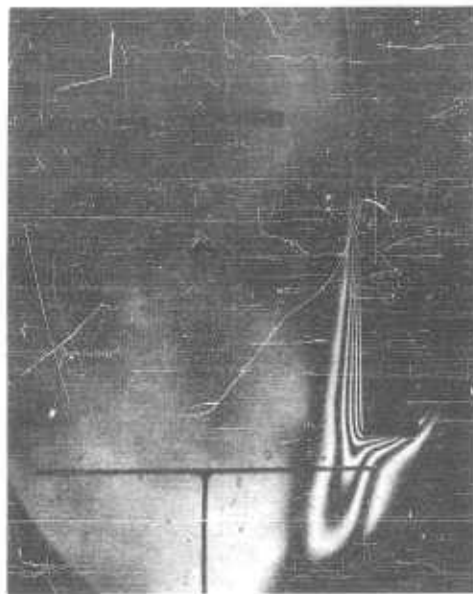
A. 0 KV   0.0 mieroamps   B. 6.3 KV   9.9 microamps
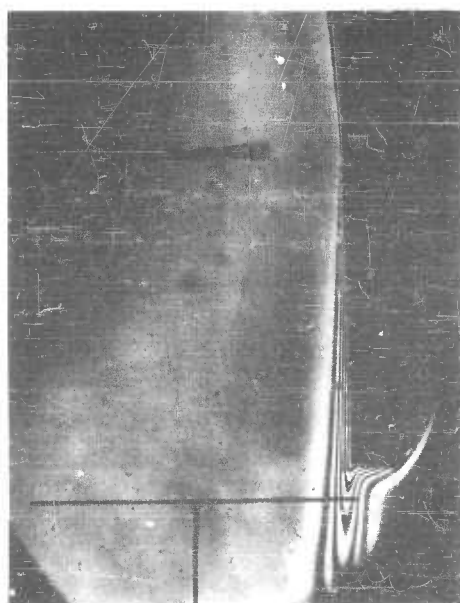
C. 6.7 KV   19.9 microamps   D. 11.7 KV   162 microamps
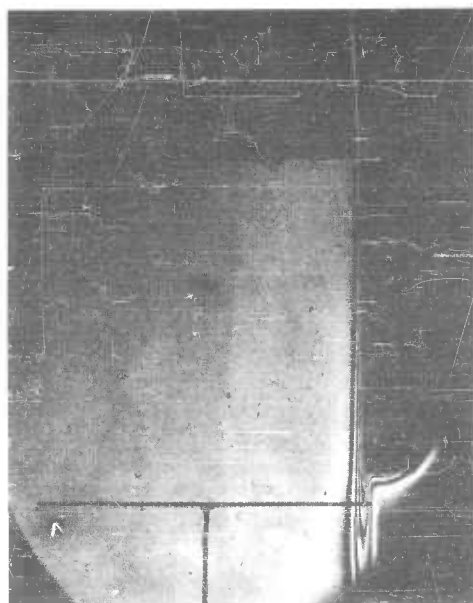
Figure 15. Effects of corona discharge on heat transfer. Vertical heated plate,
room temperature 64°F, ΔT held constant at 27°F, 0.004-inch wire
located 2 cm from plate at centerline
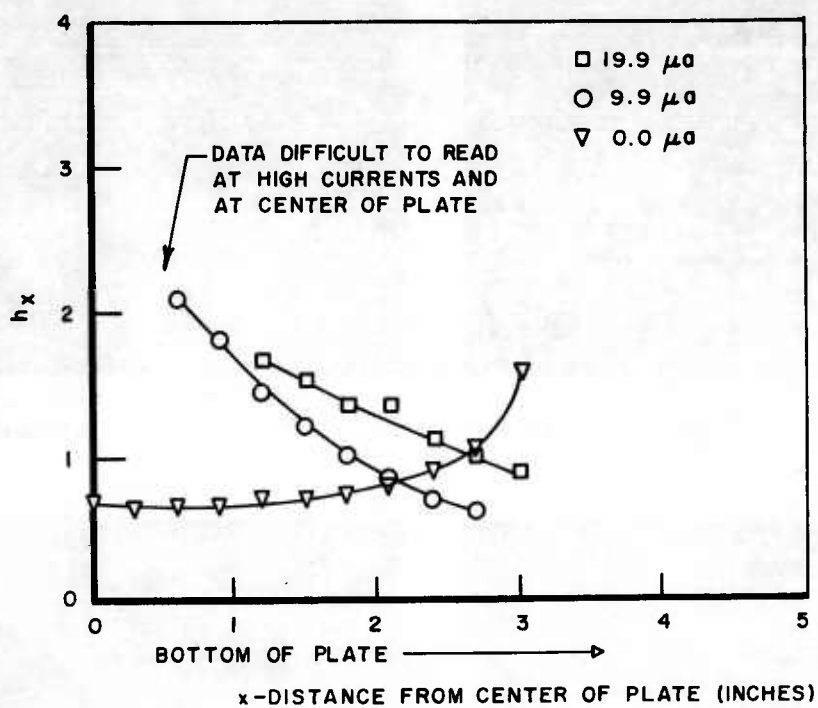
Figure 16. Heat transfer coefficients for vertical plate, 0.004-inch wire located
2 cm from centerline, corresponding to photographs of Figure 15
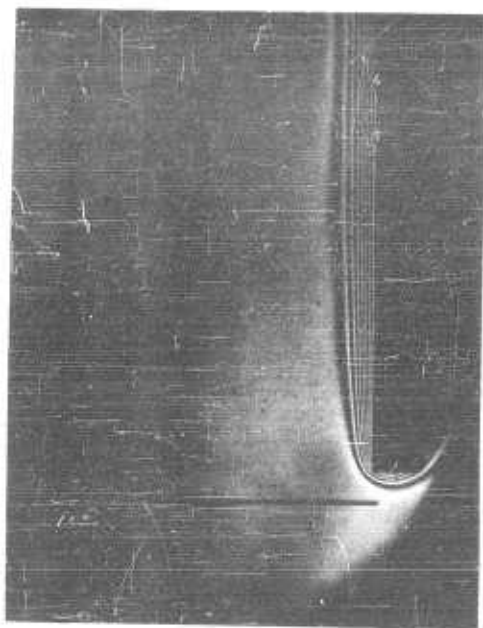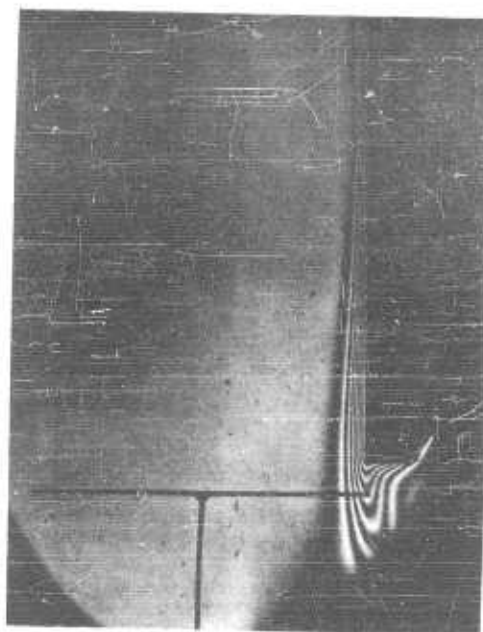
A.   0 KV   0 microamps   B.   8.3 KV   4.8 microamps
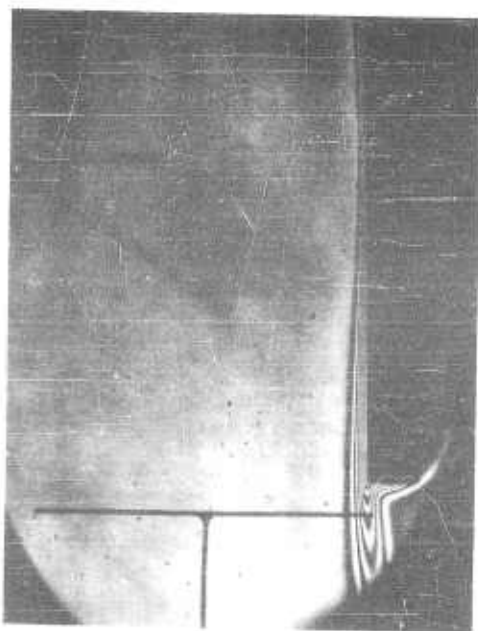
C.   11.5 KV   19.9 microamps   D.   23.3 KV   158 microamps

Figure 17.   Effects of corona discharge on heat transfer. Vertical heated plate,
room temperature 61°F, Δ T held constant at 34°F, 0.004-inch wire
located 5 cm from plate at centerline
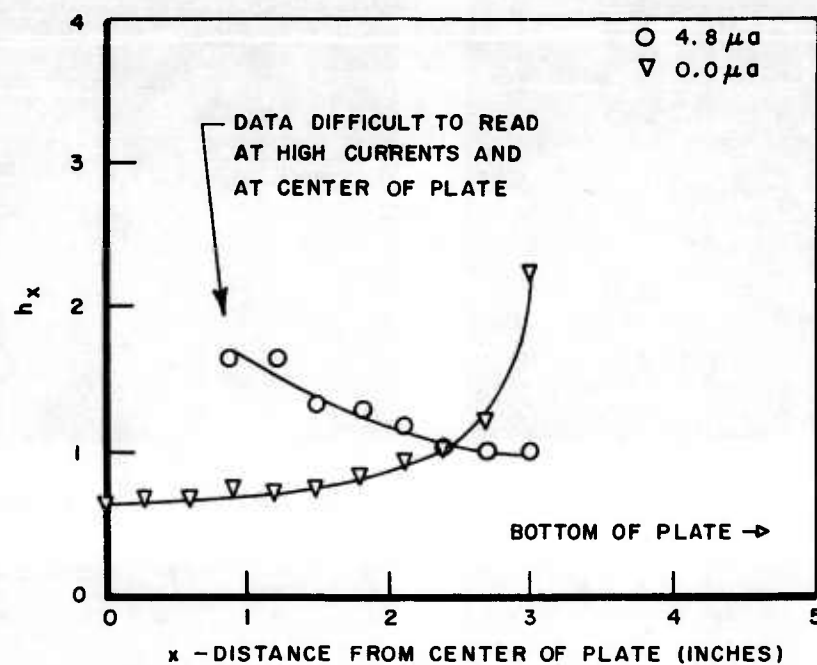
Figure 18. Heat transfer coefficients for vertical plate, with 0.004-inch wire located 5 cm from centerline
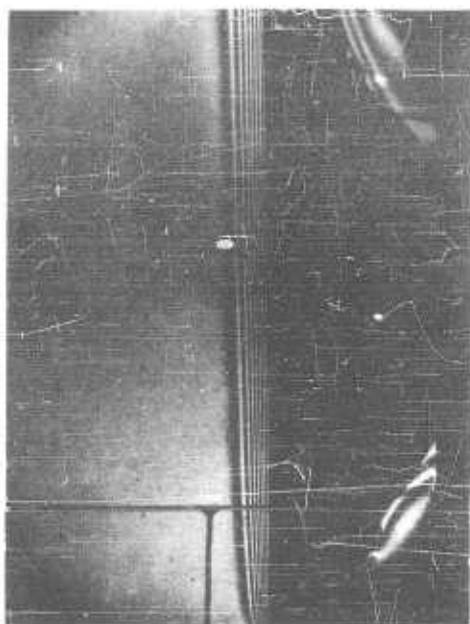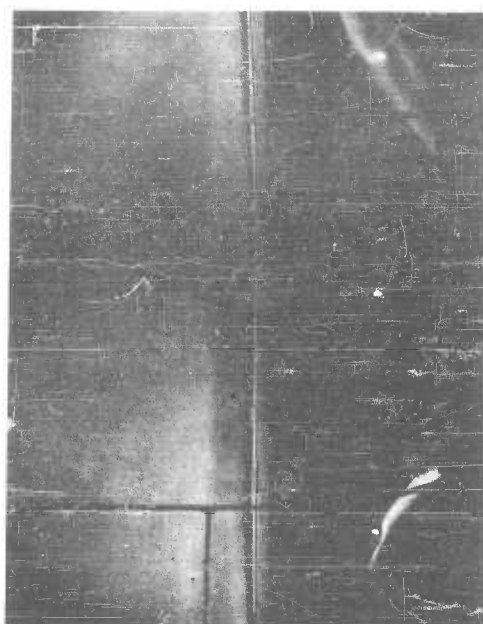
A. 0 KV   0 microamps   B. 12.5 KV   5.05 microamps
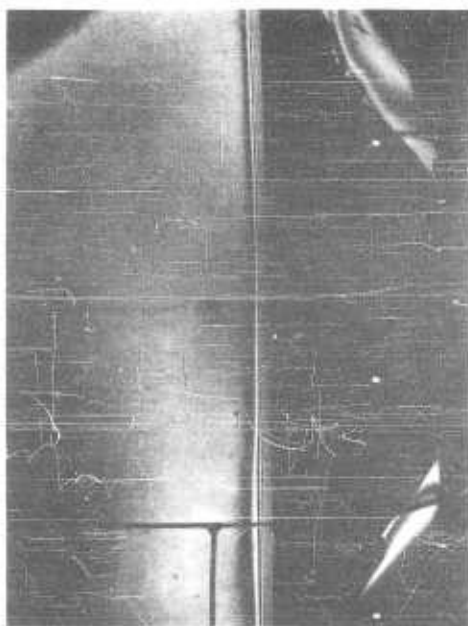
C. 15.2 KV   10.2 microamps   D. 25.2 KV   39.5 microamps
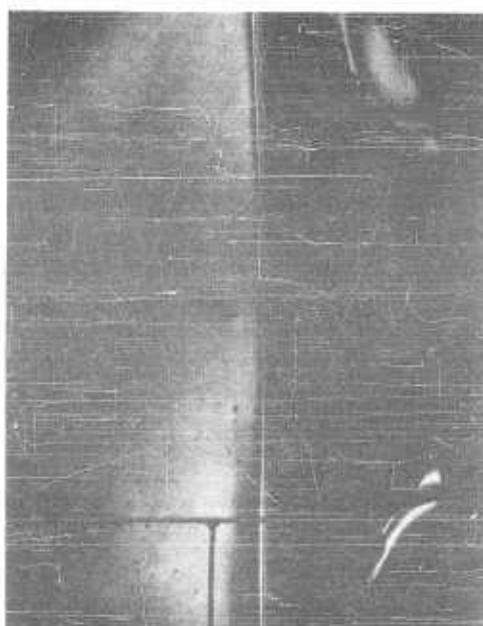
Figure 19. Effects of corona discharge on heat transfer. Vertical heated plate,
room temperature 53°F, Δ T held constant at 34°F, 0.004-inch wire
located 10 cm from plate at centerline
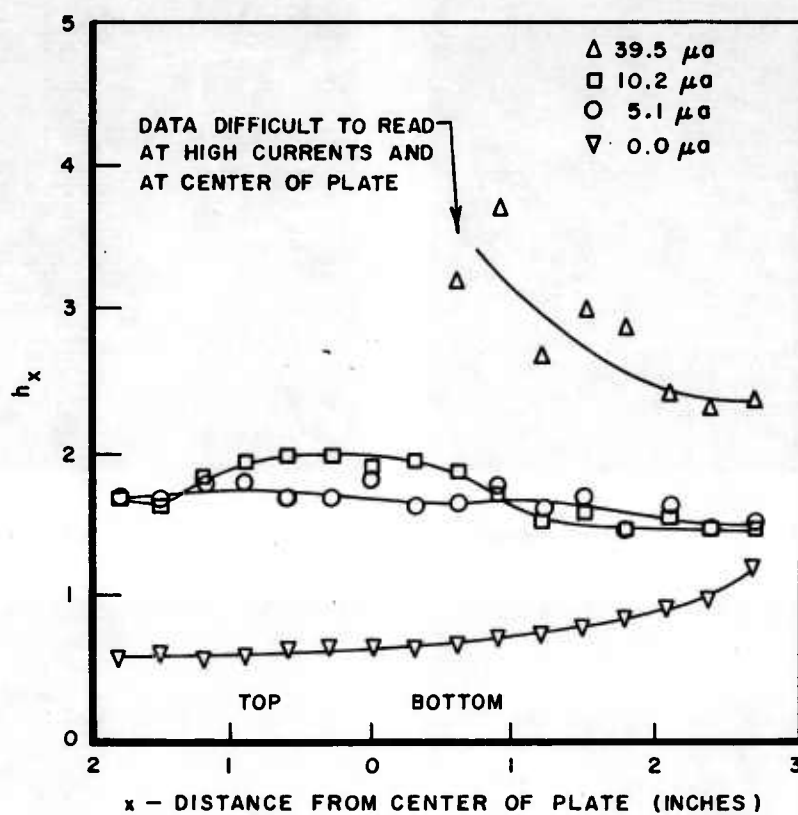
Figure 20. Heat transfer coefficients for vertical plate, with 0.004-inch wire located 10 cm from centerline

A. 0 KV   0 microamps

B. 5.0 KV   1.05 microamps

C. 5.2 KV   2.54 microamps

D. 5.7 KV   4.55 microamps

Figure 21. Effects of corona discharge on heat transfer. Horizontal heated plate,
room temperature 60°F, ΔT held constant at 27°F, 0.004-inch wire
located 2 cm from plate at centerline
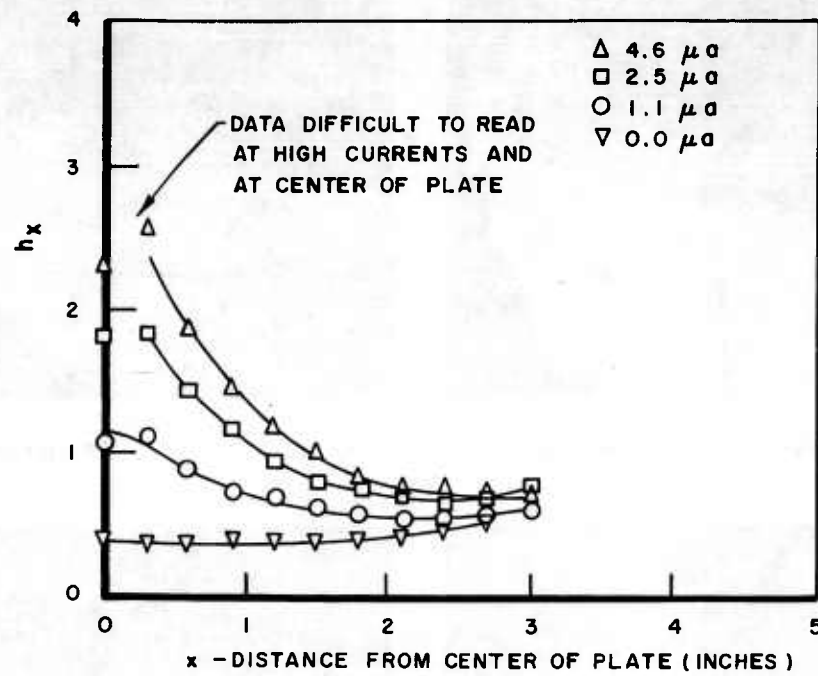
Figure 22. Heat transfer coefficients for horizontal plate, with 0.004-inch wire located 2 cm from centerline
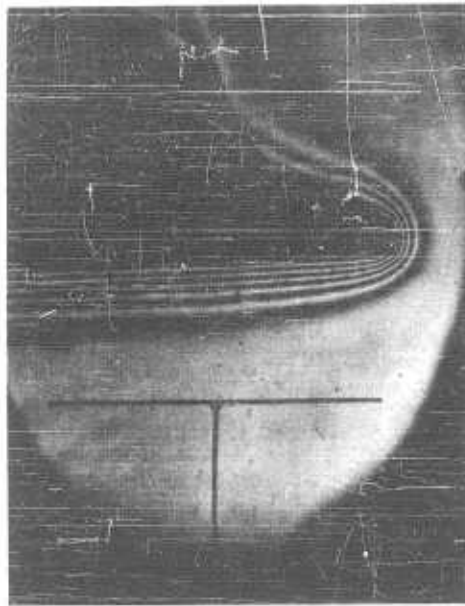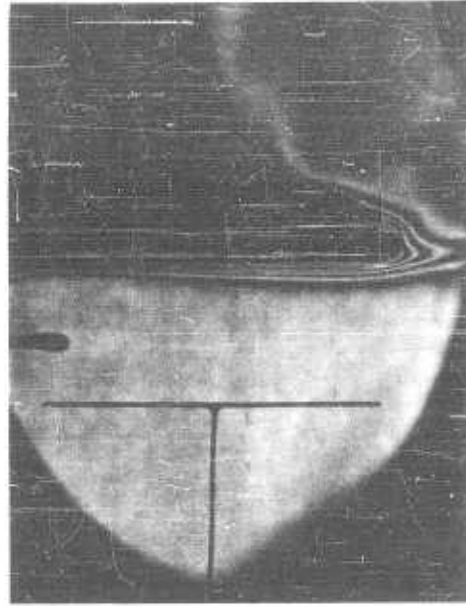
A. O KV   0 microamps   B. 6.3 KV   10.3 microamps

C. 8.0 KV   41 microamps   D. 11.0 KV   159 microamps

Figure 23. Effects of corona discharge on heat transfer. Horizontal heated plate, room temperature 61°F, ΔT held constant at 34°F, 0.004-inch wire located 2 cm from plate at centerline
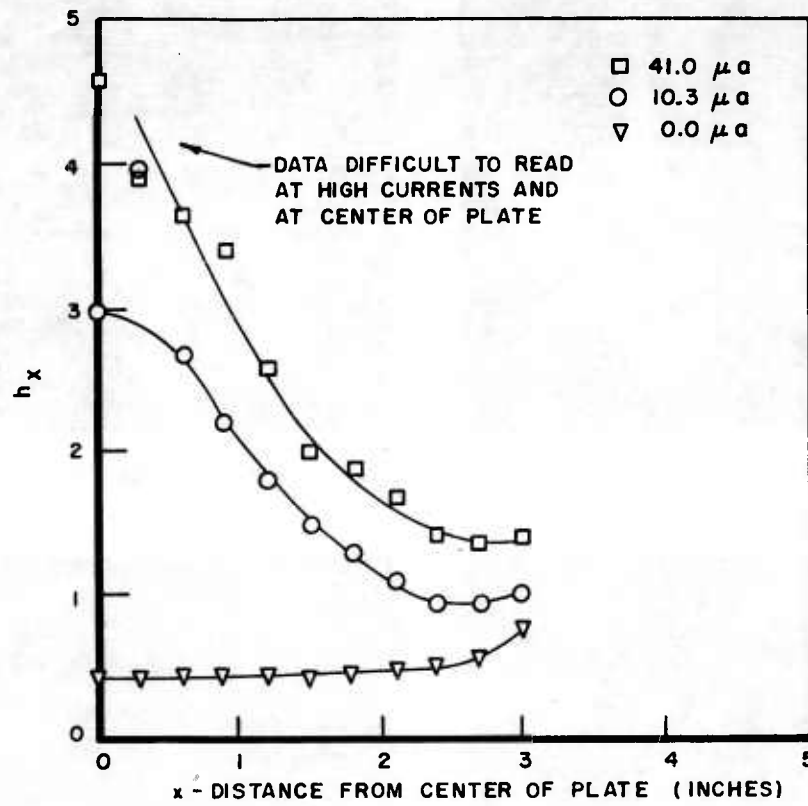
Figure 24. Heat transfer coefficients for horizontal plate, 0.004-inch wire located 2 cm from centerline, corresponding to photographs of Figure 23.

78

A.   0 KV   0 microamps   B.   8.7 KV   4.45 microamps

C.   11.8 KV   21.2 microamps   D.   23.3 KV   158 microamps

Figure 25. Effects of corona discharge on heat transfer. Horizontal heated plate,
room temperature 61°F, Δ T held constant at 34°F, 0.004-inch wire
located 5 cm from plate at centerline
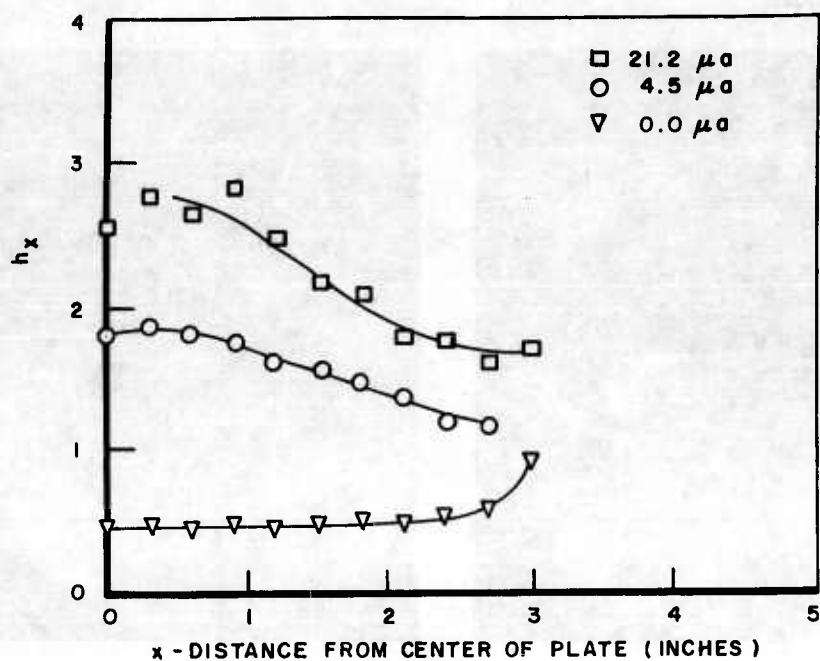
Figure 26. Heat transfer coefficients for horizontal plate, 0.004-inch wire located 5 cm from centerline
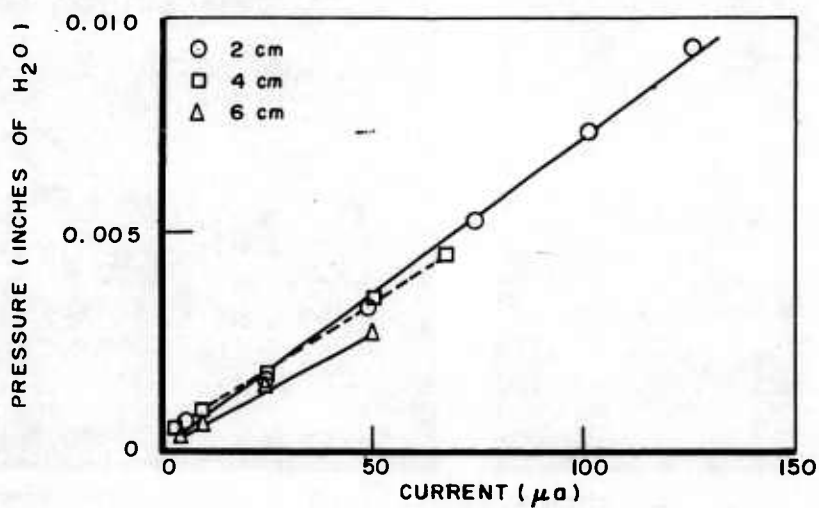
Figure 27. Stagnation pressure at the centerline of 7 x 12-inch flat plate for various wire spacings with a 0.0005-inch wire
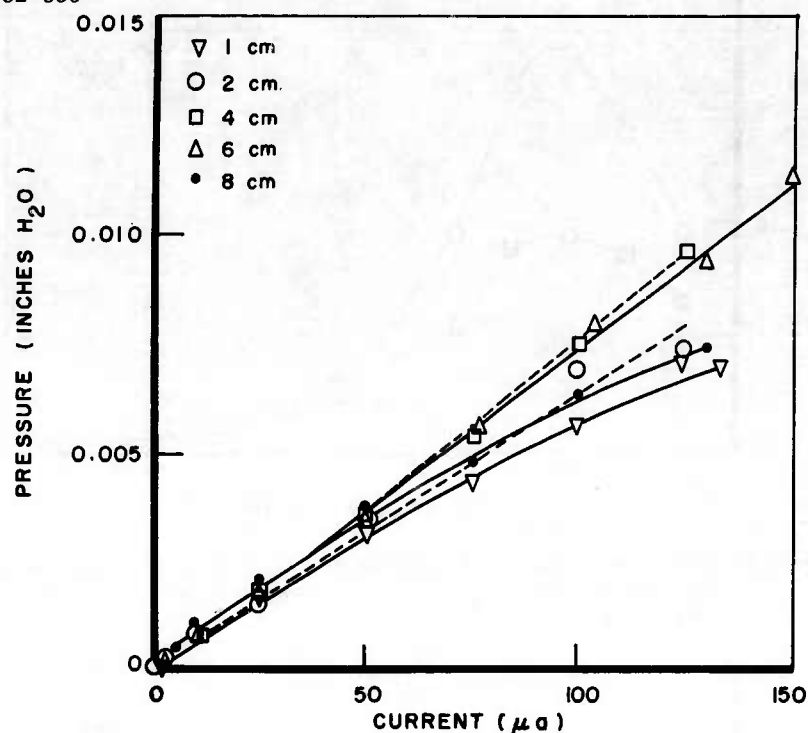
Figure 28. Stagnation pressure at centerline of the 7 x 12-inch flat plate for various wire spacings, wire diameter 0.004 inch
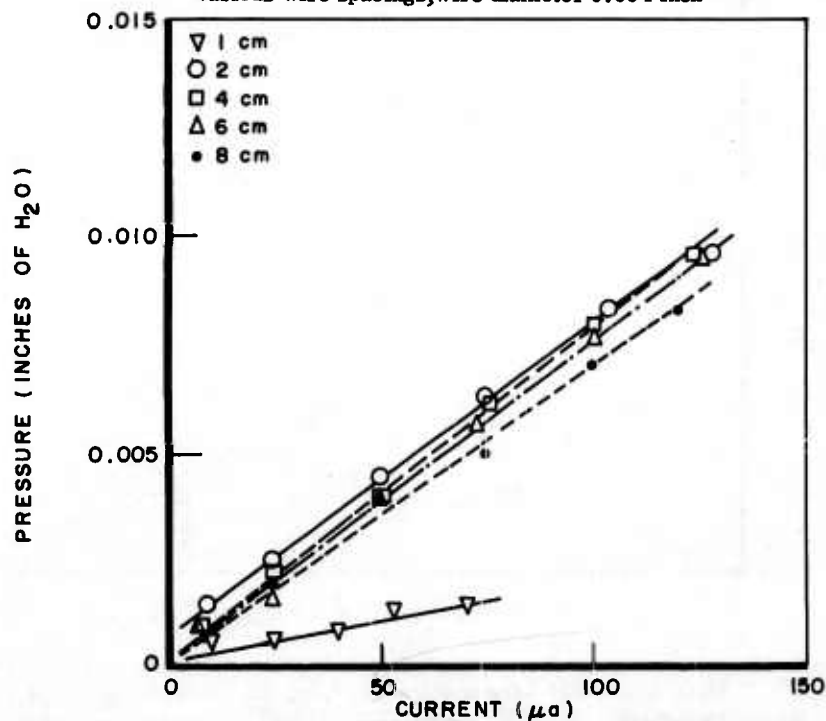
Figure 29. Stagnation pressure at centerline of the 7 x 12-inch flat plate for various wire spacings, wire diameter 0.010 inch
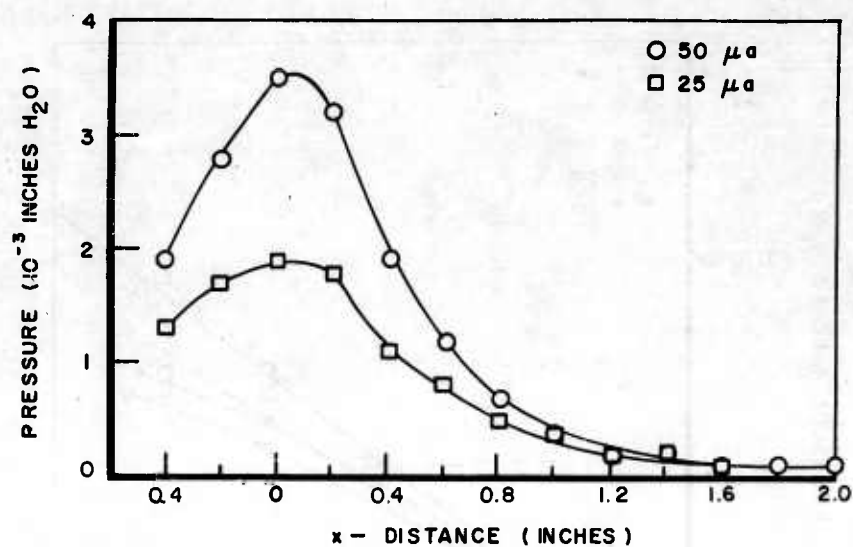
Figure 30. Corona wind pressure distribution over the surface of the 7 x 12-inch plate, 0.004-inch wire at centerline along the 7-inch dimension, 2 cm from plate
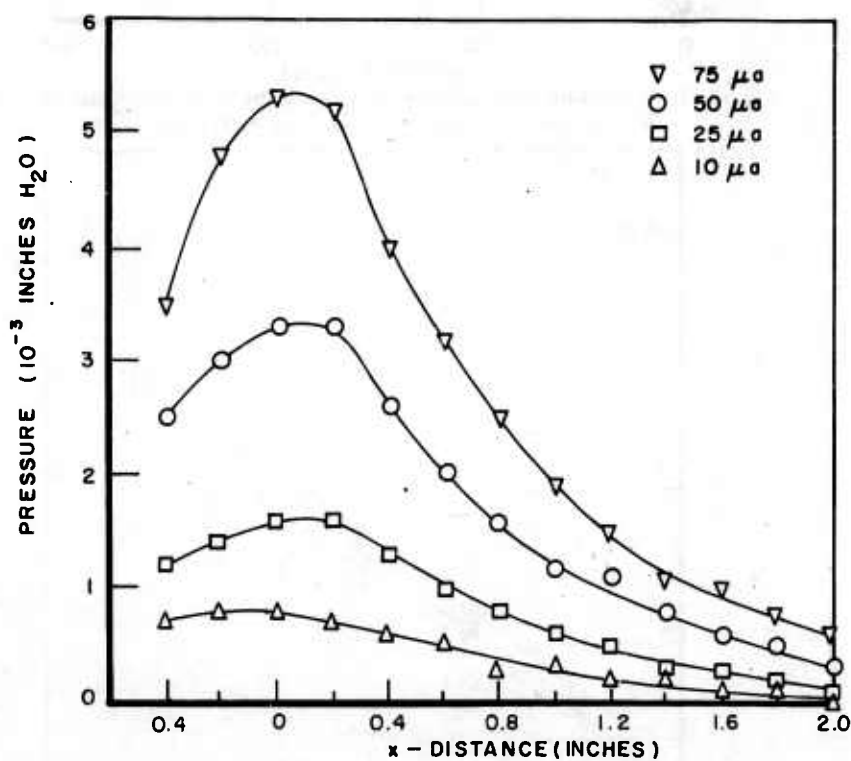
Figure 31. Corona wind pressure distribution over the surface of the 7 x 12-inch plate, 0.004-inch wire at centerline along the 7-inch dimension, 4 cm from plate
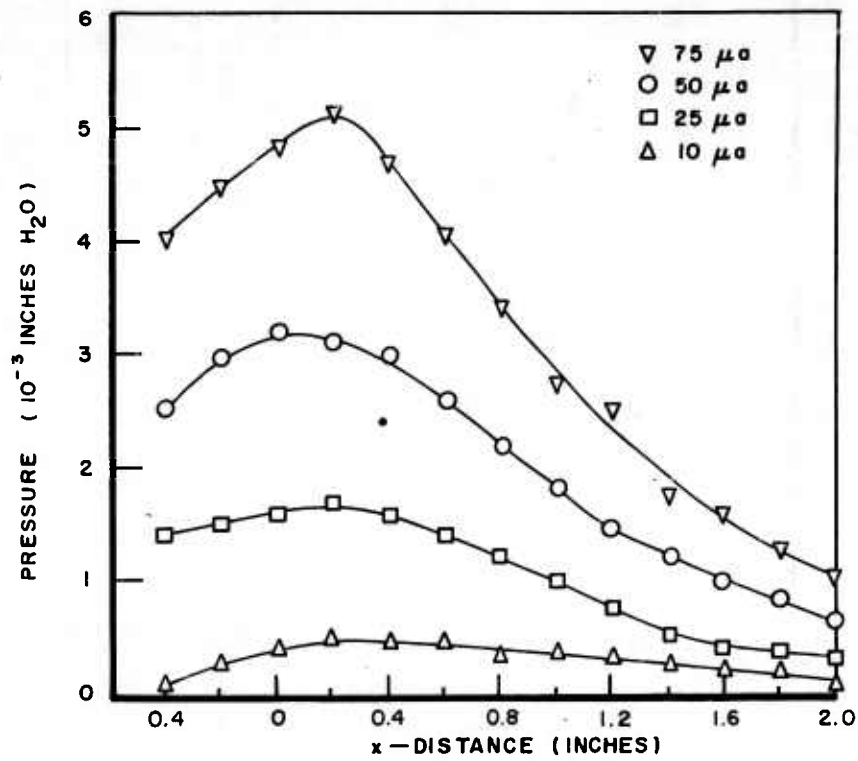
Figure 32. Corona wind pressure distribtuion over the surface of the 7 x 12-inch plate, 0.004-inch wire at centerline along 7-inch dimension, 6 cm from plate
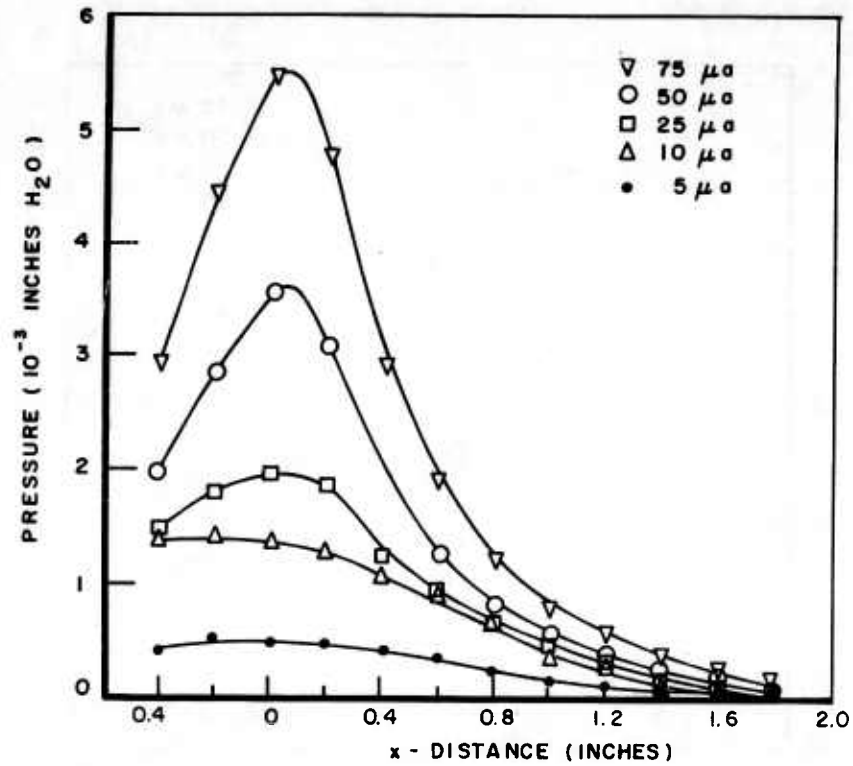
Figure 33. Corona wind pressure distribution over the surface of the 7 x 12-inch plate, 0.004-inch wire at centerline along 7-inch dimension, 2 cm from plate. (Data for low currents very erratic.)
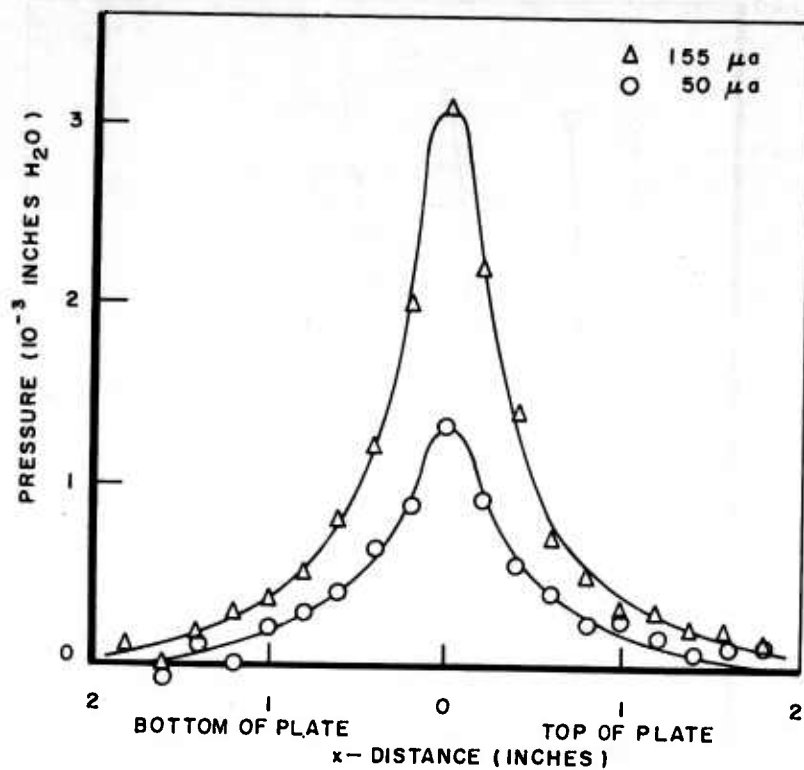
Figure 34. Typical pressure data from inclined manometer, a = 2 cm
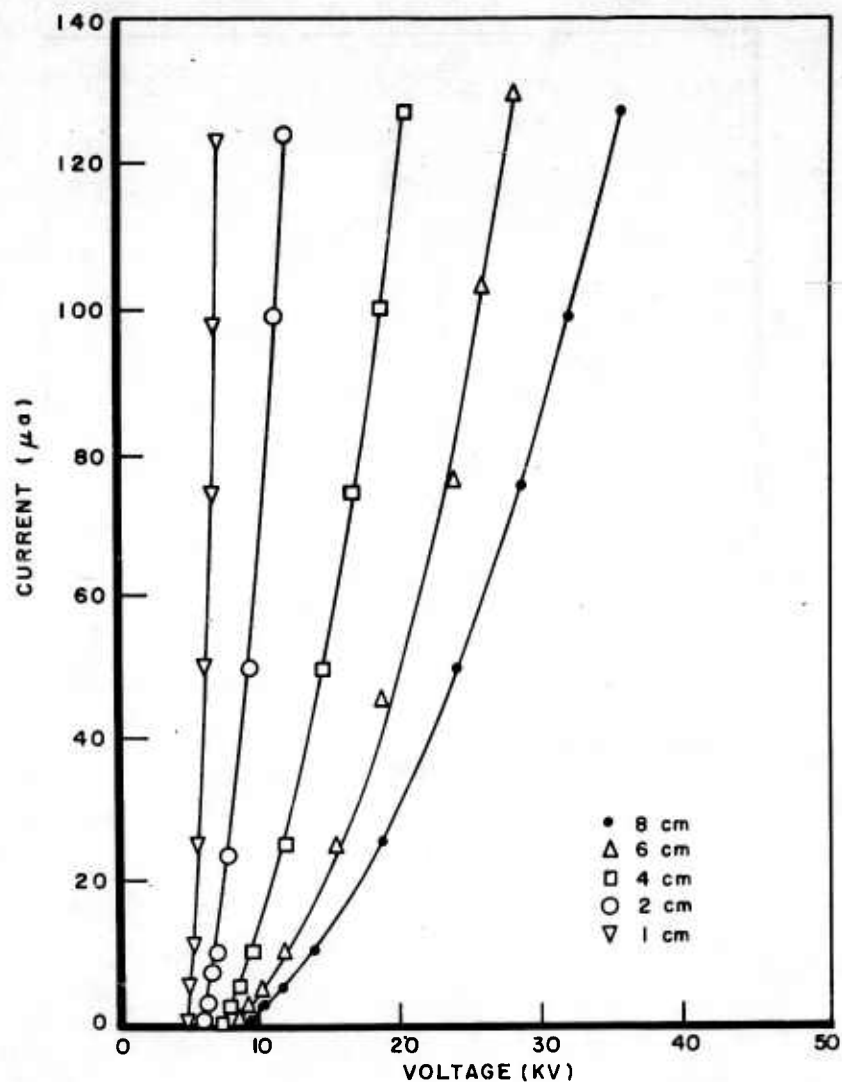
Figure 35. Typical current-voltage curves for a corona discharge with 0.004-inch
wire at centerline along 7-inch dimension of a 7 x 12-inch flat plate,
4 cm from centerline

86
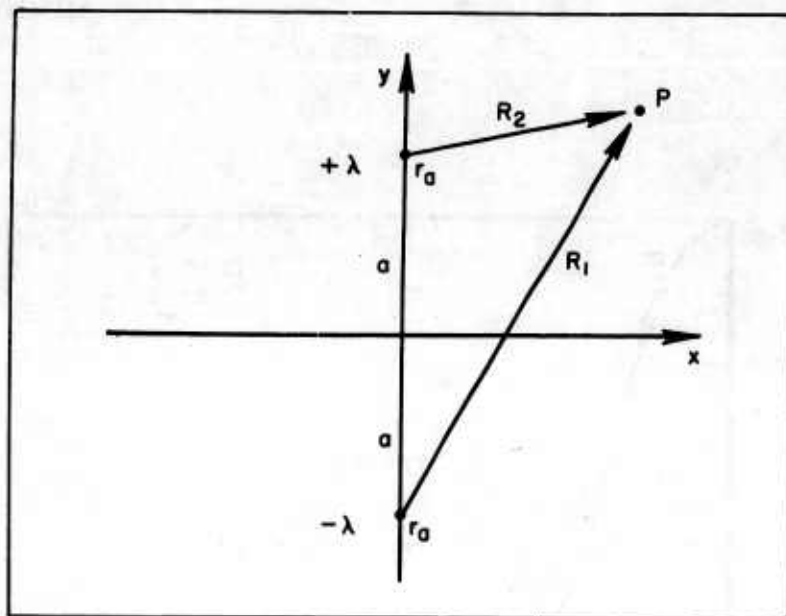
Figure 36. Field of a wire parallel to a plane

$$\frac{\rho}{\rho_c} = \frac{1}{(1 + z^2)^2}$$
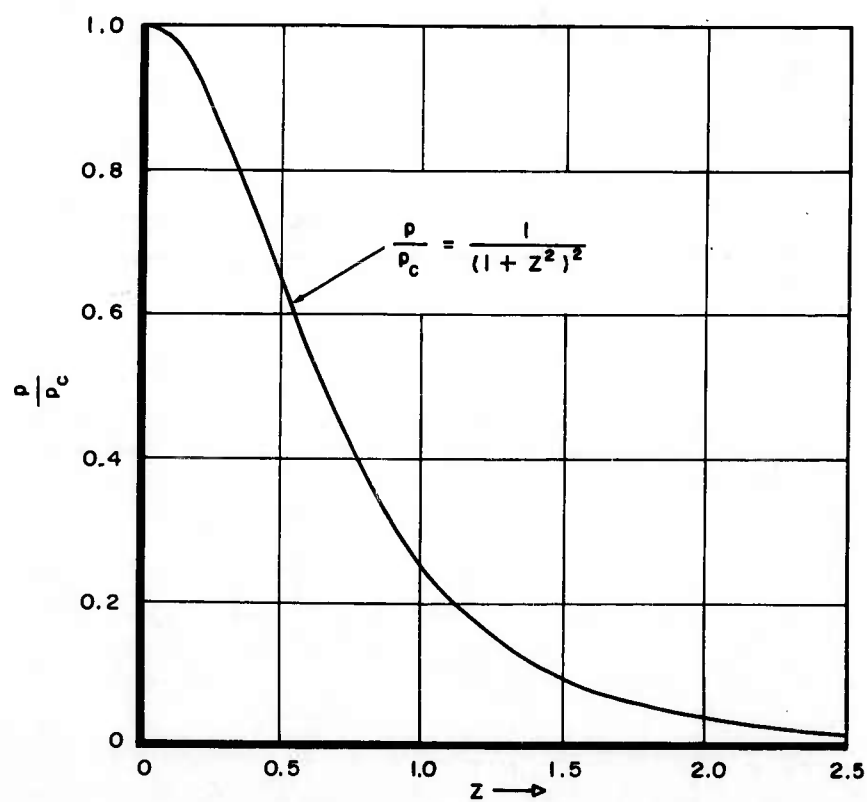
Figure 37. Normalized theoretical pressure distribution assuming $\rho_c = 0$
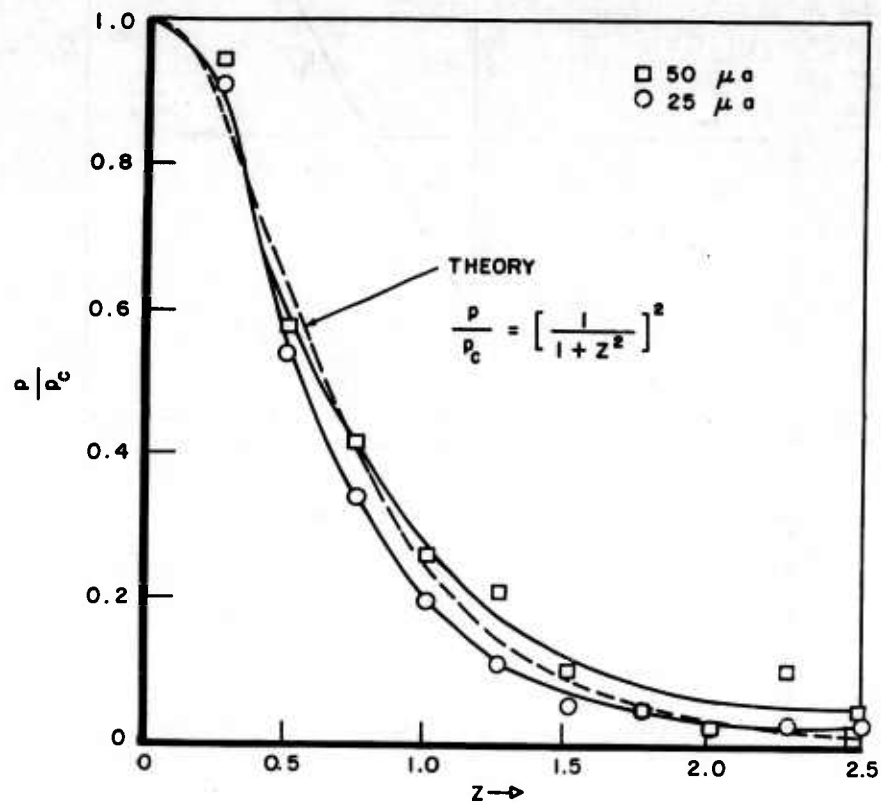
Figure 38. Normalized pressure distribution over the surface of the 7 x 12-inch plate, 0.004-inch wire along the 7-inch dimension, 2 cm from centerline of plate
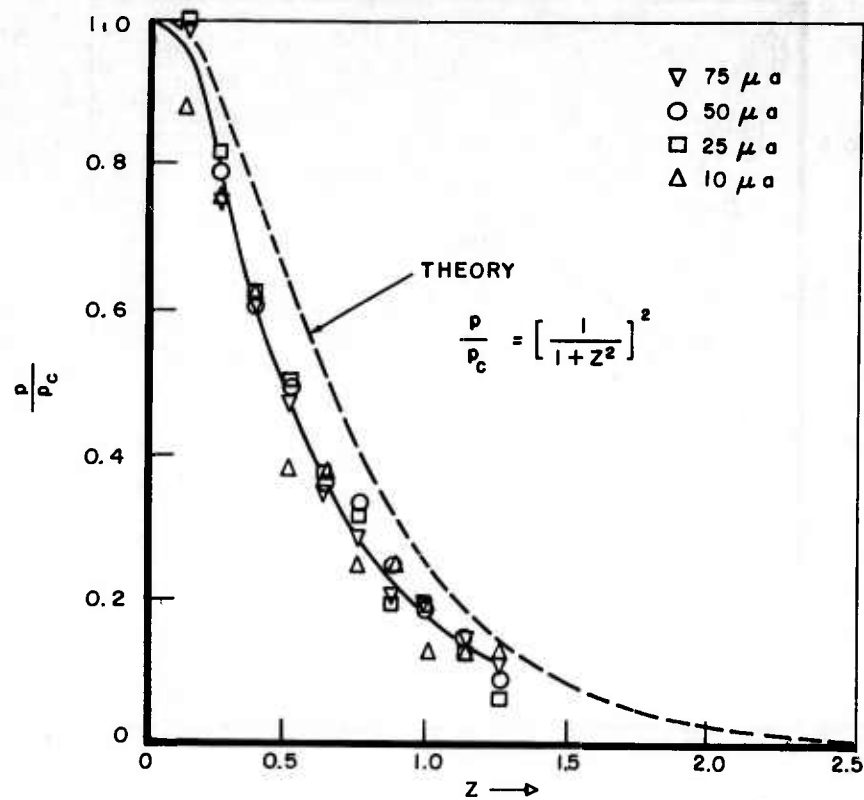
Figure 39. Normalized pressure distribution over the surface of the 7 x 12-inch plate, 0.004-inch wire along the 7-inch dimension, 4 cm from centerline of plate
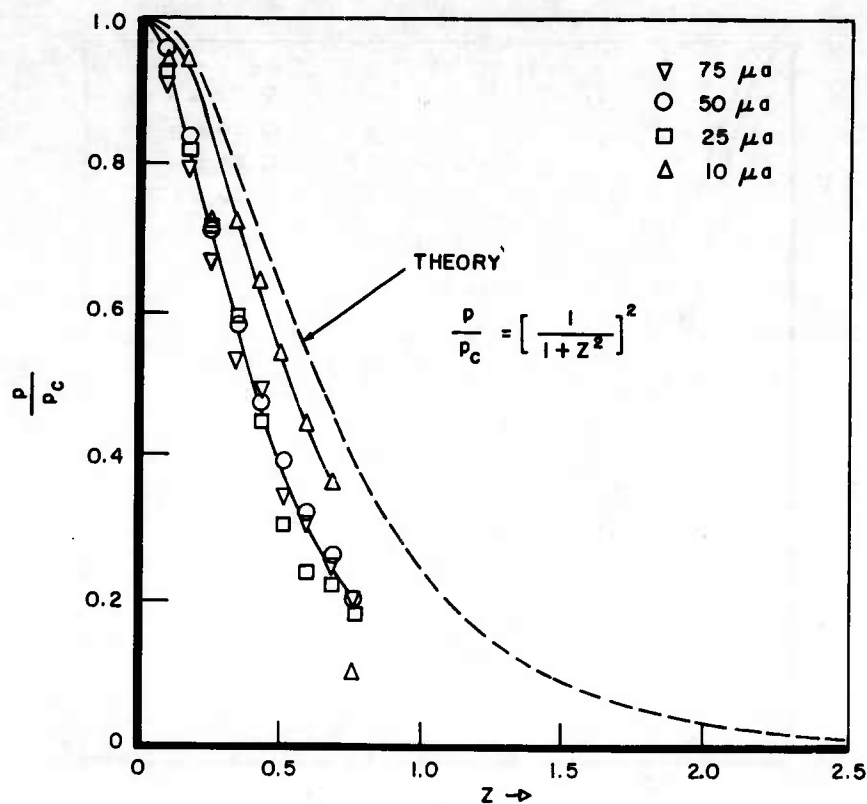
Figure 40. Normalized pressure distribution over the surface of the 7 x 12-inch
plate, 0.004-inch wire along the 7-inch dimension, 6 cm from center-
line of plate
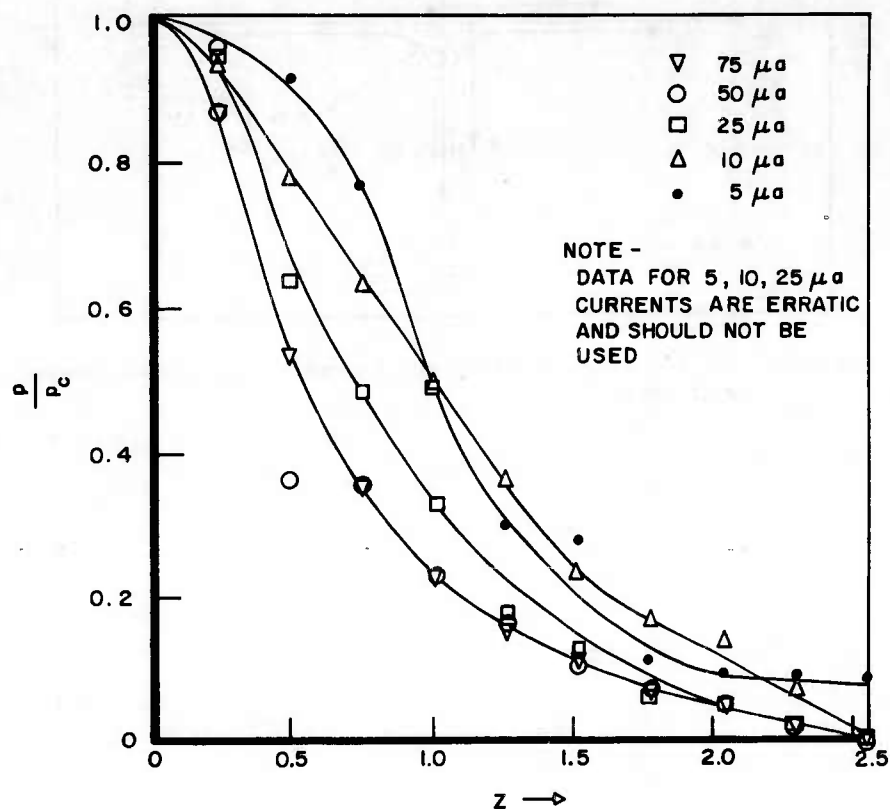
Figure 41. Normalized pressure distribution over the surface of the 7 x 12-inch plate, 0.004-inch wire along 7-inch dimension, 2 cm from centerline of plate. (Data for low currents illustrate erratic behavior due to zero shifts.)
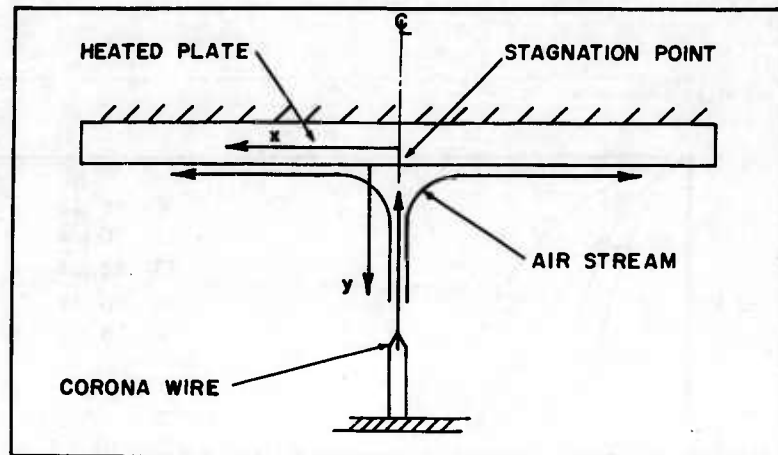
Figure 42. End view of horizontal plate with bottom heated, subjected to corona discharge in air
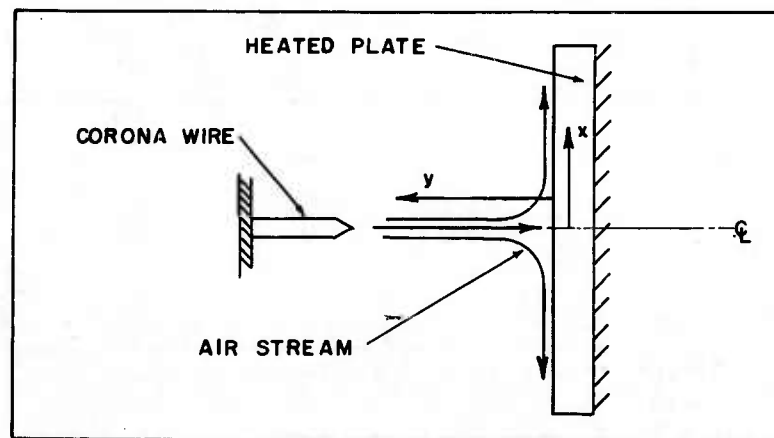
Figure 43. End view of vertical plate with front heated, subjected to corona discharge in air
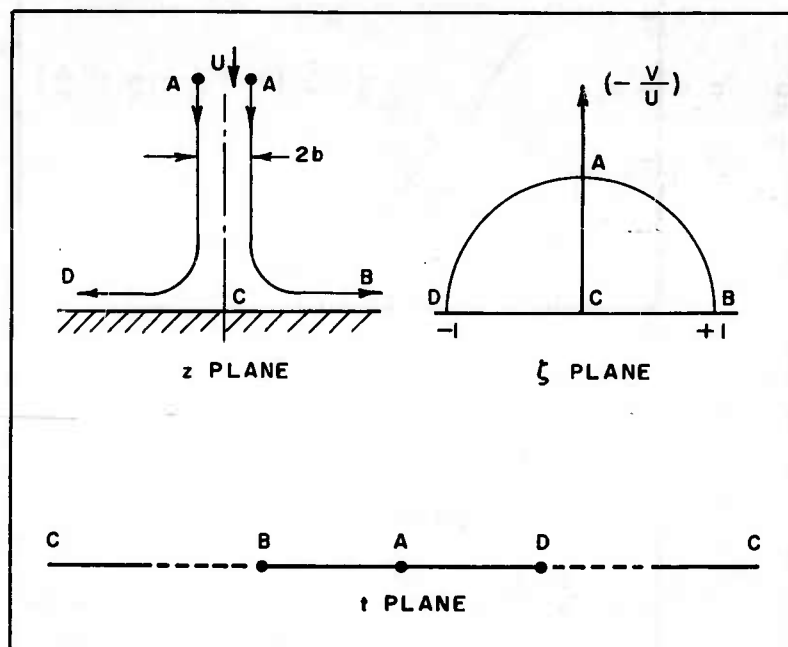
Figure 44. Transformation of the impinging two-dimensional jet shown in the
Z plane
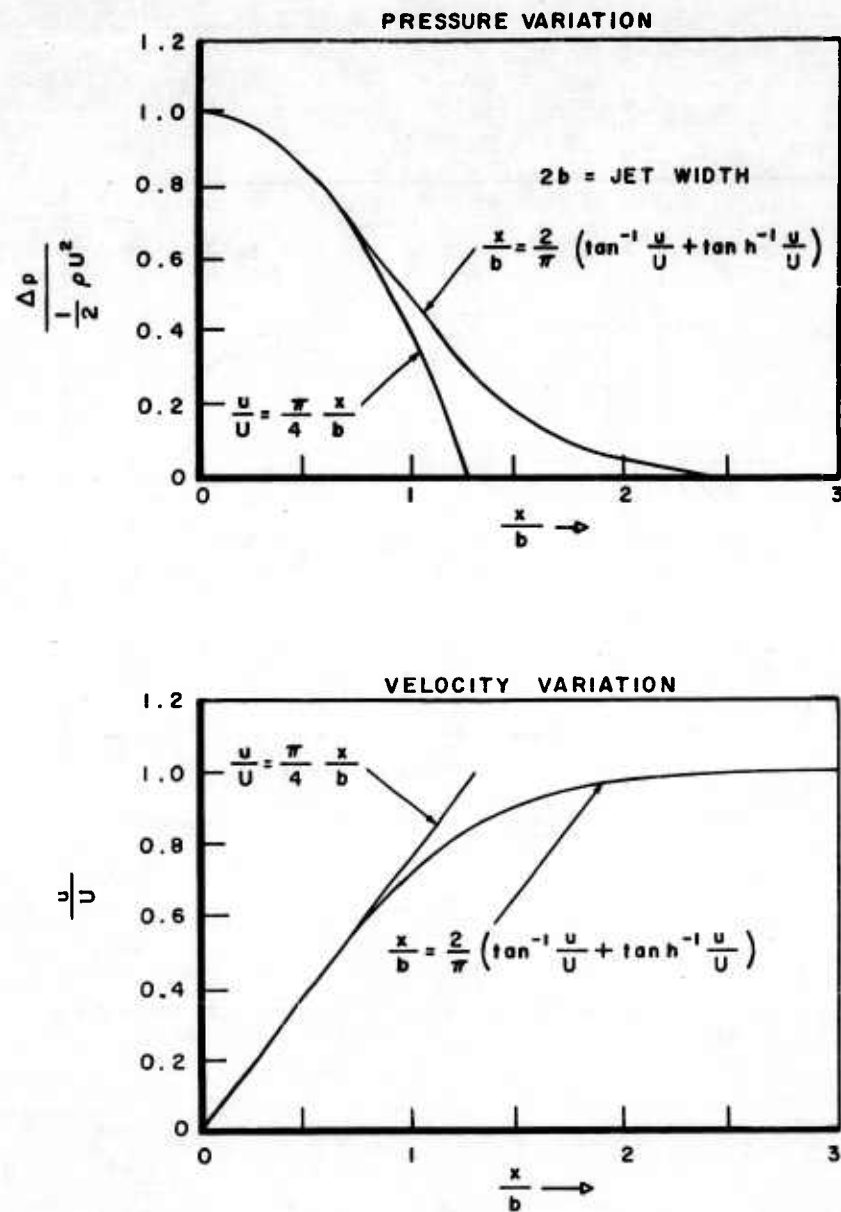
Figure 45. Pressure and velocity distribution at the surface of a plate under narrow ideal jet

94
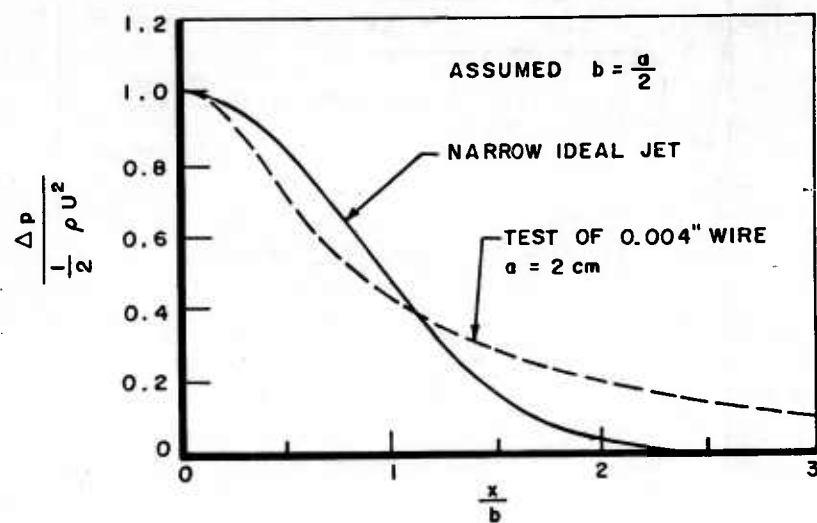
Figure 46. Comparison of the narrow ideal jet pressure distribution with the data of corona discharge from a 0.004-inch wire with 2 cm spacing
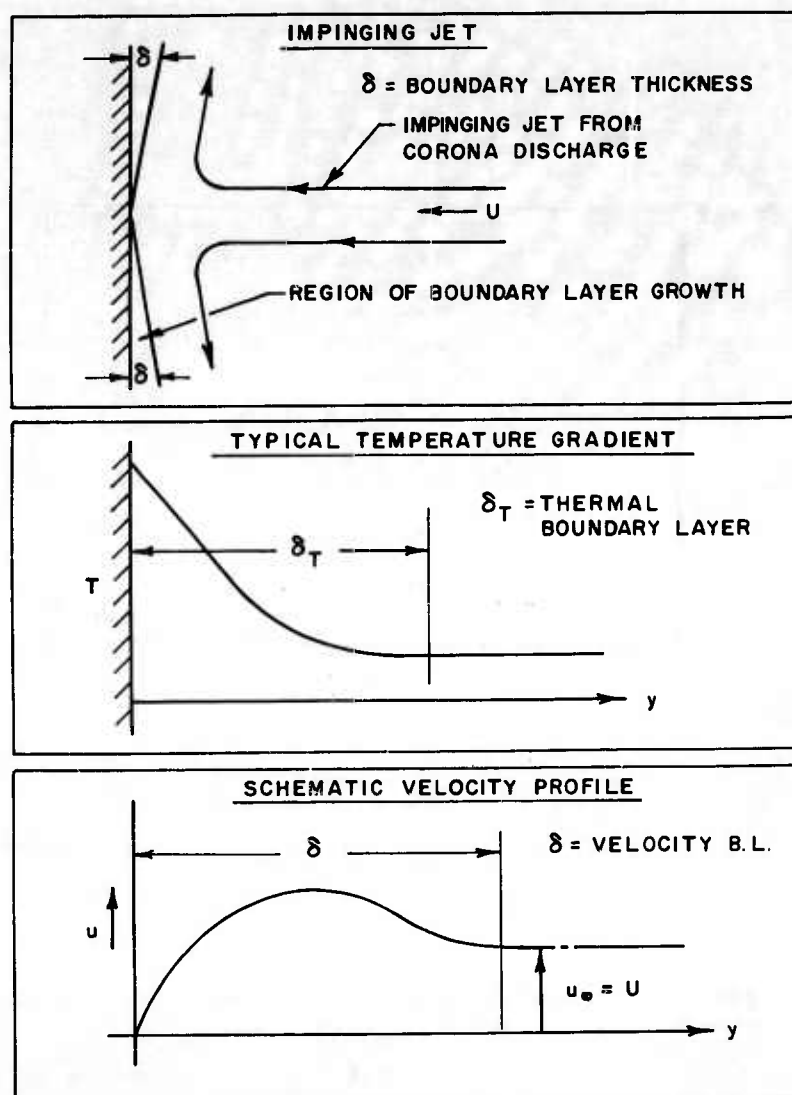
Figure 47. Schematic representations of flow, velocity, and temperature profiles illustrating boundary conditions
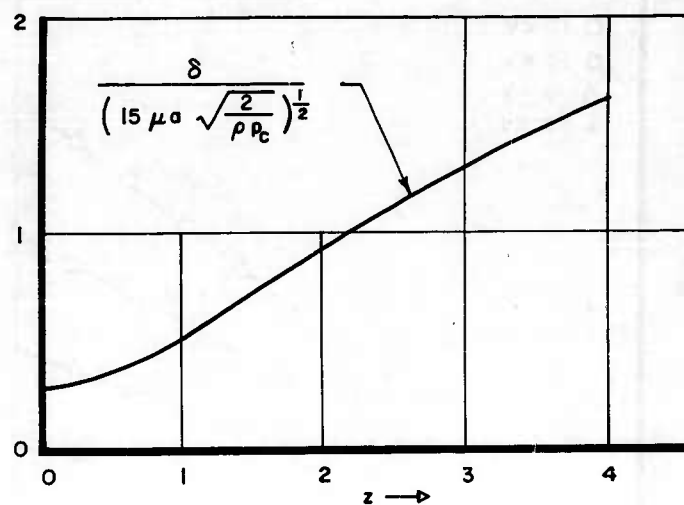
Figure 48. Variation of the theoretical velocity boundary layer thickness for a parabolic velocity profile
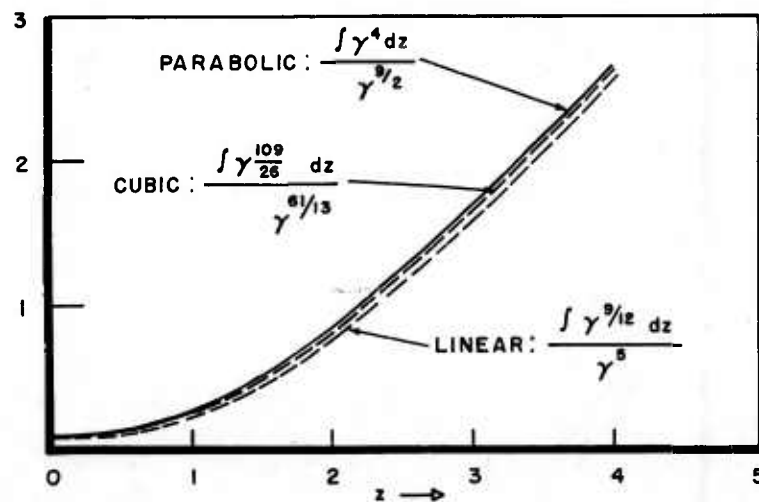
Figure 49. Variation of boundary layer parameters
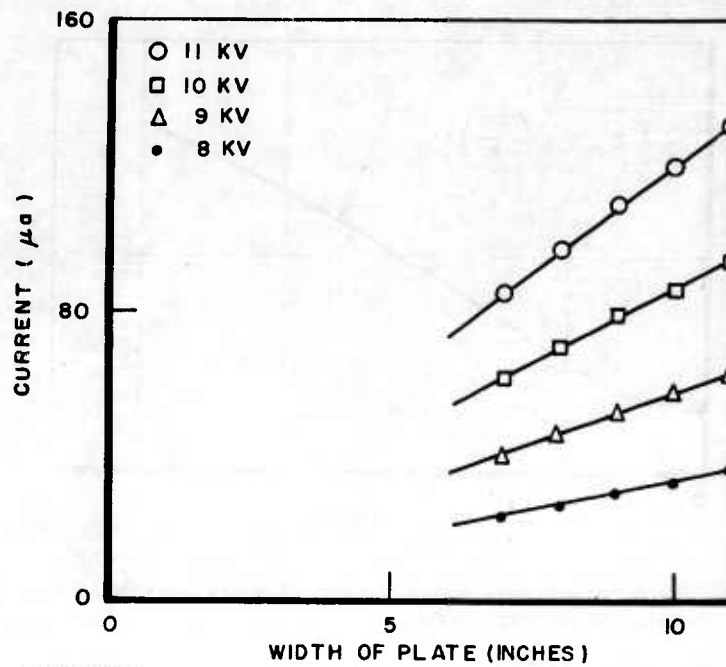
Figure 50. Variation in currents for various pressure plate widths
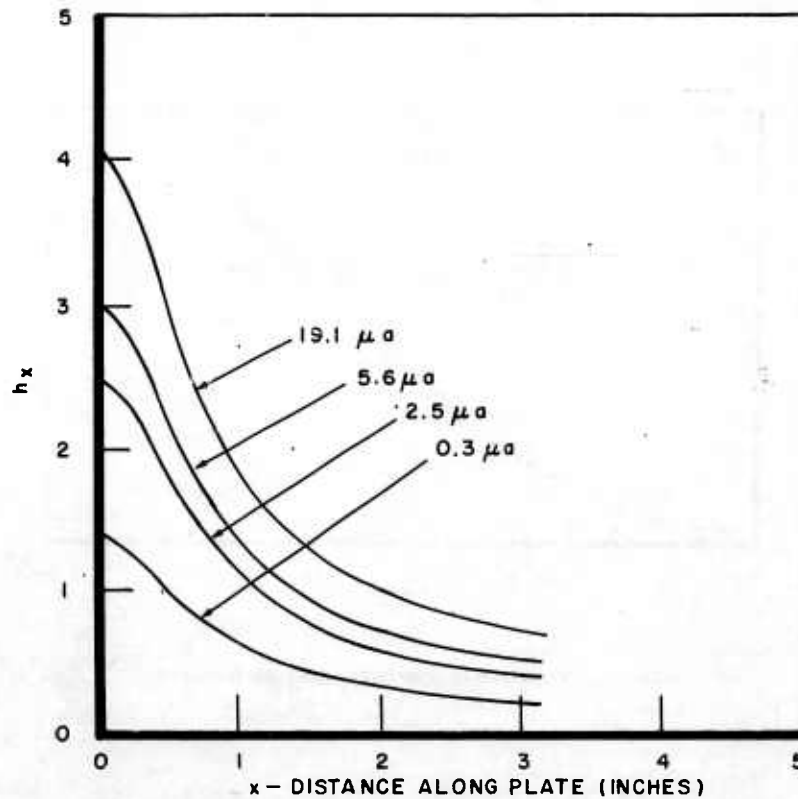
Figure 51. Theoretical variation of heat transfer coefficient, parabolic profile,
a = 2 cm
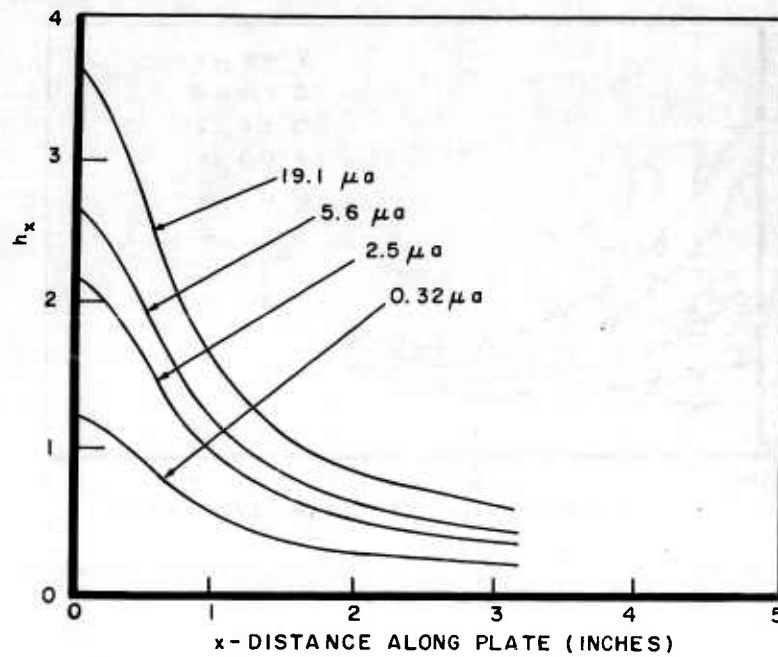
Figure 52. Theoretical variation of heat transfer coefficient, linear profile, a = 2 cm
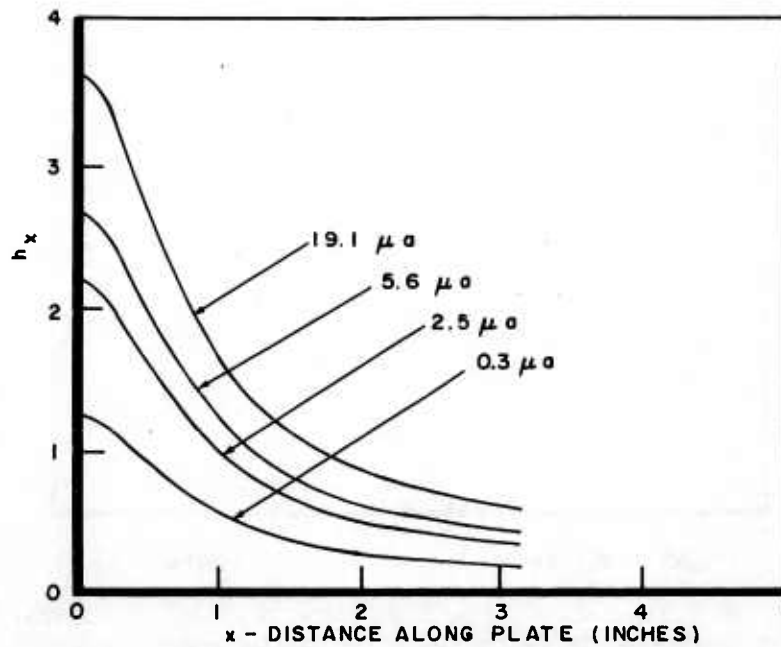
Figure 53. Theoretical variation of heat transfer coefficient, cubic profile, a = 2 cm
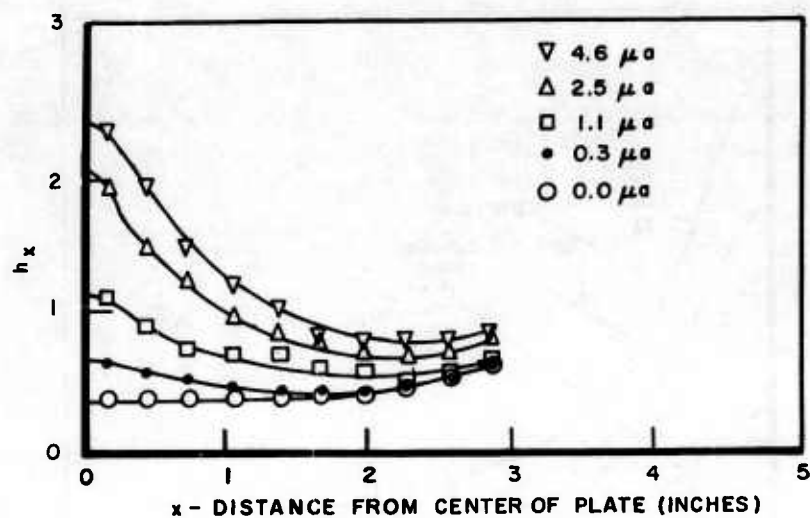
Figure 54. Heat transfer coefficients for horizontal flat heated plate at low currents, a = 2 cm, wire diameter 0.004 inch
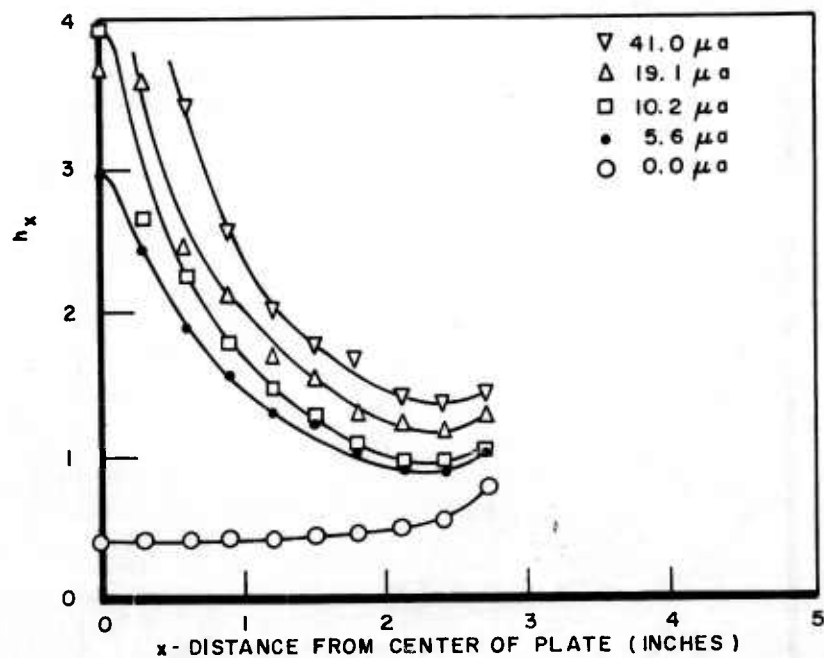
Figure 55. Heat transfer coefficients for horizontal flat heated plate at high currents, a = 2 cm, wire diameter 0.004 inch
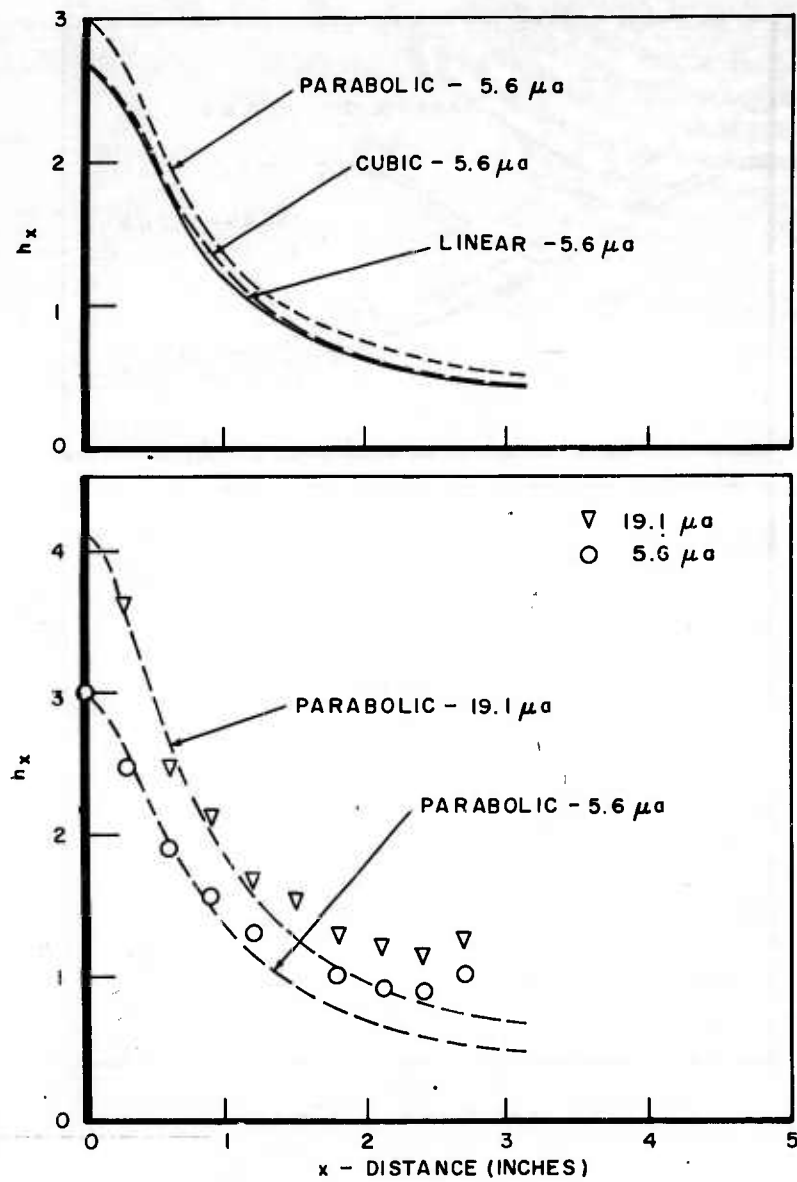
Figure 56. Direct comparison of theory and test data, a = 2 cm,
wire diameter 0.004 inch
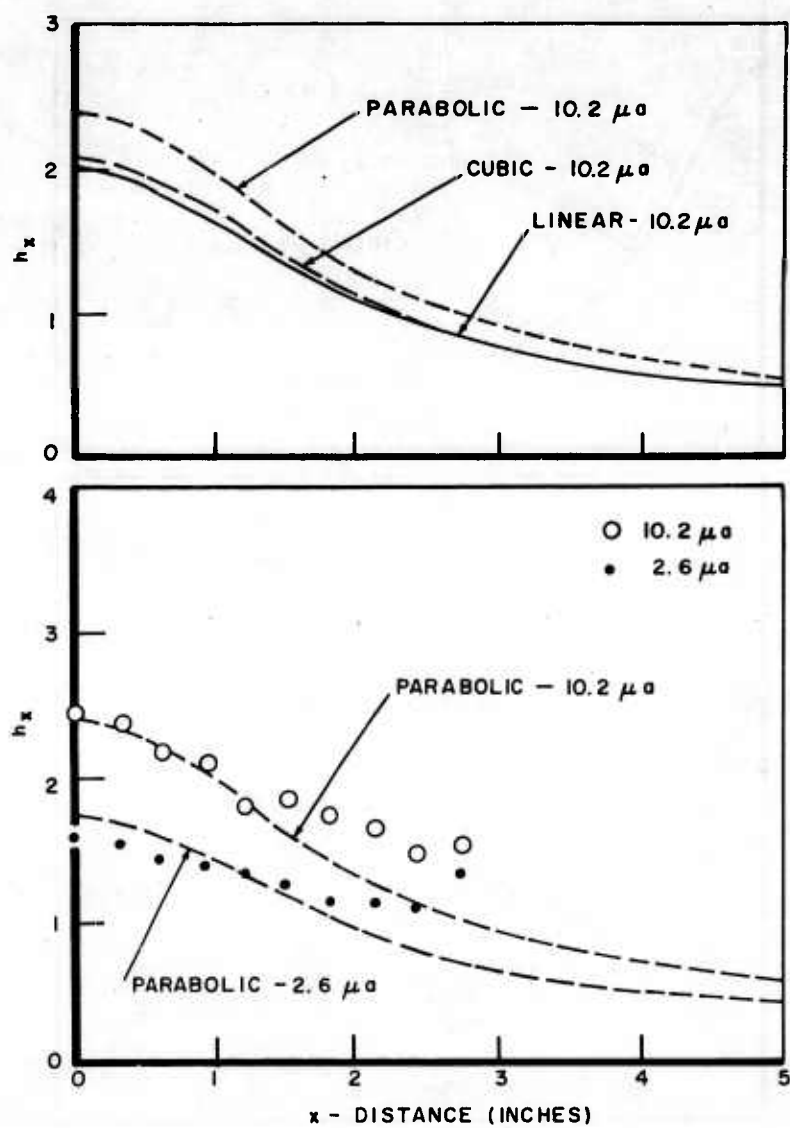
Figure 57. Direct comparison of theory and test data where a = 5 cm,
wire diameter 0.004 inch
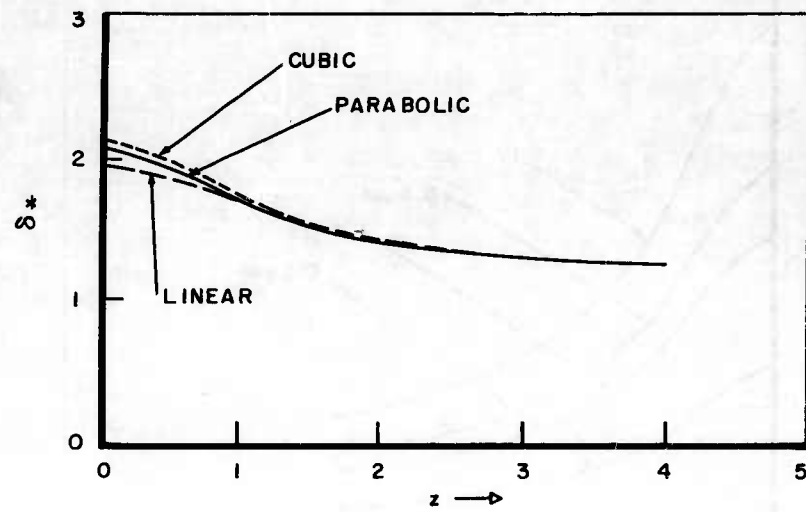
Figure 58. Variations of δ_* for various profiles
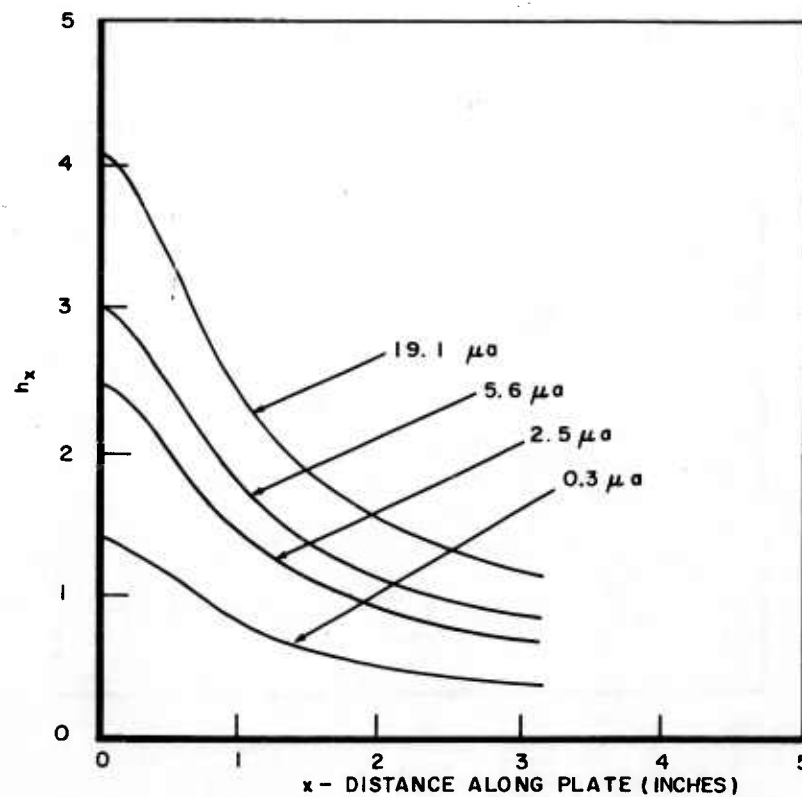
Figure 59. Modified heat transfer coefficients, parabolic profile, a = 2 cm

103
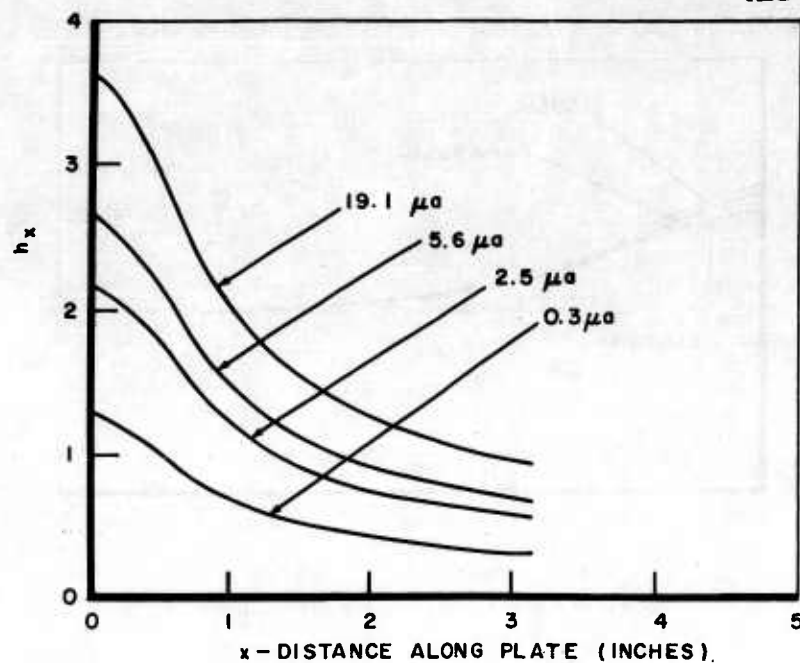
Figure 60. Modified heat transfer coefficients, linear profile, a = 2 cm
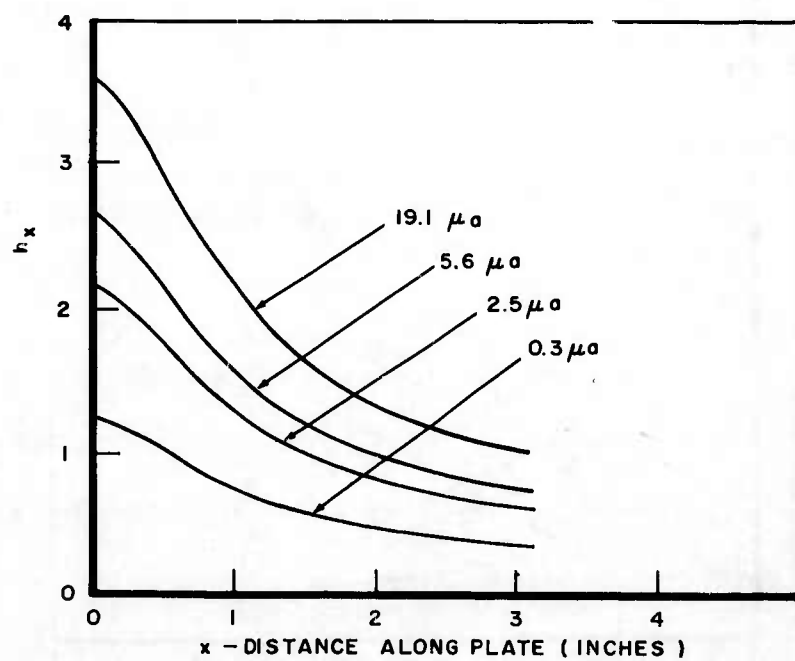
Figure 61. Modified heat transfer coefficients, cubic profile, a = 2 cm
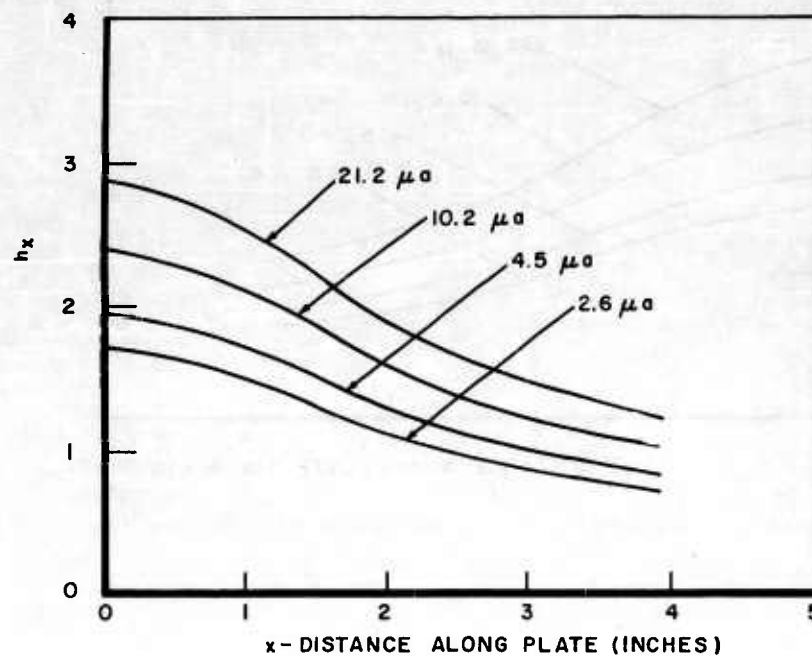
Figure 62. Modified heat transfer coefficient, parabolic profile, a = 5 cm
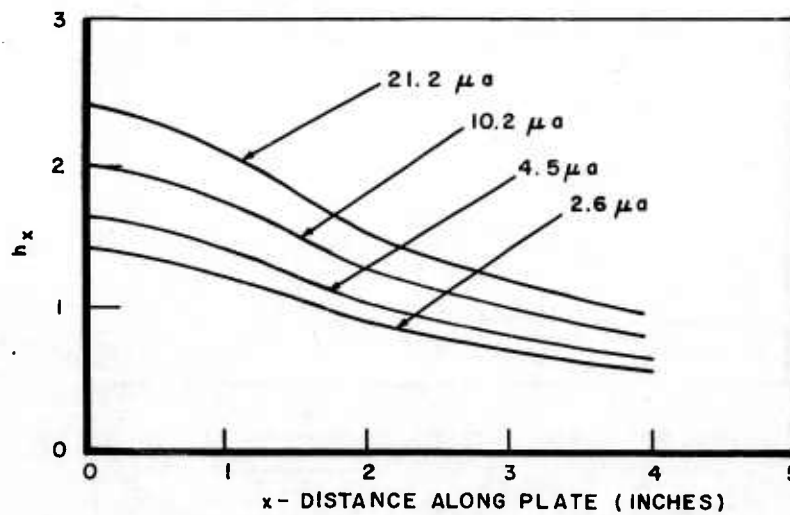
Figure 63. Modified heat transfer coefficients, linear profile, a = 5 cm
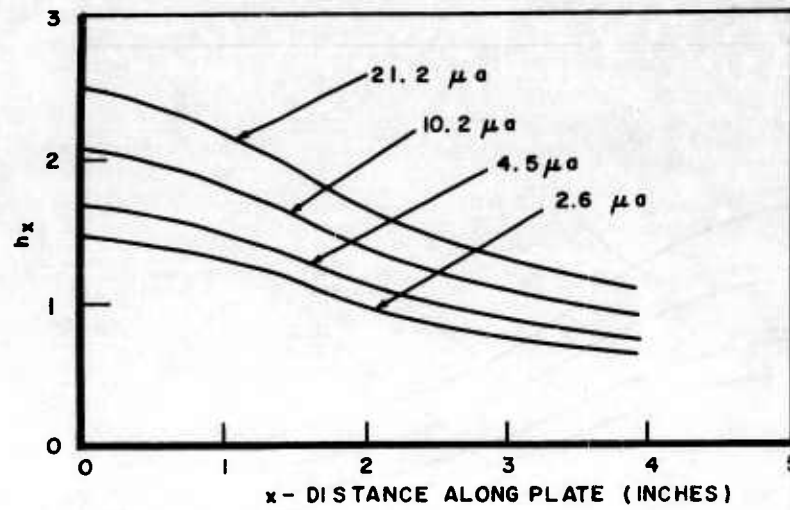
Figure 64. Modified heat transfer coefficients, cubic profile, a = 5 cm
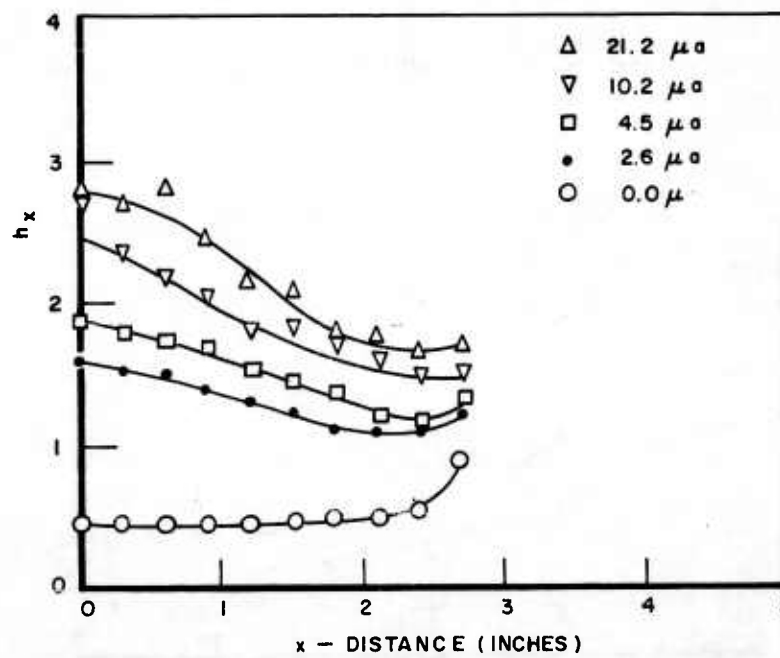
Figure 65. Heat transfer coefficients for horizontal flat heated plate, a = 5 cm, wire diameter 0.004 inch
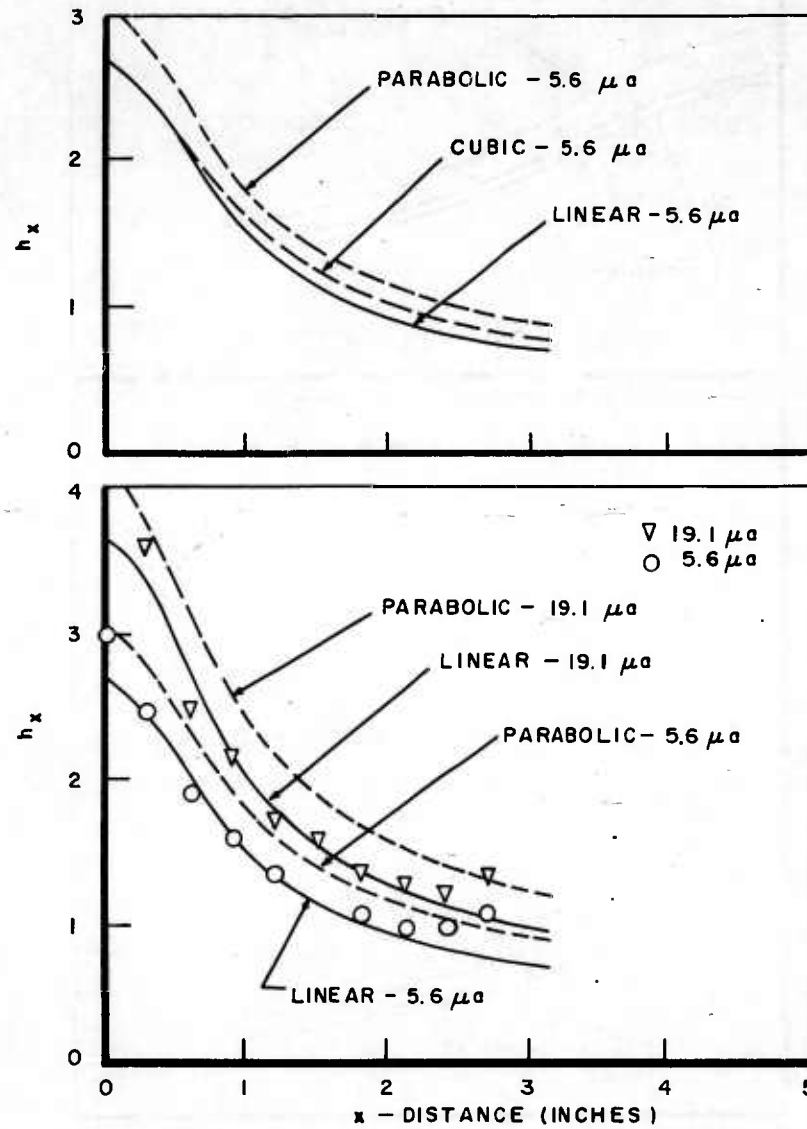
Figure 66. Direct comparison of modified theory with test data for a = 2 cm
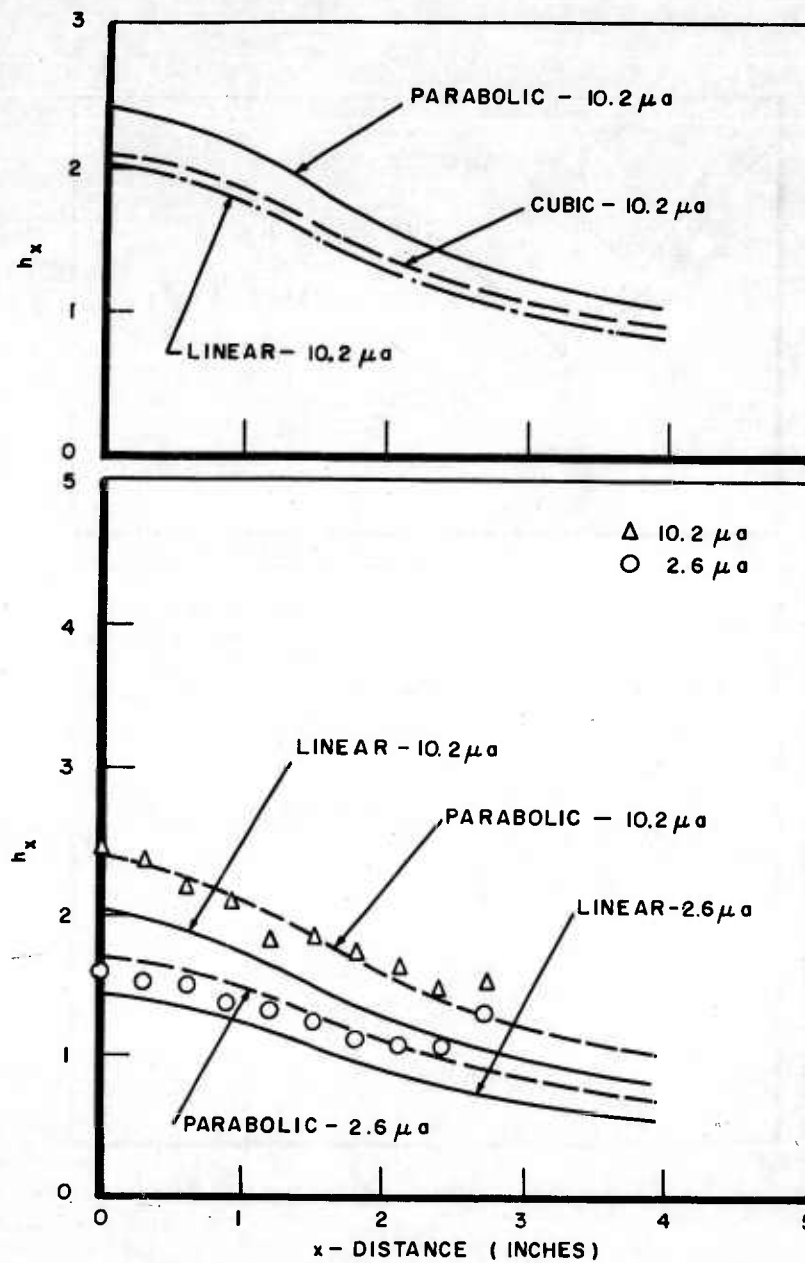
Figure 67. Direct comparison of modified theory with test data for a = 5 cm
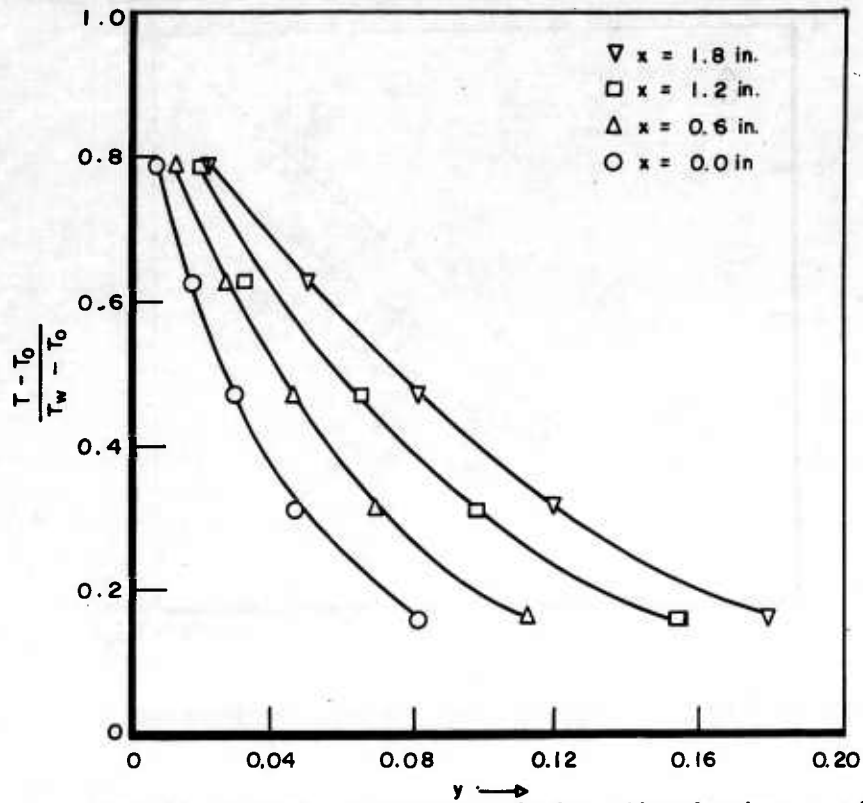
Figure 68. Variation of temperature in the thermal boundary layer on a flat
horizontal plate under influence of corona discharge, a = 2 cm,
current 5.6 microamperes
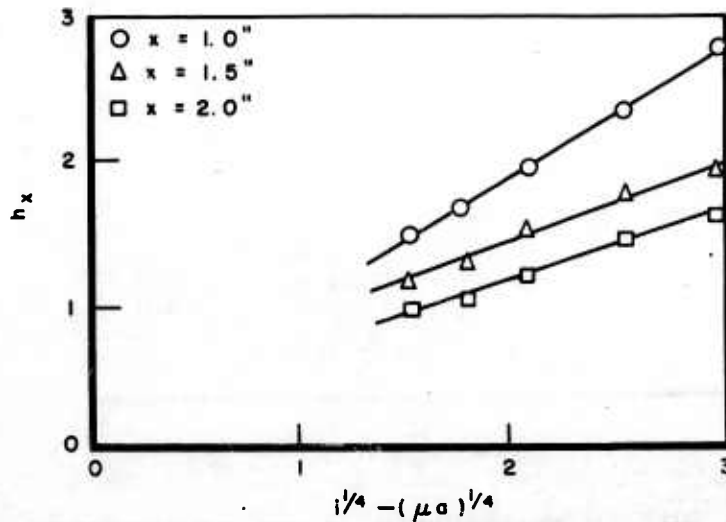
Figure 69. Variation of local heat transfer coefficient with corona current,
a = 2 cm, wire diameter 0.004 inch
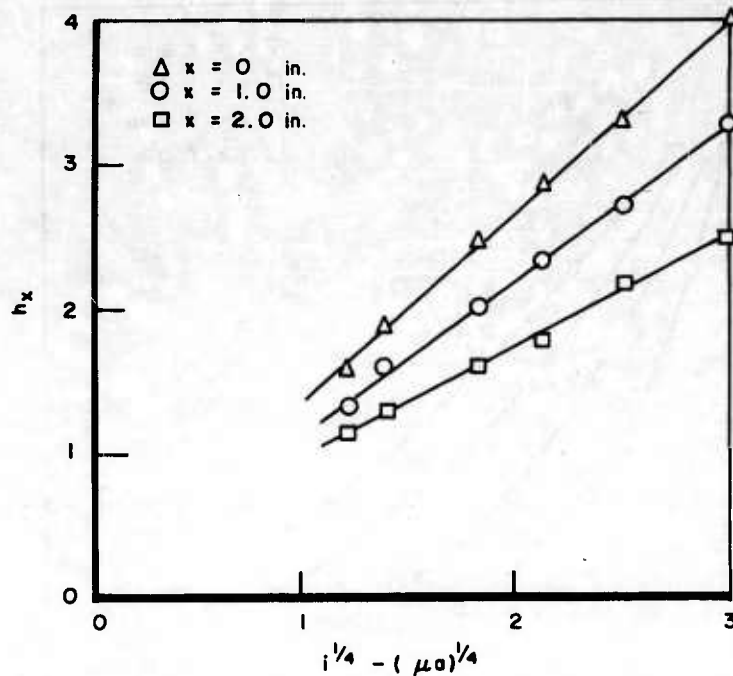
Figure 70. Variation of local heat transfer coefficient with corona current, a = 5 cm, wire diameter 0.004 inch
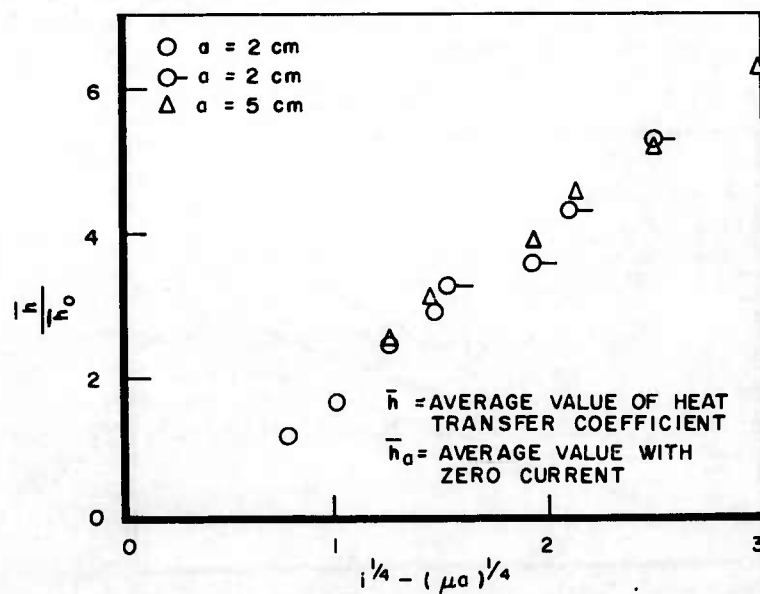
Figure 71. Variation of mean heat transfer coefficient for horizontal plate, 0.004-inch wire
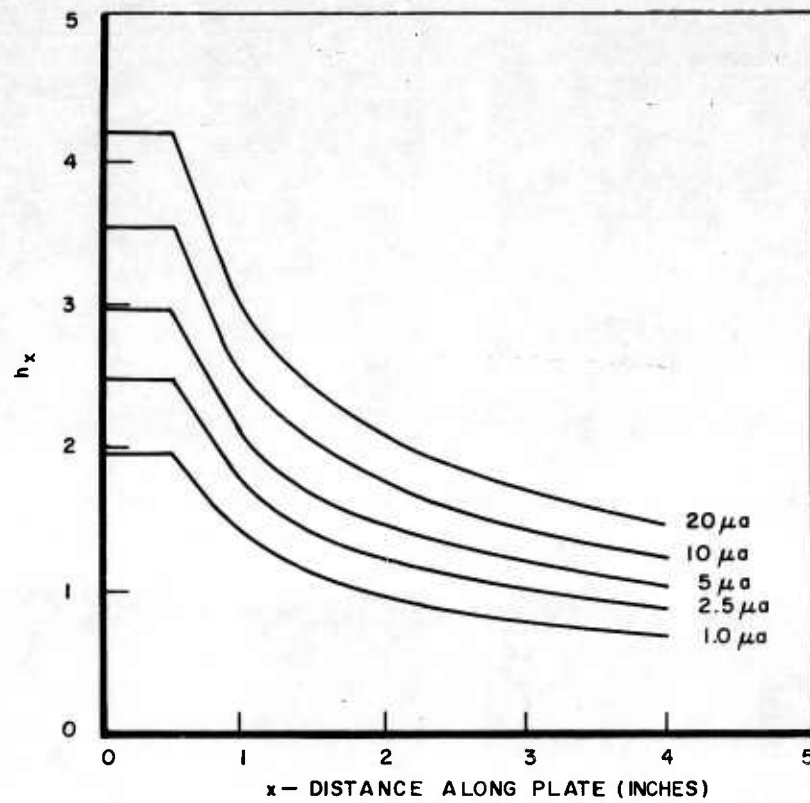
Figure 72. Heat transfer coefficients based upon thin jet solution a = 2 cm
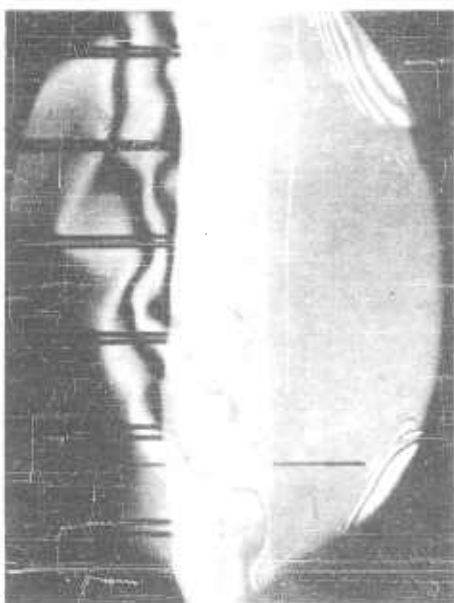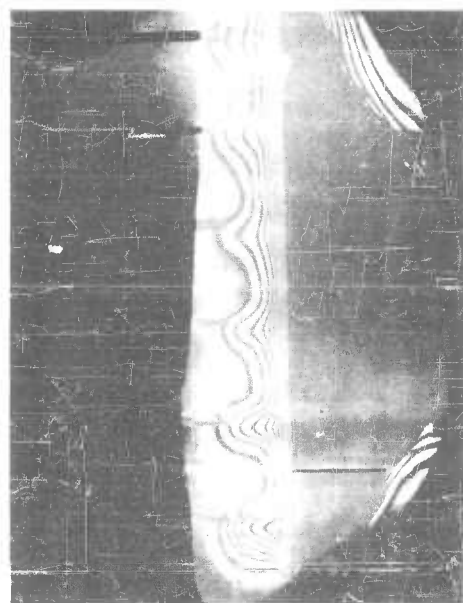
A. Just after field applied   B. Steady state with field
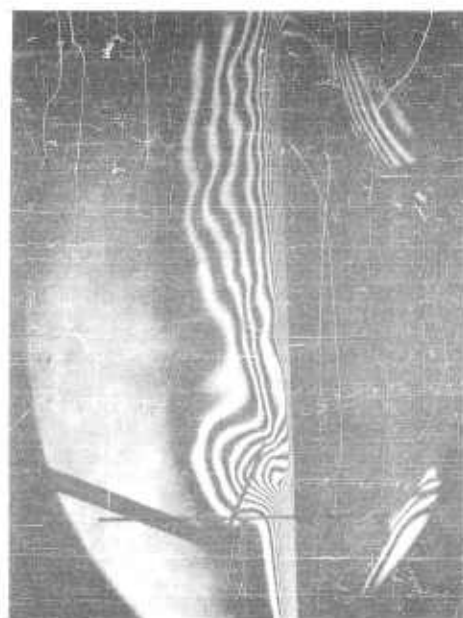
Figure 73. Corona discharge to a heated plate using a row of needles and spark coil
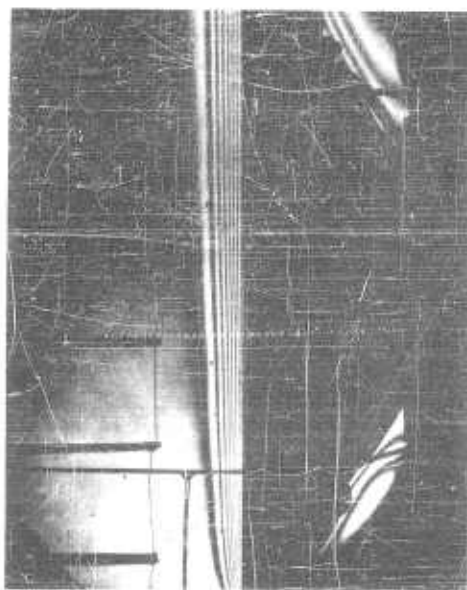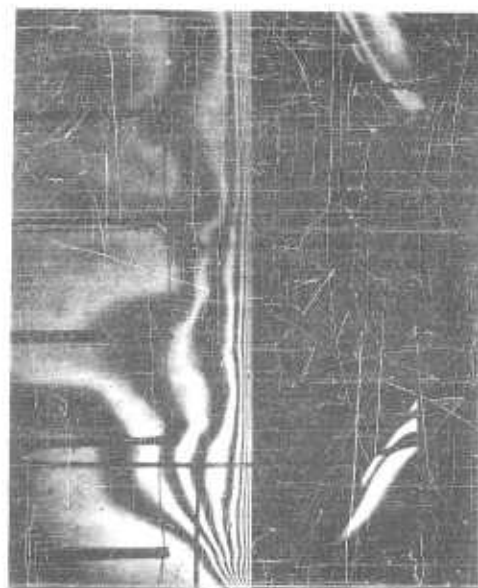

A. Approximately 1 cm spacing   B. Approximately 2 cm spacing

Figure 74. Electrical field applied to a wire grid located in front of the vertical
heated plate using a spark coil

112

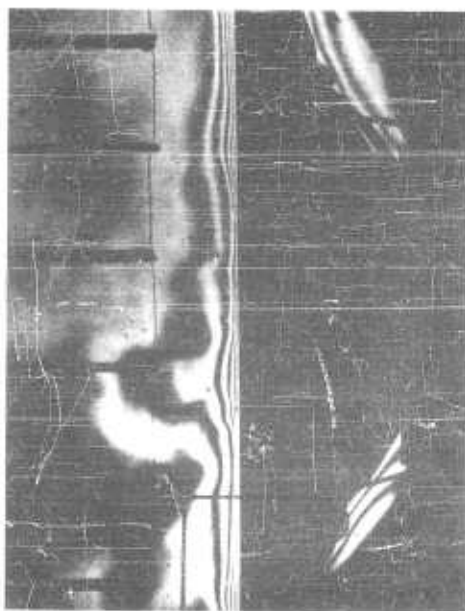A.   0 KV   0 microamps   B.   10.0 KV   4.5 microamps
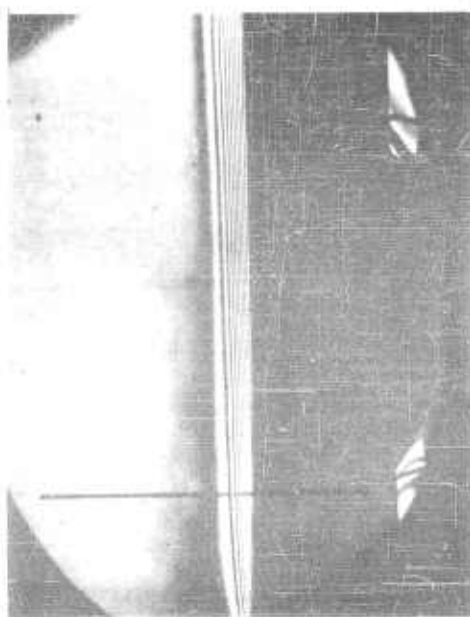
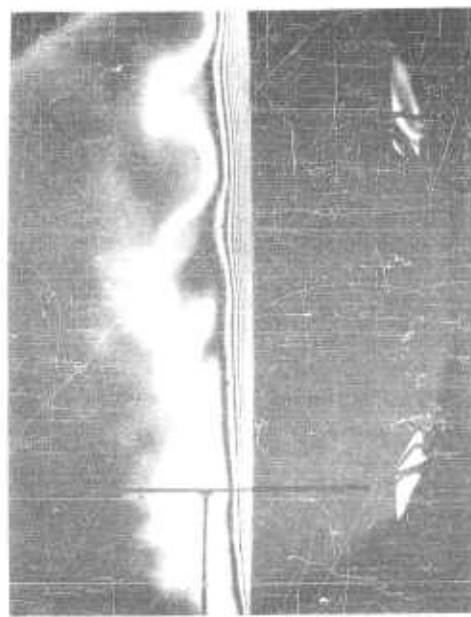C.   10.2 KV   19.8 microamps   D.   12.5 KV   200 microamps

Figure 75.   Interferometer pictures of the effects of corona discharge on heat transfer.
Vertical heated plate, room temperature 52°F, Δ T held constant at 34°F,
0.010-inch wire grid located horizontally at 2 cm from plate, D.C. voltage
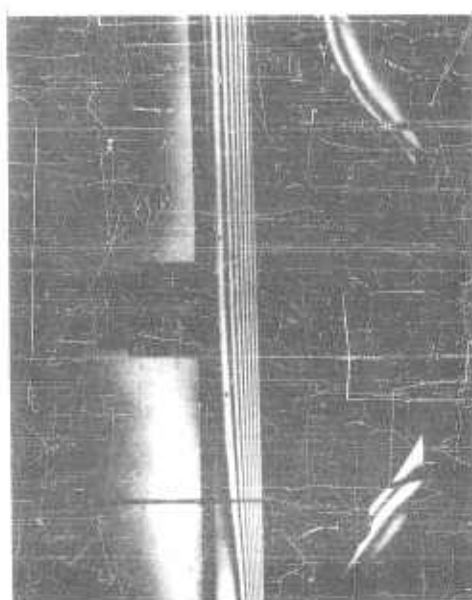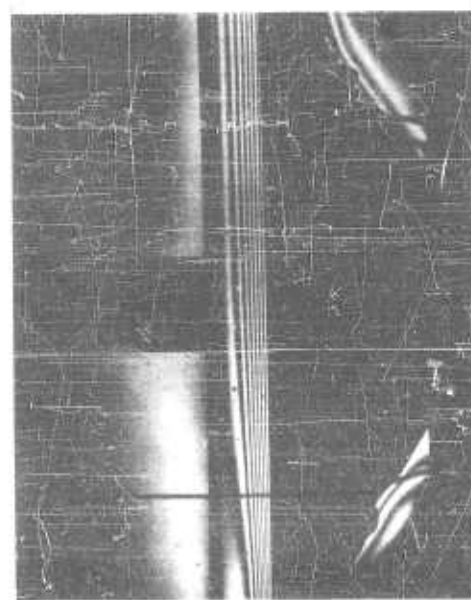applied

A. 0 KV   0 microamps   B. 39.2 KV Current greater than 50 microamps

Figure 76. Interferometer pictures of the effects of corona discharge on heat transfer.
Boundary layer grid glued to vertical heated plate, plate temperature
approximately 100°F, room temperature 54°F, oval positive electrode
1-5/8-inch below bottom edge of heated plate.

A. Zero Voltage   0 microamps   B. 14.7 KV   0 microamps

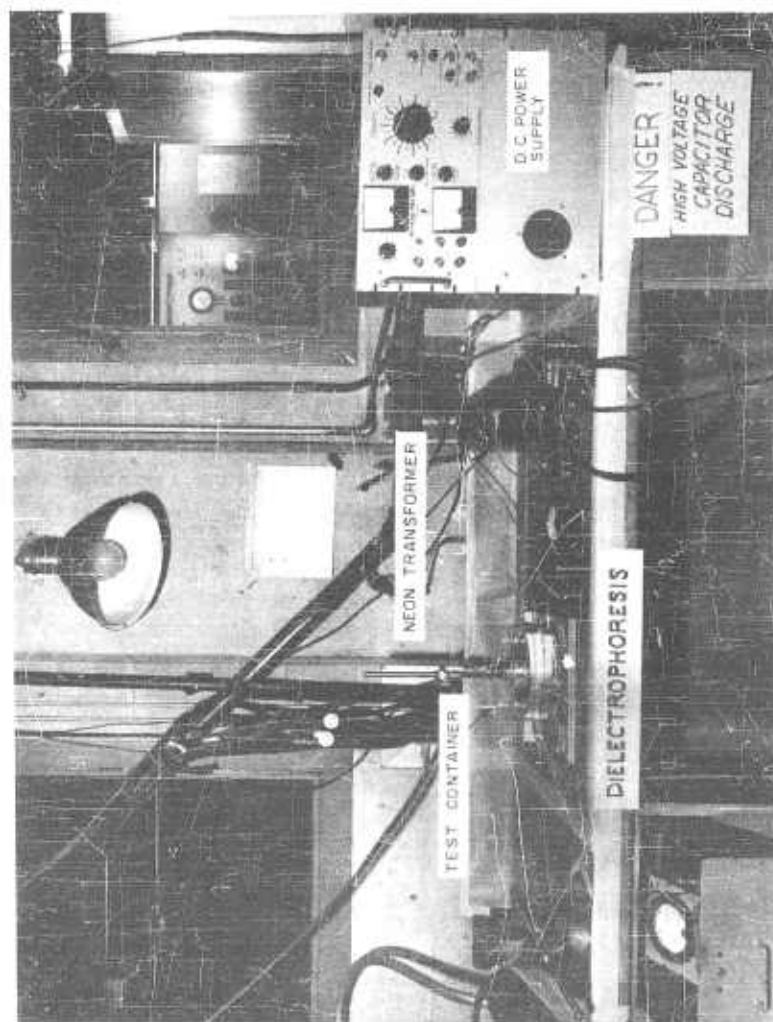Figure 77. Effect of uniform electric field on free convection heat transfer

Figure 78. Over-all view of test set-up for dielectrophoresis experiments
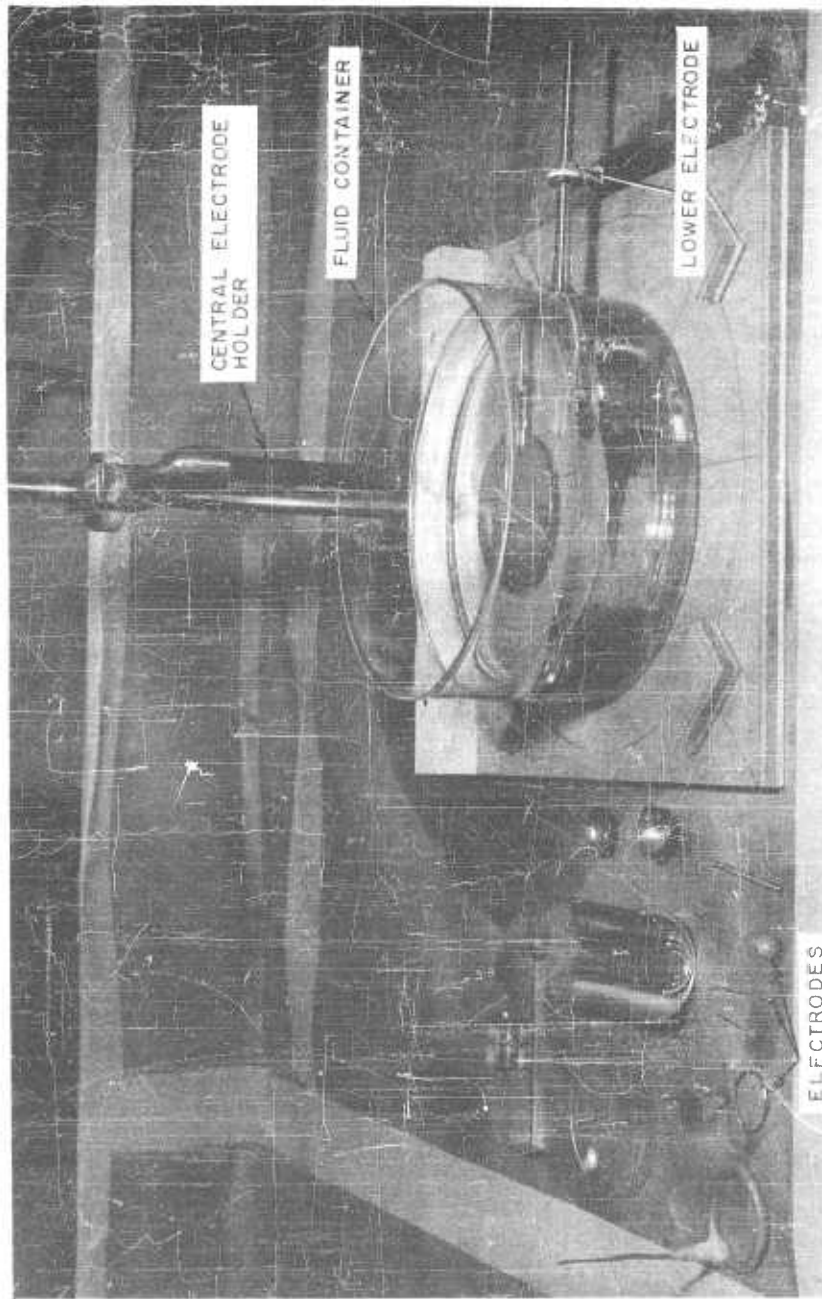
Figure 79. Close up of dielectrophoresis equipment showing electrodes

116
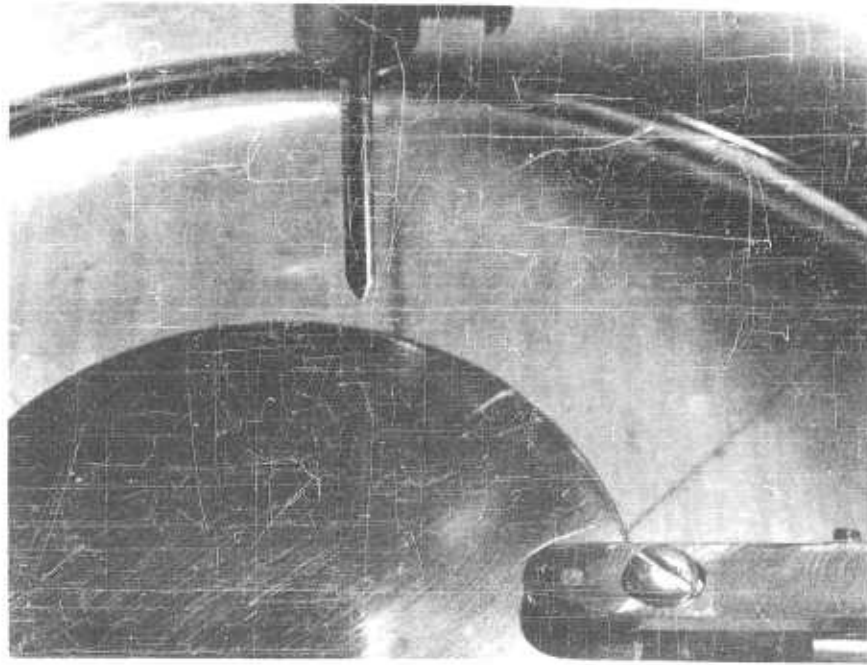
Figure 80. Illustration of electric wind demonstration, no applied field
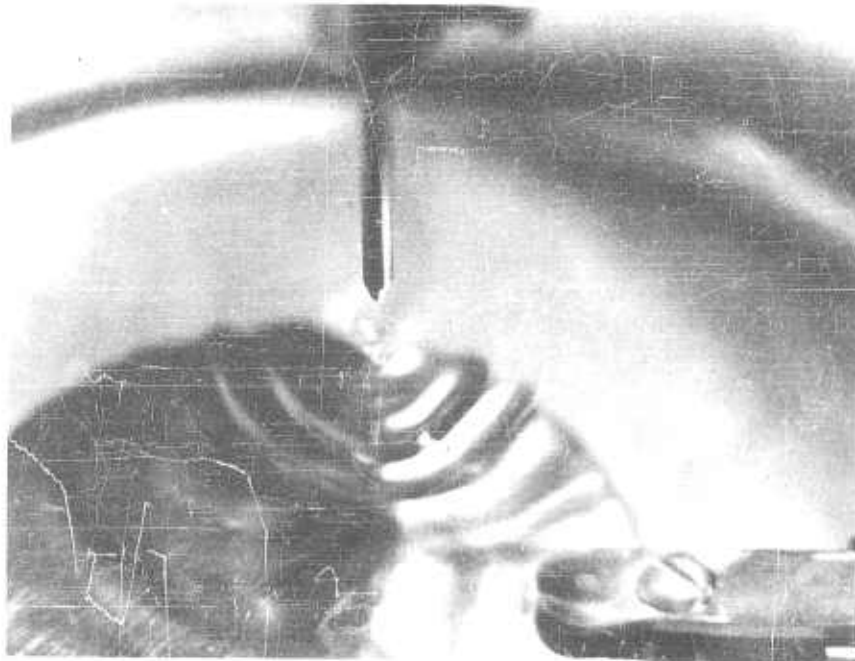
Figure 81. Electric wind test with applied field showing surface waves

Figure 82. Dielectric attraction test, no applied field, sphere located just above liquid surface
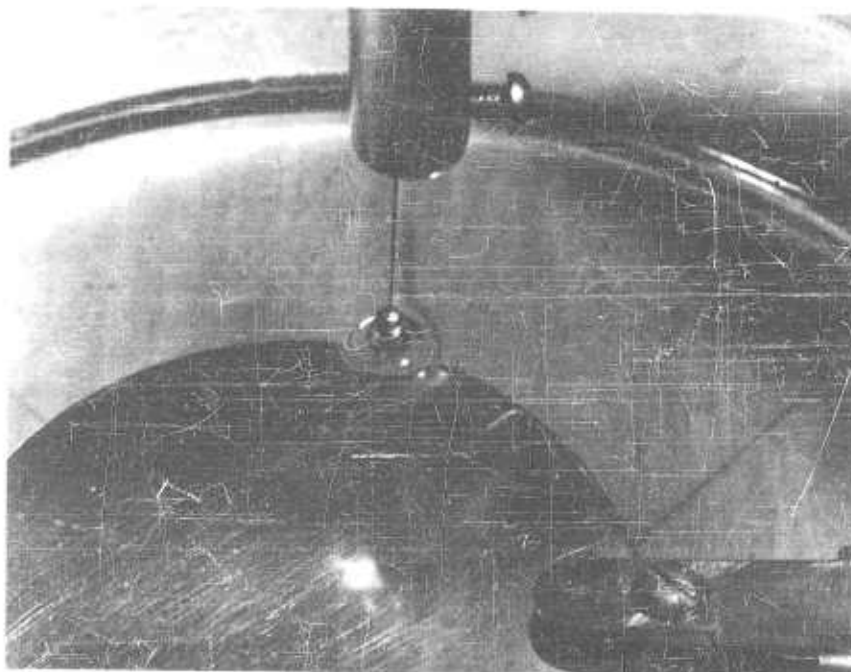
Figure 83. Dielectric attraction test with applied field
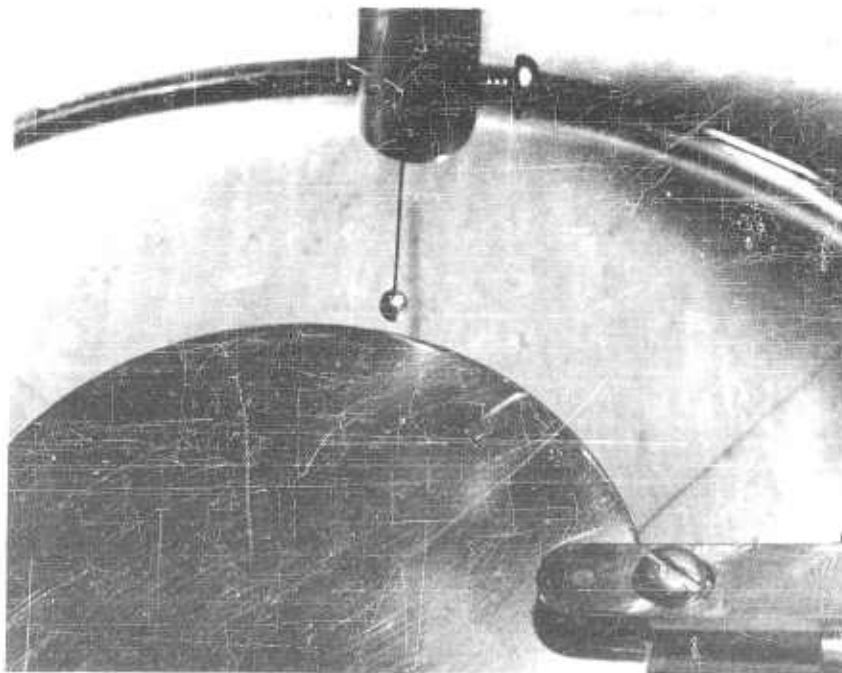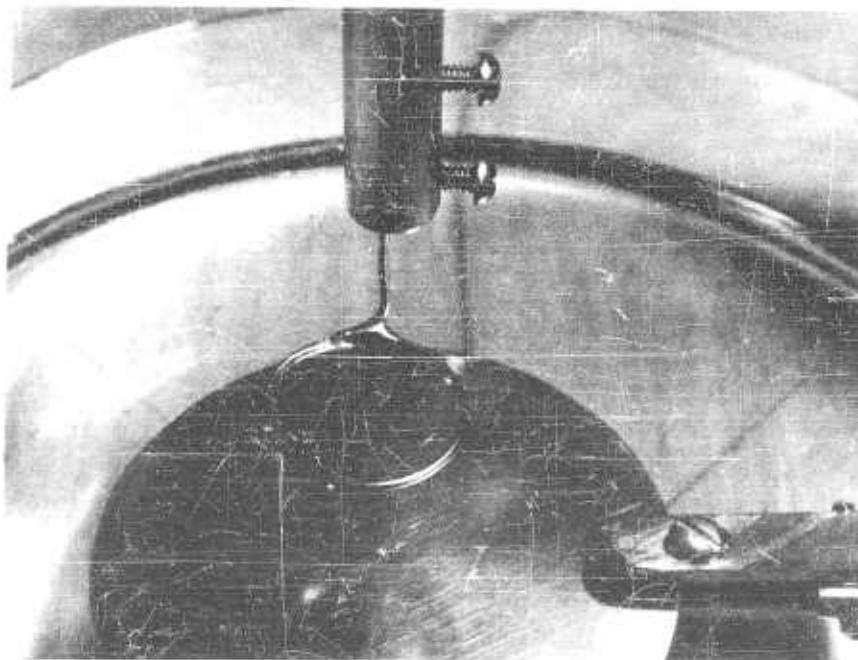
Figure 84. Dielectric attraction test, no applied field, ring electrode just above surface
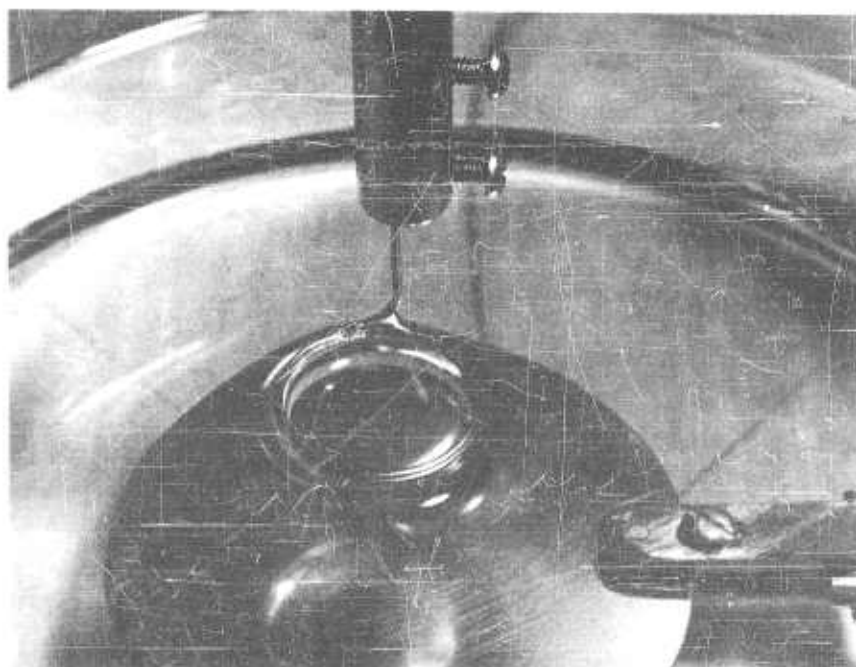

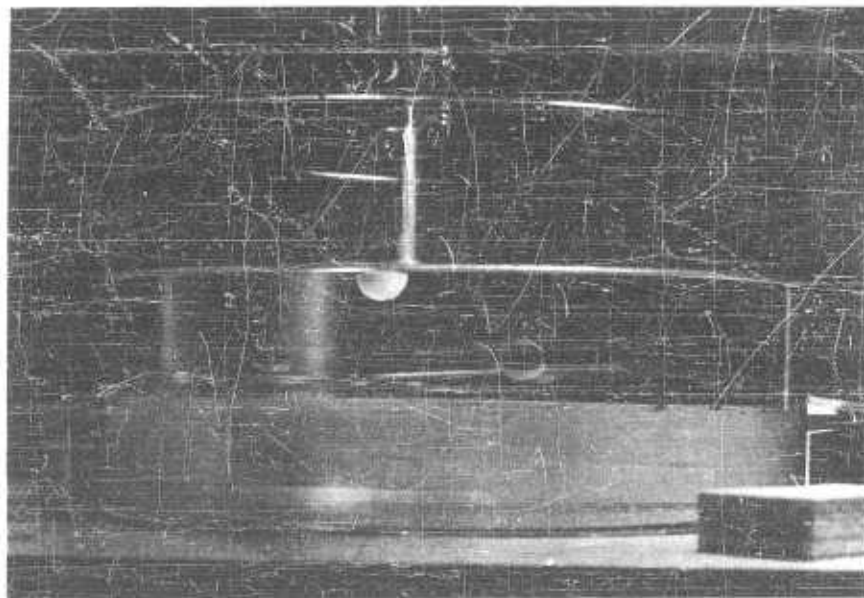Figure 85. Dielectric attraction test with applied field

Figure 86. Dielectric influence on water droplets suspended in a nonconducting
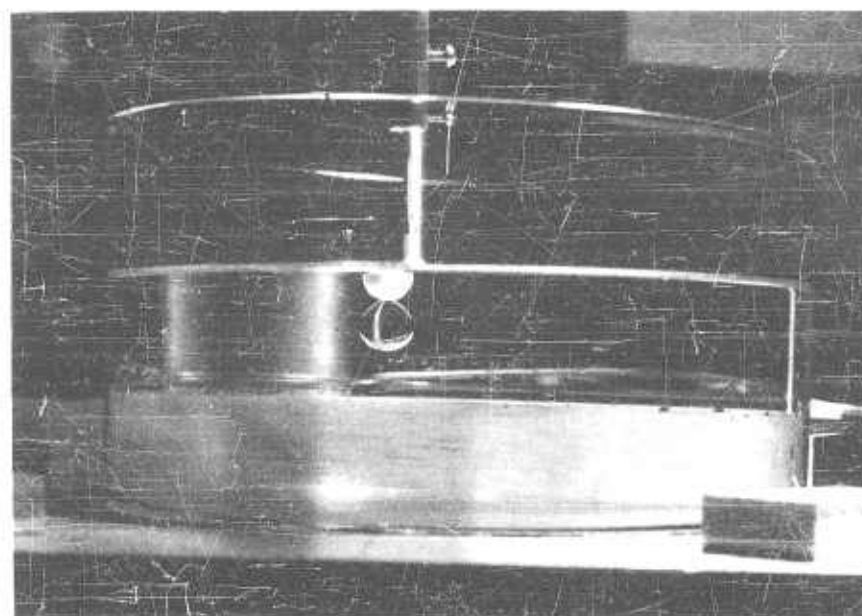liquid, no applied field

Figure 87. Dielectric influence on water droplets suspended in a nonconducting
liquid, after the application of the electric field

REFERENCES

1. Velkoff, H. R., "Electrofluidmechanics: A Study of Electrokinetic Actions in Fluids." ASD-TR-61-642, Aeronautical Systems Division, Air Force Systems Command, WPAFB, Ohio, Feb. 1962

2. Cobine, J. D., Gaseous Conductors, 1st Ed., McGraw-Hill Book Company, New York, N. Y. 1941.

3. Dean, R. C., Jr., Ed., Aerodynamic Measurements, Gas Turbine Laboratory, Massachusetts Institute of Technology, Cambridge, Mass. 1953.

4. Jakob, M., Heat Transfer, Vol I, J. Wiley and Sons, New York, N. Y. 1957.

5. Chattock, A. P., "On the Velocity and Mass of Ions in The Electric Wind in Air," Phil, Mag. Vol. 48. 1899.

6. Harney, J. D., "An Aerodynamic Study of the Electric Wind." Thesis, Calif. Institute of Technology. Pasadena, Calif. (AD-134400) 1957.

7. Stuetzer, O. M., "Ion Drag Pressure Generation." Journal of Applied Physics, Vol. 30. 1959.

8. Robinson, M., "Movement of Air in the Electric Wind of the Corona Discharge," NObs 77164. Index, No. NS-600-010. Technical Paper TP60-2. Research-Cottrell, Inc., Bound Brook, New Jersey. 1960.

9. Schlicting, H., Boundary Layer Theroy. McGraw-Hill Book Company, New York, N. Y. 1955.

10. Goldstein, S., Ed., Modern Developments in Fluid Dynamics, Vol. I & II., Oxford University Press, London. 1938.

11. Rodgers, W. E., Introduction to Electric Fields, McGraw-Hill Book Company, New York, N. Y. 1954.

12. Attwood, S. S., Electric and Magnetic Fields, John Wiley and Sons, New York, N. Y. 1941.

13. Boast, W. B., Principles of Electric and Magnetic Fields, Harper Brothers, New York, N. Y. 1956.

14. Kraus, J. D., Electromagnetics. 1st Ed., McGraw-Hill Book Co., New York, N. Y. 1953.

15. Page, L., and Adams, N. L., Principles of Electricity. 3rd Ed., Van Nostrand, Princeton, N. Y. 1958.

16. Howarth, L., Ed., Modern Developments in Fluid Dynamics. Vol I & II, Clarendon Press, Oxford. 1953.

17. Jakob, M. and Hawkins, G. A., Elements of Heat Transfer, John Wiley and Sons, New York, N. Y. 1957.

REFERENCES (Cont'd)

18. Rouse, H., Ed., Advanced Mechanics of Fluids. John Wiley and Sons. New York, N. Y. 1959.

19. Milne-Thomson, L. M., Theoretical Hydrodynamics. 4th Ed., The Macmillan Company, New York, N. Y. 1960.

20. Sparrow, E. M., Eickhorn, R., and Gregg, J. L., "Combined Forced and Free Convection in a Boundary Layer Flow." The Physics of Fluids, Vol 2, Nr 3. May-June 1959.

21. Sokolnikoff, I. S., and E. S., Higher Mathematics for Engineers and Scientists. 2d Ed., McGraw-Hill Book Co., New York, N. Y. 1941.

22. Gemant, A., Liquid Dielectrics. J. Wiley and Sons, New York, N. Y. 1933.

23. Pohl, H. A., "Some Effects of Non-Uniform Fields on Dielectrics." Rpt No. 48B, Plastics Laboratory, Princeton University, under Contract No. DA-36-039 SC-70154 ONR 356-375. (Journal of Applied Physics, Vol. 29. 1958) 1958.

OTHER BIBLIOGRAPHICAL MATERIAL

Ostrach, S., "An Analysis of Laminar-Free Convection Flow and Heat Transfer About a Flat Plate Parallel to the Direction of the Generating Body Force." NACA TN-2635. Washington, D. C., 1952.

Ostrach, S., "Combined Natural and Forced Convection Laminar Flow and Heat Transfer of Fluids with and without Heat Sources in Channels with Linearly Varying Wall Temperatures." NACA TN 3141, Washington, D.C., 1954.

Von Mises, R. and Friedricks, K. O., "Fluid Dynamics," Notes of Brown University Course in Advanced Instruction and Research in Mechanics. 1941.

Werner, F. D. and Geronime, R. L., "Applications of the Corona Discharge for Measurements of Density and Velocity Transients in Air Flow." Wright Air Development Center TR 53-142. W-PAFB, Ohio. 1953.

APPENDIX I

CALCULATION OF HEAT TRANSFER COEFFICIENTS

The calculation of the heat transfer coefficients from the interferograms is a straight-forward process (Ref. 1)*. It is based upon the fundamental equations of heat transfer and the unique characteristics of the interferometer. Consider the basic heat transfer equations first. In convective heat transfer from a wall, it is assumed that the wall is at rest. It then follows that the heat must pass from the wall through the fluid layer by conduction, and the simple equation of heat conduction can be used.

$$Q = -kA \left. \frac{\partial T}{\partial y} \right|_{y=0}$$

where A is the area through which the heat passes. The defining equation for the heat transfer coefficient is:

$$\dot{Q} = hA(T_w - T_0).$$

Equating these two expressions, one finds:

$$h = -\frac{k}{T_w - T_0} \left. \frac{\partial T}{\partial y} \right|_{y=0}.$$

The value of k is determined at a temperature representative of the fluid layers adjacent to the wall. Following Sparrow (Ref. 2), the reference temperature used in evaluating the fluid properties is

$$T_R = T_w - 0.38(T_w - T_0)$$

The values of the properties of air, including density, viscosity, and Prandtl number were

taken from References 1 and 3. $\left. \frac{\partial T}{\partial y} \right|_{y=0}$ is determined from the interferometer data.

Eckert and Soehngen have derived an equation for the temperature difference between ambient and any fringe in the boundary layer (Ref. 4). A complete tabulation of values of this equation is given by Evalenko (Ref. 1), and these values are reproduced in Table 2. To use the table, it is necessary to know the density, and the number of the fringe being considered. The fringe temperature is then given by

$$T_{Fi} = T_0 \Sigma_{ij} \left(\frac{\lambda_0 \epsilon}{L_c \gamma_0} \right)^j.$$

In order to determine the temperature gradient at the wall, it is necessary to measure the spacing of the fringes precisely. The interferometer pictures were read by means of a Gaertner comparator. This instrument can read distances to within 0.0001 inch. A small "T" is included at the bottom of each photograph to provide a reference length of three inches from which a scale factor could readily be obtained for each photograph. Lines were carefully scribed on the photographs at selected stations along the heated plate.

---

*Numbers in parentheses refer to references for Appendix I.

Table 2

Values of the Properties of Air, $\sum_{ij} \left(\dfrac{\lambda_0 Fi}{LC \, \gamma_0} \right)^j$

F	$\rho = .0710$	Diff	$\rho = .0720$	Diff	$\rho = .0730$	Diff	$\rho = .0740$
1	.00840	12	.00828	11	.00817	12	.00805
2	.01694	25	.01669	23	.01646	22	.01624
3	.02564	38	.02526	36	.02490	34	.02456
4	.03447	51	.03396	48	.03348	47	.03301
5	.04345	64	.04281	60	.04221	60	.04161
6	.05260	79	.05181	74	.05107	71	.05036
7	.06192	95	.06097	87	.06010	85	.05925
8	.07140	111	.07029	100	.06929	100	.06829
9	.08104	126	.07978	115	.07863	115	.07748
10	.09087	139	.08948	135	.08813	128	.08685
11	.10087	159	.09928	147	.09781	144	.09637
12	.11106	178	.10928	162	.10766	162	.10604
13	.12145	197	.11948	179	.11769	178	.11591
14	.13202	216	.12986	195	.12791	196	.12595
15	.14278	233	.14045	215	.13830	213	.13617
16	.15377	254	.15123	233	.14890	233	.14657
17	.16496	276	.16220	252	.15968	250	.15718
18	.17639	298	.17341	272	.17069	273	.16796
19	.18804	323	.18481	291	.18190	292	.17898
20	.19990	344	.19646	315	.19331	312	.19019
21	.21201	367	.20834	339	.20495	332	.20163
22	.22437	396	.22041	357	.21684	358	.21316
23	.23699	421	.23278	382	.22896	382	.22514
24	.24987	448	.24539	409	.24130	406	.23724
25	.26303	474	.25828	437	.25391	431	.24960
26	.27645	506	.27139	461	.26678	456	.26222
27	.29018	539	.28479	488	.27991	484	.27507
28	.30418	569	.29849	516	.29333	513	.28820
29	.31852	605	.31247	547	.30700	541	.30159
30	.33317	640	.32677	576	.32101	574	.31527
31	.34813	672	.34141	612	.33529	605	.32924
32	.36344	712	.35632	642	.34990	641	.34349
33	.37908	747	.37161	678	.36483	676	.35807

F   is the fringe number

ρ is the density of the air based upon T_R

Distance readings were made for all fringes at a given station, and corrected by applying the scale factor for that photograph. Knowing the temperature of each fringe and its spacing, it is then possible to plot the temperature profiles. From the temperature profiles, the slope at the wall was determined for several typical cases. For the same cases the slopes based upon the inner two fringes were determined and compared with the slopes based upon the plotted temperature profiles. Since the two slopes agreed quite well, the determination of the remaining temperature gradients was based upon the slopes determined by the temperatures and spacings of the inner two fringes.

APPENDIX I - REFERENCES

1. Evalenko, W. A., "Free Convection Heat Transfer on a Vertical Plate under Conditions of Non-Uniform Surface Temperature." Thesis, GAE-4 Air Force Institute of Technology, Wright-Patterson Air Force Base, Ohio. 1957.

2. Sparrow, E. M., "Laminar Free Convection on a Vertical Plate with Prescribed Non-Uniform Wall Heat Flux or Prescribed Non-Uniform Wall Temperature." NACA TN 3508, Washington, D. C. 1955.

3. Jakob, M. and Hawkins, G. A., Elements of Heat Transfer, John Wiley and Sons, New York, N. Y. 1957.

4. Eckert, E. R. G. and Soehngen, E. E., "Studies on Heat Transfer in Laminar Free Convection with the Zehnder-Mach Interferometer." AFTR 5747. Wright-Patterson Air Force Base, Ohio. 1948.

APPENDIX II

LIST OF EQUIPMENT USED

The nomenclature for the equipment used in the experimental phase is listed in this section.

1. High voltage D.C. power supply

   Type: D. C. power supply
   Rating: 0-2 ma
         0-50 KV
   Make: Sterling Instruments Co., Detroit, Michigan
   Model: PS-50

2. Microammeter

   Type: Illuminated Spot microammeter
   Rating: 0-1-3-10-100-300-1000 ua
   Make: Greibach Instruments Corp., New Rochelle, N. Y.
   Model: Number 500

3. High Voltage Voltmeter

   Type: Electrostatic voltmeter, double pivoted moving vane
   Rating: 0-10-20-30-40 KV
   Make: Sensitive Research Instruments Corp., New Rochelle, N. Y.
   Model: ESH

4. High Voltage Voltmeter

   Type: Vacuum tube voltmeter plus high voltage probe
   Rating: 0-50 KV
   Make: Radio Corporation of America, Harrison, N. J.
   Model: WV-97A and WG-289 High Voltage Probe

5. Thermocouple Potentiometer

   Type: Portable precision potentiometer
   Make: Rubicon Instruments Div., Minneapolis-Honeywell Regulator Co., Minneapolis, Minn.

6. Inclined Manometer

    Type: 40 tube band with reservoir
    Make: Ann Arbor Instrument Works, Ann Arbor, Michigan
    Specific gravity of fluid .956

7. Micromanometer

    Type: Chattock two fluid micromanometer (Kerosene and water)
    Make: Frank G. Wahlen, Chicago, Ill.

8. Traversing Microscope

    Type: micrometer traverse - Range 0-4″ traverse
    Make: Gaertner Scientific Corp., Chicago, Ill.
    Model: Gaertner Comparator

Aeronautical Systems Division, Dir/Aeromechanics,
Propulsion Laboratory, Wright-Patterson AFB, Ohio
Rpt Nr ASD-TDR-62-650. ELECTROFLUIDMECHANICS:
INVESTIGATION OF THE EFFECTS OF ELECTROSTATIC
FIELDS ON HEAT TRANSFER AND BOUNDARY LAYERS.
Final report, Sep 62, 128p. incl illus., tables, 31 refs.

Unclassified Report

A series of experiments were conducted on the influence
of an electric field on free convection heat transfer. A
heated plate was mounted in a Mach-Zehnder interfero-
meter, and the effects of applied electrical fields were
studied. Large changes in effective heat transfer were
found. Analytical studies were made of this phenomenon.
A suitable mathematical model was formulated on the
basis of the Von Karman integral equations and the

(over)

1. Electrostatic fields
2. Fluid mechanics
3. Heat transfer
4. Hydrodynamics
5. Boundary layer

I. AFSC Project 3141
II. H. R. Velkoff
III. Aval fr OTS
IV. In ASTIA collection

electrostatic field equations. Correlation between the
interferometer test data and the mathematical model
was achieved.

Exploratory tests of fluid orientation and motion under
the influence of dielectric forces were also conducted,
and the potential usefulness of the phenomenon is
graphically portrayed in pictures showing the motion
of water droplets in a "Zero-G" model when a field is
applied.